A New Deep X-Ray Lithography Beamline at DELTA – Setup and Performance –

Dipl.-Phys. Daniela Lietz

Dissertation
zur Erlangung des Doktorgrades der Naturwissenschaften
der Fakultät Physik der Technischen Universität Dortmund

eingereicht am
11. November 2010

Abstract

The efforts in today's technology to produce highly functional devices on ever decreasing dimensional scales demand new production techniques in the field of micro technology. The required micro components cannot be produced with mechanical tools. Instead, micro mechanical components with a height of up to several millimeter and a sub-micron lateral resolution are manufactured by lithography using x-rays. The required x-ray radiation needs to have a high penetration depth, a high intensity and a high parallelism. These demands are met by synchrotron radiation sources.

Within the course of this thesis a dedicated deep x-ray lithography beamline is planned and constructed at the synchrotron radiation facility DELTA at the Technische Universität Dortmund. After beamline commissioning including beam characterization measurements, test wafers are exposed at the new beamline. The generated structures are investigated after chemical development concerning edge steepness, structure fidelity, and sidewall roughness.

Contents

1. Introduction **1**

2. Lithography **5**

2.1. Basic principles of lithography 5

2.1.1. Serial writing mode 6

2.1.2. Parallel writing mode 7

2.1.3. Positive and negative resist 11

2.2. The LIGA process 16

2.2.1. X-ray lithography 17

2.2.2. Electroplating 17

2.2.3. Molding 17

2.3. Deep x-ray lithography 18

2.3.1. Requirements for high structures 18

2.3.2. 3D structures 19

2.3.3. Potential malfunction sources 19

3. Investigation Methods **21**

3.1. Synchrotron radiation 21

3.2. Theory of x-ray scattering 25

3.3. Scanning electron microscopy 27

3.4. Confocal microscopy 31

4. Setup of Beamline BL 1 **33**

4.1. The storage ring DELTA 33

4.2. Beamline hardware setup 34

4.2.1. The valves 39

4.2.2. The photon absorber 39

4.2.3. The collimator . . . 40
4.2.4. The beamshutter . . . 41
4.2.5. The beryllium window . . . 43
4.2.6. The end station . . . 44
4.2.7. The ion getter pumps and turbo pumps . . . 46
4.2.8. The pressure measuring system . . . 47
4.2.9. The fast closing system . . . 48
4.2.10. The electrical supply . . . 48
4.2.11. The compressed air supply . . . 48
4.2.12. The cooling water supply . . . 49
4.2.13. The fulfilment of the radiation protection requirements . . . 49
4.3. Control System . . . 53
4.3.1. The interlock control . . . 53
4.3.2. The valve control . . . 59
4.3.3. The catch system . . . 61
4.3.4. The communication between BL 1 and DELTA control system . . . 62

5. Beamline Commissioning **65**
5.1. Fulfillment of safety requirements . . . 65
5.2. Beam characterization . . . 66
5.2.1. Beam position investigation . . . 66
5.2.2. Beam profile investigation . . . 69
5.2.3. Photon flux calculation . . . 75

6. Sample Preparation **77**
6.1. Wafer cleaning . . . 77
6.1.1. Shiraki cleaning . . . 77
6.1.2. RCA cleaning . . . 78
6.2. Spin coating . . . 79

7. First Exposures and Photoresist Investigations **81**
7.1. Sample holding and x-ray masks . . . 81
7.2. Measurements at BL 2 . . . 85
7.2.1. Exposure performance . . . 85
7.2.2. Investigation of exposed wafers . . . 86

7.3. Measurements at BL 1 89
7.3.1. Exposure procedure 89
7.3.2. Results of the exposures at BL 1 90
7.4. Sidewall roughness 103
7.4.1. Investigation of the mask absorber profile 103
7.4.2. Effect of the membrane material 103
7.5. Conclusion 109
7.6. X-ray reflectivity investigations of the resist 110
7.6.1. Sample environment and preparation 110
7.6.2. Measurement and analysis 111

8. Summary and Outlook **115**

A. Attachment **119**
A.1. X-ray scattering from matter 119
A.1.1. Scattering from surfaces and interfaces 119
A.1.2. Basic principles 120
A.2. Remark 126

Bibliography **127**

Danksagung **I**

1. Introduction

The success of modern technical devices, such as mobile phones, personal computers or storage media, strongly relies on high functionality combined with small size of the devices. To meet these demands it is necessary to increase the packing and functional density of the required micro components. In order to produce such components the size of production tools has to be smaller than the desired object dimensions. A suitable technique for the production of micro components which are used in several fields including mechanical, fluidic, optical, chemical and biochemical applications, is lithography.

The basic idea of lithography is to transfer the lateral shape of the components via shadow projection into a photosensitive resist which is coated on a silicon wafer. Here, the overall scale of the produced structure depends on the wavelength of the radiation used for the projection. In today's technology the production of components on the micro- and nanometer scale is of interest. A special challenge is the generation of structures with heights of several millimeters that offer a sub-micrometer lateral resolution, a high edge steepness, smooth sidewalls and a high structure fidelity. These demands are fulfilled using x-rays for the lithography process.

In industry, reducing the production time is also a goal as this is a major cost factor. In order to meet these demands the LIGA technique was developed. LIGA is the German acronym for (x-ray) lithography, electroplating and molding ((Röntgen-)Lithographie, Galvanik, Abformung), describing the main process steps from the lateral component layout to the final product. To generate high, vertical sidewalls the radiation needs to have a high penetration depth into the photoresist and has to be highly parallel. These requirements are fulfilled by synchrotron radiation which provides an intense source of hard x-rays. In addition, it allows a high throughput with respect to the wafer exposure. Due to the thick resist layer that is exposed by x-rays, this kind of lithography is referred to as deep x-ray lithography (DXRL). Therefore, the first step of LIGA requires access to a synchrotron radiation source.

The Technische Universität Dortmund, located in the direct neighborhood of the technology center in Dortmund, operates a synchrotron radiation facility called DELTA (**D**ortmunder **EL**ek**T**ronen Speicherring **A**nlage). As one focus of the Dortmund technology center is micro- and nanotechnology, the operation of a dedicated deep x-ray lithography beamline at DELTA is planned. This beamline offers the DXRL technique to the micro competence centers nearby.

In the early operation phase of DELTA a first x-ray lithography beamline was constructed using the technique of electron beam wobbling [1]. As this operating mode conflicted with experiments that depend on a stable beam position, this beamline was not further pursued. As micro technology expanded, the project of a lithography beamline was restarted. This time the electron beam will be kept stable and the sample should be moved across the photon beam. Proof of principle test exposures carried out at the ISASLine BL 2 were a success and showed the feasibility of DXRL at DELTA. The results obtained were essential for the decision to set up the dedicated lithography beamline BL 1 at DELTA. This beamline was planned, constructed, and commissioned in the course of this thesis. After completion of the setup, first exposures were performed.

The structure quality of micro components is of great interest for industry. Structures produced at BL 1 were thus investigated in this regard by scanning electron microscopy, confocal microscopy, and optical microscopy. In addition, the surface properties of the photoresist SU-8 used for the exposures were determined by x-ray reflectivity measurements.

The thesis is structured as follows. The basic principles of lithography are described in chapter 2, including the description of the most common photoresists. Furthermore, the LIGA process and the advantages of deep x-ray lithography are explained.

Chapter 3 deals with the different experimental techniques performed in this study. Thus, the characteristics of synchrotron radiation are explained and the techniques of x-ray reflectivity, scanning electron microscopy, and confocal microscopy are outlined.

The beamline setup regarding the beamline hardware as well as the software configuration is presented in chapter 4.

The beamline commissioning including the safety protection requirements and the photon beam characterization are outlined in chapter 5.

To perform x-ray reflectivity measurements on SU-8, silicon wafers were spin coated with this negative photoresist. Prior to the coating process the wafers were cleaned. The respective procedures of wafer cleaning and coating are described in chapter 6.

Structures resulting from test exposures at ISASline BL 2 and at the completed BL 1 were investigated with respect to structure quality and sidewall roughness. The latter aspect was studied in dependence of two different x-ray mask materials. The negative resist SU-8 was investigated regarding its surface characteristics by x-ray reflectivity measurements. The results are presented in chapter 7.

A summary of the beamline setup and the performed studies is given in chapter 8, including a perspective for future projects regarding lithography exposures at BL 1.

2. Lithography

Lithography is a powerful technique for the production of micro components. It can be applied in different ways depending on the desired structure size and the field of application. The basic principles of lithography are explained in the first section of this chapter. It is followed by the description of a process line (LIGA) for the entire production process of micro components starting with the structure design to the final product (section 2.2). Ultra-high components with a thickness of up to several millimeters can be manufactured by use of deep x-ray lithography. The characteristics of this technique are described in section 2.3.

2.1. Basic principles of lithography

From the historical point of view lithography is the oldest technique of planographic printing, developed in 1798 by Alois Senefelder. The literal interpretation of lithography is $\lambda\iota\theta o\varsigma$ (Greek: lithos) which means “stone” and $\gamma\rho\alpha\varphi\omega$ (grapho) which means “to write” [2]. During the 19th century it was the only method to print colored papers in a high run.

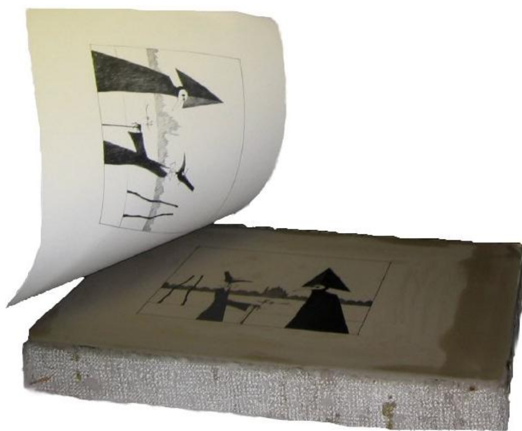

Fig. 2.1.: A smooth limestone with the master drawing on its surface and the finished printing are shown [3].

The procedure of lithographic printing is as follows: The master is drawn with oil-based paint (e.g. wax crayon) on a smooth limestone. In a subsequent step the stone is covered with an aqueous solution of gum arabic, which is weakly acidified with nitric acid HNO_3. The solution of gum arabic sticks to the oil-free surface parts, i.e. the non-painted regions, and reacts with the limestone. As a result a hydrophilic layer of calcium nitrate $Ca\left(NO_3\right)_2$ and gum arabic is formed. For the printing process the stone is covered with water which adheres solely to the

gum arabic layer. Greasy ink is rolled over the stone and sticks to the painted areas while it is rejected from the water at the non-painted regions. Afterwards a piece of paper is pressed on the stone and the colored drawing is transferred to the paper [4]. In figure 2.1 a limestone with a painting on top and the finished print with the transferred drawing is shown.

In recent years lithography techniques have been used to produce technical devices on the micrometer scale for applications in communication technology, storage media, medical science, and medical engineering.

A substrate, mostly a silicon wafer, is covered with a photosensitive resist. The component structure that shall be produced is transferred into the resist by either direct writing with a particle or focussed light beam or by large-area shadow projection using a mask that contains the desired structure. The main distinctive criterion of the lithography techniques is the operation in a serial or a parallel writing mode. By use of parallel production modes a special mask is required. This mask, representing the master drawing, contains the lateral component structure. The mask membrane is made of a transparent material and the lateral component shape is applied on the membrane using an opaque substance (so-called absorber structure). The choice of appropriate materials depends on the type of lithography and is explained in more detail in section 2.1.2.2.

A short overview of the different modi and types of lithography is given in the following.

2.1.1. Serial writing mode

In the serial writing mode the lateral component structure which shall be produced is written pixel by pixel into the resist by a focused light beam (laser) or by a particle beam (e.g. electron beam or ion beam). The desired structure is entered into a computer program that controls the beam movement. The beam is moved across the resist such that it traces the desired structure shape, hence a mask is not necessary. Due to the computer-controlled process this technique is very flexible.

The possible resolution for this mode is in the nanometer region (1 nm = 10^{-9} m) [5]. Using ion beams the maximum resist height that can be structured is 500 nm [2], while by use of electrons the resist thickness can be up to a few micrometer [4]. However, the major disadvantage of this technique is its high expenditure of time. Therefore, the main applications of the serial mode are production of masks and prototypes or low quantity components. In the latter case it is a too big effort to produce a mask for a large-area exposure.

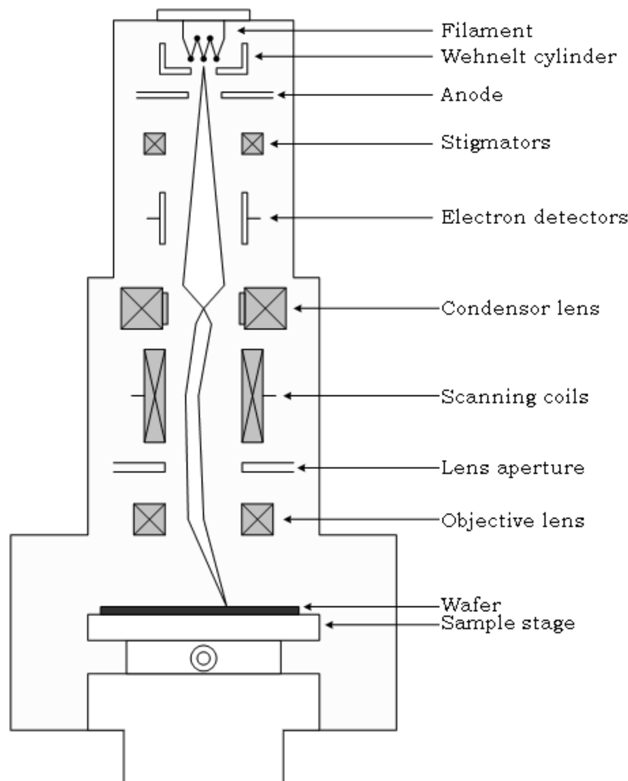

Fig. 2.2.: Typical setup of an electron beam lithography station. The electron source, the lenses, aperture stops, deflection coils, and the correction system are shown [6].

For the production of masks which are used for the exposures in parallel mode, electron beam lithography is the initial step. For the design of prototypes the flexibility of the serial procedure is required.

Using electrons or ions to write a structure in the serial mode, the particle beam is focused to a fine jet of about 10 nm beam width [7]. This stream is deflected by electron-optical and ion-optical systems, in order to scan the resist surface. The degree of deflection is limited to about 1 mm [4]. For the exposure of a large area the positioning stage must be movable within the desired range [7]. In figure 2.2 a typical setup of an electron beam lithography station is shown. The electrons emitted by the electron source are accelerated by the anode to a kinetic energy of 10 - 100 keV [4]. They pass different lenses yielding focusing by electrical or magnetic fields and aperture stops which modify the beam profile. On their way to the resist they are deflected by scanning coils and their position is measured and controlled by electron detectors [7]. The required structure is thus written into the resist with high precision but in a time-consuming procedure.

2.1.2. Parallel writing mode

In order to produce components in a high quantity it is too time-consuming and therefore too expensive to manufacture the components in a serial process. To overcome these limitations the structures can be generated by use of a parallel writing process. Within this mode a mask is exposed with adequate parts of the electromagnetic spectrum (visible light to x-rays). The radiation penetrates the mask at the transparent membrane and produces a shadow image of the absorber structure in the resist. This mode can be operated in full-wafer exposure or

step by step in case of very large wafers. Full-wafer exposure means that the whole wafer is exposed in one step using a broad beam and scanning the wafer and the mask through this beam. Using large wafers the resist is exposed through the mask in a small area; afterwards, the mask is moved to the next subarea for exposure. This process is called step-and-repeat mode.

Depending on the desired structure dimensions different regions of the electromagnetic spectrum are used. Structures with dimensions larger than 0.5 μm can be generated with visible (400 - 750 nm) or near ultraviolet light (465-250 nm) [2]. If sub-micrometer structures shall be transferred in optical or UV lithography, lenses are required (projection lithography, see section 2.1.2.1). However, using lenses means abandoning full-wafer exposure and hence a higher expenditure of time. In order to achieve high demands concerning structure fidelity the mask is exposed partially in the step-and-repeat mode. This implies high requirements for the movement and positioning of the mask. For dimensions in the nm region a radiation source with smaller wavelengths is necessary. Here e.g. an excimer laser (UV spectrum) is operated in projection lithography using concave mirrors and reflecting masks [2, 8] as well as projection lenses made of quartz as it is the only suitable material in the deep ultraviolet region [8].

For the structure diminution to the nm scale (and below) and especially in order to perform full-wafer exposures with submicron lateral resolution, x-ray lithography is applied. Operated at a synchrotron radiation source, the wavelength for lithography is within the region 10 - 0.1 nm (124 eV - 12 keV) [2, 7]. Hence, a structure size reduction by projection systems is not necessary. While diffraction in optical and (extreme) ultraviolet ((E)UV, 10 - 400 nm) lithography can limit the feasible resolution, this effect is negligible for x-ray lithography using the broad synchrotron radiation spectrum (white beam).

Three main principles for exposure exist within the parallel mode, referred to as projection lithography, contact lithography, and proximity lithography. The last two methods are summarized in the process of shadow projection.

2.1.2.1. Projection lithography

Projection lithography is used for example in optical or (extreme) ultraviolet lithography, mapping the structures to a smaller scale on the resist. By scaling down the structures, the possible imprecisions and imperfections of the mask, which are responsible for structure defects, are also scaled down and are less serious compared to an exposure on the scale 1:1 [7]. This is a big advantage of this technique. The possible lateral resolution is less than 0.5 μm [7].

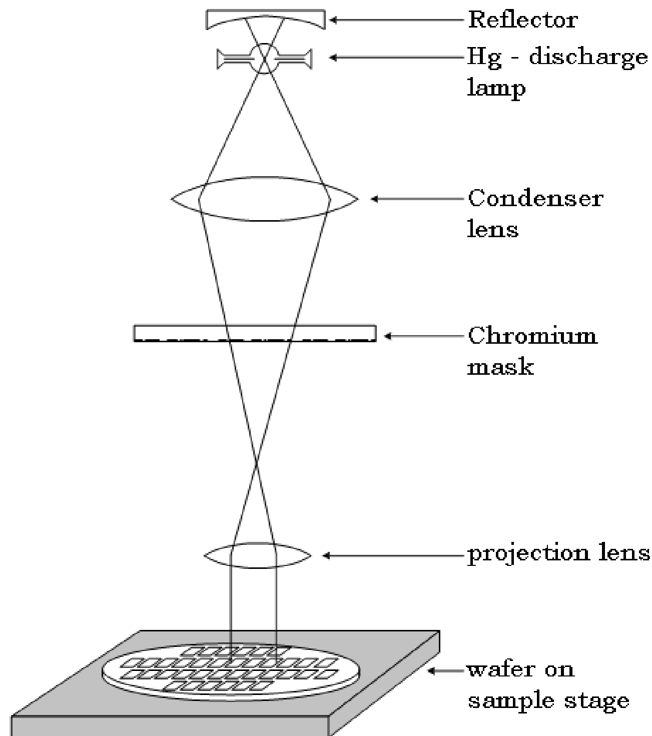

Fig. 2.3.: Schematic drawing of an equipment for projection lithography [9].

Projection lithography uses an adequate imaging system (figure 2.3) and a special mask, called reticle, which contains the scaling factor [4]. The mask is fixed between the lenses such that the shadow image is transferred to the resist on the favored scale (10:1 up to 4:1). Using projection lithography only a small area can be exposed in one step. In order to structure the entire wafer the step-and-repeat mode is applied in projection lithography.

As projection systems are very difficult to realize for x-rays, projection lithography is not relevant for exposures with synchrotron radiation in deep x-ray lithography. Instead, the shadow projection mode is used.

2.1.2.2. Shadow projection lithography

If a projection on the scale 1:1 is requested, the lenses are omitted and shadow projection lithography is used. A wafer, coated with a photoresist, is exposed through a mask in a large area (figure 2.4). The radiation penetrating the mask is absorbed by the mask absorber structure which forms the lateral component shape. At the transparent membrane parts the radiation passes the mask, transferring the absorber profile to the resist surface by shadow imaging. The radiation penetrates the resist layer perpendicular to the surface and leads to a

chemical change over the full resist height in the exposed region. The gap seen in figure 2.4 for so-called proximity exposure is about 10 - 50 µm high [2]. In case of contact lithography, which is another mode of shadow projection lithography, the mask is applied right on the resist, i.e. the gap is zero.

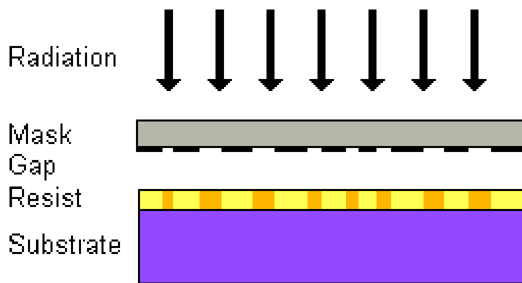

Fig. 2.4.: Scheme of wafer exposure using shadow projection lithography. The wafer is exposed through a mask, yielding a shadow image of the lateral absorber structure in the resist.

For optical exposures the mask assembling procedure is as follows: The transparent base plate is made of a flat quartz glass plate with a thickness of a few mm. A thin chromium layer of about 100 nm is applied on top, forming the lateral absorber structure. For x-ray lithography mostly gold is used as an absorber, but also wolfram or tantalum can be chosen. Gold can easily be deposited by electroplating, whereas wolfram and tantalum have to be structured by reactive etching processes [2]. Therefore, gold is the favored absorber material. It is important to utilize a material with a high atomic number, corresponding to a high absorption. In contrast, the transparent membrane is made of a material with a low atomic number ensuring an unhampered way of the x-rays through the membrane. Materials for mask membranes are silicon, silicon nitride, boron nitride, silicon carbide, graphite, beryllium and titanium. The latter is used for the production of precision masks (see chapter 7.4.2).

Contact lithography

Within contact lithography the mask is applied directly on the resist surface [2]. The advantage of this mode is that a high resolution can be obtained. The minimum line width w_{prox} for contact and proximity exposures depends on the resist thickness, the gap g between mask and resist, and the wavelength λ for the exposure [4, 7]

$$w_{\text{prox}} = \frac{1}{2}\sqrt{\lambda g}\,. \tag{2.1}$$

As w_{prox} decreases with decreasing gap and wavelength, the resolution increases. The reachable lateral resolution of optical lithography performed in contact mode is in the sub-µm region [4]. Hence, the contact mode delivers a better resolution than the proximity exposure mode.

The disadvantage is the high potential for damages: any particle enclosed between resist and mask can lead to a distortion and to a failure in the structure transfer. In addition, it is possible that parts of the resist stick to the mask and pollute it. In addition, a less flat resist surface leads to a bad contact between resist and mask yielding different structure resolutions. Thus, the risks of distortion are very high and the chance to use the mask again for several times decreases.

Proximity lithography

For wafer exposure performed via proximity lithography, the mask is fixed in front of the wafer with a small gap of about 10 - 50 μm. Due to the gap, the probability of damaging the mask or the structure is minimized and the chance to use the mask for several further exposures is increased.

Using visible light, the possible lateral resolution for an exposure with a proximity gap is 2 - 4 μm [4]. Considering equation 2.1 the gap can be in the order of some millimeters when using synchrotron radiation with wavelengths in the region of 0.2 - 2 nm, without the loss of submicron resolution [10, 11]. For optical lithography a lower resolution due to diffraction effects has to be accepted.

As a result of the almost wear-free process and the recurring high precision, it is possible to produce several million components with a high structure fidelity in a cost-efficient process [2]. A special process line utilizing the reproducibility is the LIGA process. It includes the steps of (x-ray) lithography, electroplating and molding and has its name with respect to the German terms **Li**thographie, **G**alvanik and **A**bformung. The process steps of LIGA are explained in section 2.2.

2.1.3. Positive and negative resist

The material applied on wafers for structuring is a photosensitive resist that changes its chemical structure due to exposure. The term resist derives from the word resistent. For lithography this means that the resist adheres strongly to the wafer after exposure and chemical development and overcomes the subsequent process steps without any damage. The main principle of photoresists is the change in molecular weight due to exposure [5]. The chemical developer is sensitive to the molecular weight: the lower the weight, the better the resist solubility in the developer.

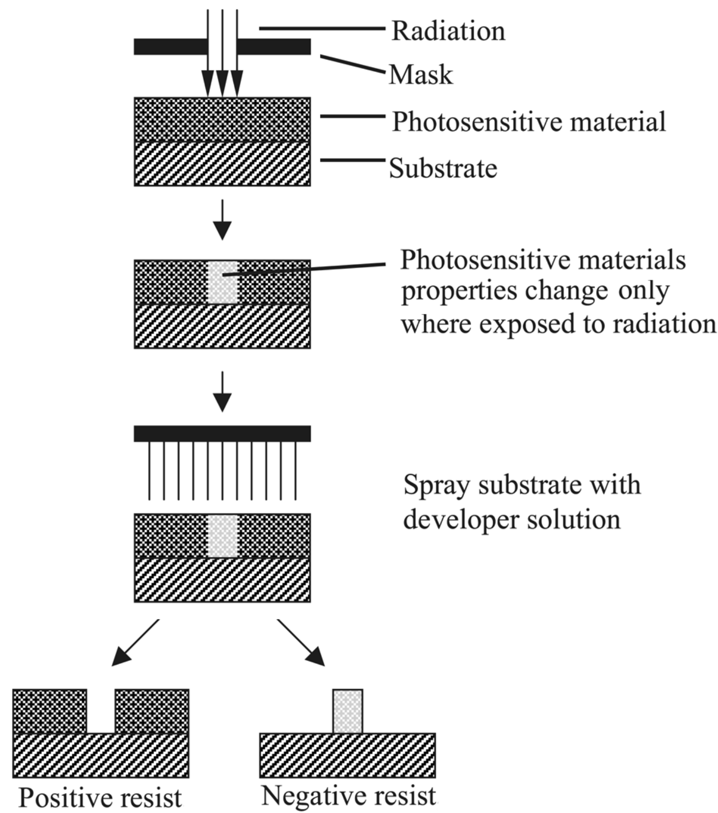

Fig. 2.5.: Resist behavior due to exposure. Exposed parts of positive resist are removed, while they remain on the wafer for negative resist [12].

The types of resists are generally divided into two main groups: positive and negative resists (figure 2.5). The molecular weight of the positive resist is decreased as a result of exposure and therefore the exposed regions are removed during the chemical development. The negative resist behaves contrary to the positive resist. Here, the molecular weight increases at the exposed areas and these parts remain at the wafer after chemical development.

The specific characteristics of positive and negative resists are described using the example of the two most common resists: polymethylmethacrylate (PMMA) and SU-8.

2.1.3.1. Positive resist

The best-known representative for positive resists is polymethylmethacrylate (PMMA) shown in figure 2.6. It consists of long hydrocarbon polymer chains. The molecular weight of the PMMA monomer, i.e. methylmethacrylate, is about 100 $\frac{\mathrm{g}}{\mathrm{mol}}$. The polymer chains are composed of several thousand units yielding a molecular weight of several 100,000 $\frac{\mathrm{g}}{\mathrm{mol}}$.

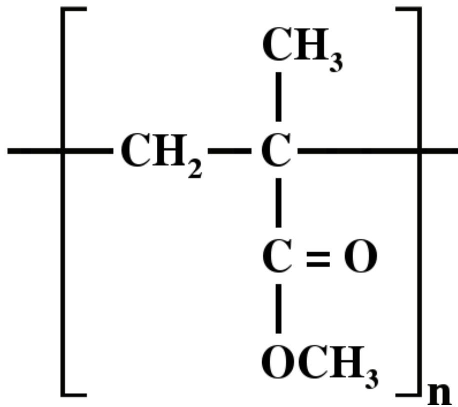

Fig. 2.6.: Chemical structure of methyl-methacrylate. Sequence repetition leads to the polymer PMMA.

Exposing the resist with high-energy radiation ($\lambda \leq 1$ nm, $E \geq 1$ keV) or with electrons ($E \geq 20$ keV), the chains become excited [2]. In this process, the initial molecular weight of about 650,000 $\frac{\mathrm{g}}{\mathrm{mol}}$ is diminished to about 2,500-3,000 $\frac{\mathrm{g}}{\mathrm{mol}}$ at high exposure doses [2]. Using synchrotron radiation, the x-rays transfer their energy to single atoms by photo effect and therefore generate highly energetic photo- and Auger-electrons. These electrons pass through the resist transferring their energy to other molecules until they reach thermal energy. The energy transfer leads to further excitations. As a result, the resist contains ionized and excited molecules in the exposed regions which fracture the main polymer chains and lead to a reduced molecular weight.

A quantitative measure for the number of main chain breakages per 100 eV are the so-called G values [2, 13]

$$G(s) = \left(\frac{1}{M_{n,D}} - \frac{1}{M_{n,0}}\right)\frac{100 \cdot N_A}{D}. \tag{2.2}$$

$M_{n,0}$ is the molecular weight in $\left[\frac{\mathrm{g}}{\mathrm{mol}}\right]$ prior to exposure, $M_{\mathrm{n,D}}$ is the weight after exposure when only scission is taken into account. The deposited dose in the resist is given by D $\left[\frac{\mathrm{eV}}{\mathrm{g}}\right]$ and N_{A} is the Avogadro constant. At higher doses also cross linking processes appear. The measure for this cross linking reactions is given by $G(x)$, defined in analogy to $G(s)$. If $G(s) > G(x)$, the average molecular weight decreases. For $G(s) = G(x)$ no change in the mean molecular weight occurs. This implies that a dose above a certain upper limit dose does not lead to a better dissolution of PMMA.

As the resist solubility increases with decreasing molecular weight, the exposed areas are removed during the following chemical development while the unexposed areas constitute a relief of the mask absorber structure.

As the exposed dose decreases exponentially over the resist height, a dose that is high enough to expose the resist at the bottom has to be chosen in order to guarantee dissolution. However, the dose must not be too high at the resist surface because PMMA tends to formation of bubbles when it is overexposed, leading to structure distortions [5]. Using x-rays for exposure, the best results can be achieved when the deposited dose is less than 20 $\frac{\mathrm{kJ}}{\mathrm{cm}^3}$ at the

top and about 4 $\frac{\text{kJ}}{\text{cm}^3}$ at the bottom of the resist layer [2, 7, 14]. The maximum permitted dose at the unexposed regions is less than 0.1 $\frac{\text{kJ}}{\text{cm}^3}$.

PMMA has some advantages as it can be exposed a second time in order to establish multiple structure levels and it is well suited for injection molding [2]. However, the constraint is that the optimum molecular weight is a compromise between an optimized resist and good results in injection molding.

2.1.3.2. Negative resist

SU-8 is the best-known negative resist. It consists of epoxy resin as the main component, in combination with a photoacid generator (PAG) and solvents for both constituents [2, 15, 16]. Depending on the desired resist thickness, the solvents are combined in different fractions. Within one spin-coating process (section 6.2) it is possible to deposit a layer of about 500 μm on the wafer surface, while casting the resist on the wafer yields several millimeter thick resist layers. The wafer coating is followed by a so-called soft-bake (also called prebake) at approximately 200°C to evaporate the solvents and to reach a resist hardening.

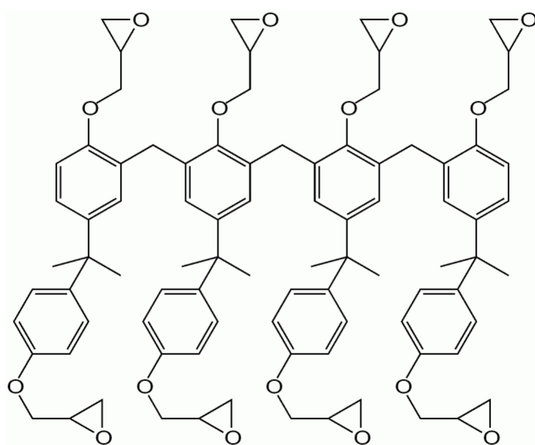

Fig. 2.7.: Chemical structure of the epoxy resin molecule $C_{87}H_{98}O_{16}$ [17].

The epoxy resin consists of eight epoxy groups (triangular groups at the particular chain endings, figure 2.7) and has the molecular formula $C_{87}H_{98}O_{16}$ [18] and a density of 1.2 $\frac{\text{g}}{\text{cm}^3}$ [19].

The PAG (Triarylsulfoniumhexafluoroantimonate salt) is a salt which is split by a photo induced reaction due to exposure. As a result several high reactive organic radicals and cations are generated, which react with the solvents and the epoxy resin molecules yielding the release of catalytic protons [16]. Thus, the salt becomes an acid during the exposure. The mobility of the acid and the epoxy molecules is very restricted at room temperature. For this reason the acid remains at the exposed areas.

Due to the post exposure bake (PEB), the temperature increases above the glass transition temperature $T_g = 55$°C of the resist. Therefore the protons of the acid react with the epoxy groups of the resin molecules as shown in figure 2.8. The excited molecules of the epoxy resin

thus can crosslink with each other. As a result a highly complex resist polymer is obtained, which is very stable to even aggressive chemical processes.

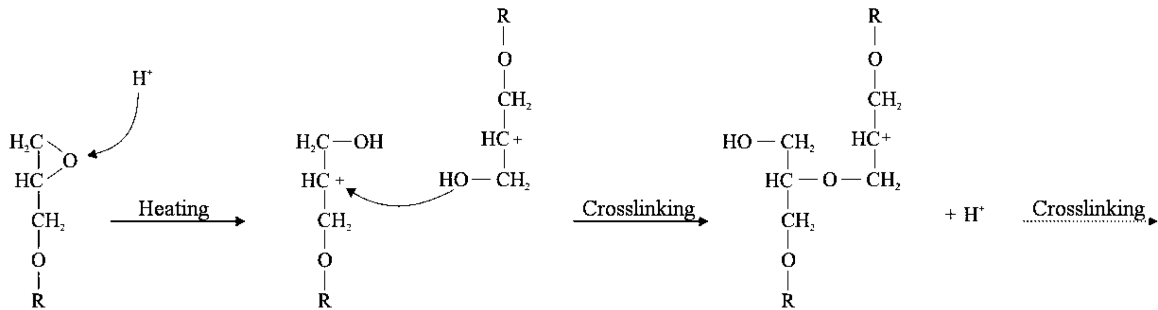

Fig. 2.8.: Cross linking process of epoxy resin molecules. Protons affect the epoxy groups yielding a breakage in these groups. During the subsequent heating the activated monomers crosslink with each other [16].

As T_g increases with the degree of cross linking, the acid mobility decreases yielding an interlacing of the resist molecules solely in the exposed areas. As a result very steep edges between cross-linked and non cross-linked regions are generated. In order to reach a full cross linking, the PEB is performed in two steps. In the first step the temperature is slightly higher than the glass transition temperature. Therefore the cross linking can start at the exposed regions. As the mobility decreases with proceeding cross linking, the temperature in the second step has to be considerably higher than T_g in order to keep the cross linking going on and to guarantee a complete cross linking in the exposed areas [2].

For SU-8 the maximum dose for the unexposed material is 2 $\frac{\mathrm{J}}{\mathrm{cm}^3}$ [2, 16, 20]. Jian et al. determined 0.05 $\frac{\mathrm{J}}{\mathrm{cm}^3}$ as the maximum allowed dose beneath the absorber structure [15]. Otherwise the resist cannot be removed and yields distorted structures. For a complete interlacing the dose has to be at least in the region of 10 - 30 $\frac{\mathrm{J}}{\mathrm{cm}^3}$ [11, 15, 20].

Compared to PMMA the negative resist SU-8 has some advantages:

- SU-8 has a 10 times higher sensitivity than PMMA, resulting in a minimum required dose that is two orders of magnitude smaller.
- Its sidewall roughness is better than the one of PMMA.
- It features a higher chemical resistance and its fabrication is faster and cheaper [20], thus it is more and more implemented in x-ray lithography.
- As SU-8 can serve as a mold for electroplating, it is well suited for the LIGA process.

2.2. The LIGA process

The term LIGA is a German acronym standing for x-ray lithography, electroplating, and molding ((Röntgen-)**Li**thographie - **G**alvanik - **A**bformung). This technique was developed at the end of the 1970's by Erwin Becker and Wolfgang Ehrfeld at the nuclear research center Karlsruhe. Originally it was developed to produce components for the separation of isotopes of uranium hexafluoride UF_6 [2, 5, 21].

The specialized implementation of LIGA is the fabrication of high micro components using synchrotron radiation for resist structuring. Concerning aspect ratio (structure height : structure width), spatial resolution, precision, and sidewall roughness, LIGA is the superior technology compared to other micro-fabrication technologies [5] like machining micro processing, micro spark erosion, and laser machining [2].

The different steps of LIGA are shown in figure 2.9 and described in sections 2.2.1 - 2.2.3.

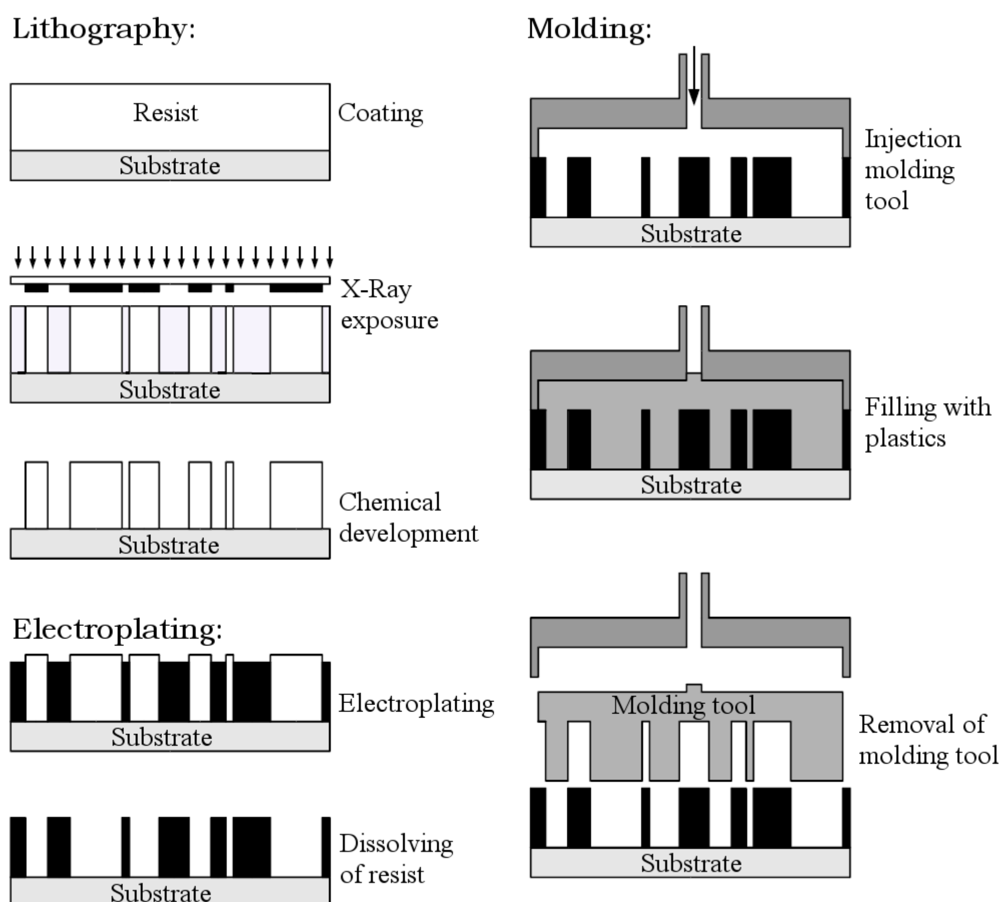

Fig. 2.9.: The different process steps of LIGA. Their order is as follows: x-ray lithography including chemical development, electroplating followed by molding.

2.2.1. X-ray lithography

X-ray lithography is performed as proximity exposure (section 2.1.2.2) utilizing a wafer (for example silicon) covered with a thin gold film or another electrically conducting material, which serves as a starting layer for electroplating. The wafer is coated with an x-ray sensitive photoresist. The two main types of photoresists have been described in section 2.1.3. The resist thickness depends on the desired application and can reach several millimeters [7].

X-rays penetrate the mask, generating a shadow image of the lateral absorber structure on the resist and yield a chemical change in the exposed areas. Depending on whether a positive or negative resist is applied the exposed or unexposed areas are removed in the subsequent chemical development [5]. As a result, the developed, free-standing, tall, two dimensional (positive or negative) component profile is obtained on the wafer.

So far, these profiles are composed of resist. In case of micro-optical applications it is possible to some extent to use these micro structures as a final product. However, mostly metallic components or sturdy, inherently stable molding tools are of interest. Hence, the subsequent process step is electroplating.

2.2.2. Electroplating

Within this step the cavities in the resist layer emerging from the exposure and the chemical development are filled with metal (copper, nickel, nickel alloy, gold) [2, 7]. The deposition starts at the conducting baseplate and fills the spaces between the non-conductive photoresist. After the electroplating the photoresist is removed and thus a complementary structure made of metal is produced [2, 7].

As lithography and electroplating are expensive procedures, the process of duplication is of interest. This demand is met by molding which is the last process step of LIGA [7].

2.2.3. Molding

The metal structure received from the electroplating is used to produce copies in plastic material by injection molding and hot embossing in nearly arbitrary quantity. These plastic structures can be used in different ways. They can be covered with a conducting layer and serve as a mold for electroplating in order to produce metal structures or they can be utilized for the fabrication of e.g. ceramic structures.

2.3. Deep x-ray lithography

Deep x-ray lithography (DXRL) using synchrotron radiation is a powerful technique to fabricate structures up to a height of 2 - 3 mm with a lateral resolution of about 0.2 μm [7, 10, 22]. It has a wide field of applications especially in micro optics and micro mechanics. Small gear wheels for high-precision positioning systems can be produced as well as fresnel zone plates, micro-optical benches, acceleration switches, micro-fluidic chips, micro-pumps and much more. These components are applied in telecommunication applications, as sensors in automotive industry, for analytical sciences, in medical devices, as recording heads for hard disks, etc. [2, 5, 7, 10, 15, 23–25].

DXRL is performed in proximity exposure as there exist no imaging systems for x-rays to accomplish projection lithography and as the possibility for damages in contact lithography is too high [7]. Using DXRL as part of LIGA a fast and cost-efficient production of high micro components is feasible. Compared to optical lithography, which has a best feasible aspect ratio of about 25:1 [26], DXRL is able to achieve aspect ratios in the region of 80:1 to 100:1 [15, 25–27].

2.3.1. Requirements for high structures

In order to produce several hundred micrometer up to a few millimeter high structures, the resist thickness has to be adapted to the favored structure height and therefore becomes very thick. To expose the full resist height within an acceptable time, very intensive radiation with a high penetration depth is required [5]. In order to gain defined structure walls with a high edge steepness and a well orthogonality between the resist surface and wall as well as between the structure wall and the wafer, the radiation has to be highly parallel. These challenges are met by synchrotron radiation.

For best results the wavelength has to be in the range 0.2 - 2 nm [4]. At smaller wavelengths the resist becomes transparent and the energy transfer into the resist is too low. In addition, the absorber structure thickness has to be increased. However, the wavelength should not exceed 2 nm because in this case the absorption of the mask membrane becomes significant [2]. Typical masks can be made up like listed below:

- 500 μm beryllium with 10 - 20 μm gold for a SU-8 thickness of about 500 μm [26],
- 150 μm graphite with 90 μm gold in order to expose 4 mm high structures in SU-8 [11],

- 2.3 µm titanium with 25 µm gold in order to expose SU-8 with a thickness of 360 µm [20].

2.3.2. 3D structures

By use of deep x-ray lithography, it is possible to produce three-dimensional structures. One possibility is the multi-layer exposure. Several SU-8 layers are applied and exposed one after another. After the last layer has been exposed the whole system is developed. The result is a micro structure build up by multiple layers. Using a combination of layers made of SU-8 and PMMA, the production of complex 3D structures is feasible [15].

Combining perpendicular and tilted exposure or rotating the mask-substrate-system across the beam, it is possible to achieve structures with inclined sidewalls [5, 25].

As the chemical development depends on the exposure dose, an exposure with distributed doses leads to inclined and curved structures. This non-uniform dose distribution is achieved by exposures with and without masks as well as by use of masks with different absorber thicknesses [5].

2.3.3. Potential malfunction sources

As the exposure dose has to be deposited over the full resist height, it is necessary to exclude the long wavelength radiation prior to exposure because this spectral region is solely absorbed in the top resist region. Using the full spectrum therefore leads to an overexposure at the resist surface while the bottom region receives an insufficient exposure dose and cannot be developed to a satisfying extent. Materials well suited to oppress the thermal part of the radiation are beryllium or Kapton (polyimide). For DXRL the thickness of such a beryllium window is about 100 - 500 µm [7].

High structures produced by DXRL feature almost perfectly perpendicular sidewalls. Yet, the higher the structure, the higher the irregularities. The most important reasons for these irregularities are the mechanical movement of the wafer and the mask during the scans, a nonsatisfying chemical development due to an insufficient developer selectivity concerning irradiated and unexposed areas, uncertainties in the setup of the mask and the wafer, and not at least physical effects caused by x-ray irradiation. Concerning the latter aspect the structure quality mainly depends on the radiation divergence and the range of the photo electrons generated in the resist.

Secondary effects like fluorescence radiation originating from the mask membrane as well as photo electrons deriving from the substrate are also important as they can lower the exposure quality [2, 7].

The effect of Fresnel diffraction at the absorber structure edges can be neglected when using the polychromatic synchrotron radiation spectrum [5]. In this case the condition for interference at one point is only fulfilled for one particular wavelength while the rest of the spectrum hits the resist undisturbed. For DXRL, the edge blurring is < 0.1 μm [2].

Due to x-ray irradiation photo electrons and Auger-electrons are generated in the resist yielding a chemical change of the resist. Because of their energy they move in the resist, thereby statistically hitting the resist molecules and transferring their energy to the molecules. Therefore they can reach unexposed regions in the resist leading to a lowering of the edge acuity. For wavelengths greater than 0.1 nm the electron path length is less than 0.15 μm [2].

As the exposure of the mask can generate fluorescence radiation in the membrane which is emitted homogeneously over the dihedral angle, the radiation can reach unexposed regions beneath the absorber yielding an edge rounding at the resist surface. If the absorption edge of the mask membrane material is within the spectrum for exposure the effect is more critical. For example titanium has an absorption edge at 2.5 keV which can lead to a structure edge rounding with a radius of approximately 150 μm [2].

As high energetic photons can cross the full resist height they can produce secondary electrons in the substrate especially in the metallic starting layer for the electroplating. These electrons expose the resist from the bottom and can also reach unexposed regions. This leads to a reduced resist adhesion on the substrate resulting in distorted structures which cannot be processed by electroplating.

3. Methods for the Investigation of the Resist and the Structure Quality

The production of high quality micro structures requires the application of synchrotron radiation. Therefore, the characteristics of this radiation type are shortly described in section 3.1. As the structure quality of resist structures exposed at DELTA was investigated by scanning electron microscopy (SEM) and confocal microscopy, these methods are presented in sections 3.3 and 3.4, respectively. The method of x-ray reflectivity measurements as a surface sensitive method is described in section 3.2 because this technique was used for the investigation of the surface characteristics of the photoresist SU-8.

3.1. Characterization and description of synchrotron radiation

At a synchrotron radiation source particles with charge e are accelerated to nearly the velocity of light c and are stored in a closed orbit. In order to gain high particle lifetimes the storage ring has to be operated under ultra high vacuum (UHV) conditions, i.e. the pressure inside the storage ring is less than 10^{-7} mbar. The particles inside the storage ring are deflected by bending magnets (also called dipole magnets) in order to stay in the orbit, thereby emitting photons due to the change in direction.

The radiated power P is mainly given by the change in the electron momentum $\vec{p}$ [28]. For non-relativistic particles ($v \ll c$) the power can be calculated from

$$P = \frac{e^2}{6\pi\epsilon_0 m_0^2 c^3} \left(\frac{d\vec{p}}{dt}\right)^2 \tag{3.1}$$

where ϵ_0 is the vacuum permittivity and m_0 denotes the particle rest mass. In case of relativistic particles ($v \approx c$) with energy E that fly on a circular orbit, i.e. they experience an acceleration perpendicular to their flight direction, equation 3.1 becomes [28]

$$P = \frac{e^2 c}{6\pi\epsilon_0 \left(m_0 c^2\right)^4} \frac{E^4}{R^2} \tag{3.2}$$

with R describing the deflection radius of the particle trajectory.

The energy loss per turn ΔE per charged particle is given by

$$\Delta E = \frac{e^2}{3\epsilon_0 \left(m_0 c^2\right)^4} \frac{E^4}{R} \tag{3.3}$$

that is for electrons [7, 28]

$$\Delta E[\text{keV}] = 88.5 \left(\frac{E^4[\text{GeV}^4]}{R[\text{m}]} \right) . \tag{3.4}$$

Therefore, the entire emitted power for a given electron beam current I is calculated from [2]

$$P[\text{kW}] = 88.5 \, \frac{E^4[\text{GeV}^4] \, I[\text{A}]}{R[\text{m}]} . \tag{3.5}$$

Knowing the electron energy E and the magnetic field strength B of the bending magnet, the deflection radius is given by

$$R = \frac{E}{ecB} = 3.3356 \, \frac{E[\text{GeV}]}{B[\text{T}]} . \tag{3.6}$$

Electrons in the dipole magnet emit radiation in tangential direction to their orbit [7]. The emitted radiation spectrum covers the whole range from infrared (few meV) to hard x-rays (up to 100 keV). As the spectrum is polychromatic, it is called white radiation. A critical wavelength λ_c or critical energy E_c is defined for the integrated power spectrum that divides the spectrum into two parts with equally sized areas beneath the curve [29]

$$\lambda_c = \frac{4\pi R}{3\gamma^3} \tag{3.7}$$

$$E_c = \frac{hc}{\lambda_c} \tag{3.8}$$

where h is the Planck constant and $\gamma = \frac{E}{m_0 c^2}$.

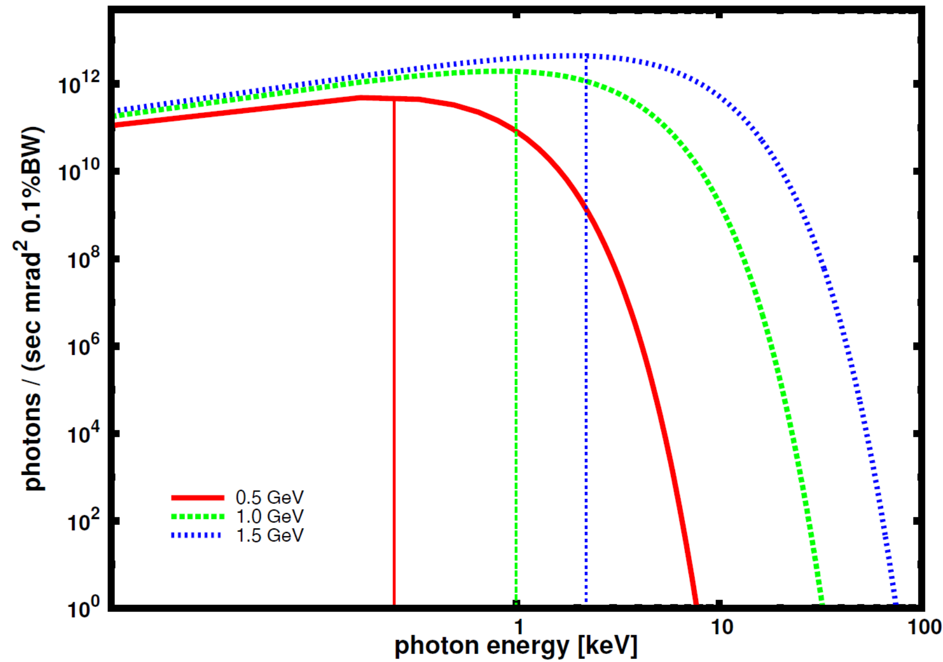

Fig. 3.1.: Power spectra of a bending magnet shown for three different electron energies. The vertical lines indicate the corresponding critical energies.

In figure 3.1 the photon flux of a 1.5 T bending magnet is shown as a function of the photon energy for three different energies. In addition, the corresponding critical energies are depicted. The photon flux defines the number of photons that are emitted per second within an energy bin of 0.1% bandwidth (BW) and within a dihedral angle that is given by the horizontal and vertical divergence. The spectrum is calculated considering an electron beam current of 100 mA. The chosen electron energies and the corresponding critical energies are:

- E_e = 0.5 GeV with E_c = 249 eV ,
- E_e = 1.0 GeV with E_c = 997 eV ,
- E_e = 1.5 GeV with E_c = 2244 eV .

The emitted radiation is extremely directed in forward direction and therefore highly parallel [2]. In vertical direction the radiation is emitted in a total angle of [28]

$$\theta = \frac{2}{\gamma} . \tag{3.9}$$

θ is the so-called vertical divergence, solely depending on the electron energy.

For an energy of 1.5 GeV the vertical divergence is $\theta = 0.68$ mrad (0.04°). This leads to a beam height of about 10 mm at a distance of 14 m from the source point. This is a usual beam

height for DXRL, therefore no aperture slits are necessary to limit the beam height at the end station [7]. The vertical beam profile is given by a gaussian distribution [28].

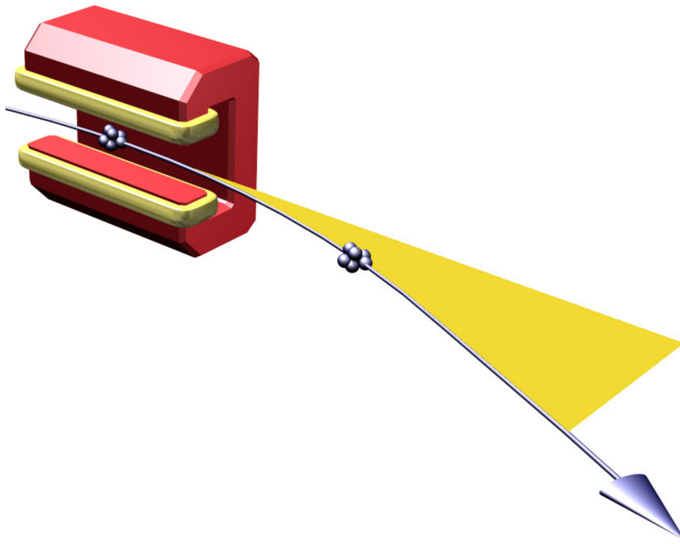

Fig. 3.2.: Horizontal distribution of photons emitted by electrons that are deflected by a bending magnet [30].

As the bending magnet has a finite length, the emitted radiation is expanded to a fan (figure 3.2). Therefore aperture slits are required to define the beam width at the experimental end station. In case of deep x-ray lithography, the beam can reach a width of 100 mm and more to enable full-wafer exposure of 4 inch or 6 inch wafers [7].

An outlet-chamber is attached at the bending magnet tangentially to the electron orbit in order to extract the radiation. As the storage ring is operated under UHV conditions, the beamline also has to be evacuated to the storage ring pressure in order to avoid a disturbance of the ring vacuum.

Apart from bending magnets there exist so-called insertion devices generating high intensive synchrotron radiation. These devices are wigglers and undulators. They are described in detail by Wille and Als-Nielsen et. al. [28, 31].

3.2. Theory of x-ray scattering

As x-ray reflectivity measurements were performed on the negative photoresist SU-8, the theory of x-ray scattering is outlined focussing on reflectivity measurements. A detailed description is given in [31, 32].

X-ray scattering from surfaces can be described by the kinematic approximation, also called first order Born approximation. This theory describes the scattering process for scattering angles about three times larger than the critical angle of external total reflection α_c [32] and solely considers single scattering.

The scattering from surfaces and interfaces is discussed assuming a discontinuous electron density transition between the interfaces with a constant electron density ρ below and above the interface. Thus, the scattering amplitude $A(\vec{q})$ of the scattered radiation is given by the Fourier transformation of the electron density in the scattering volume [33]

$$A(\vec{q}) = -r_0 \int_V \rho(\vec{r}) e^{i\vec{q}\cdot\vec{r}} d^3r \tag{3.10}$$

with r_0 as the classical electron radius defined by [31]

$$r_0 = \frac{e^2}{4\pi\epsilon_0 mc^2} = 2.818 \cdot 10^{-15}\,\mathrm{m}\,. \tag{3.11}$$

Here, e is the elementary charge of the electron, m the electron mass, ϵ_0 denotes the dielectric constant of the vacuum, and c is the velocity of light.

The differential cross section $\frac{\mathrm{d}\sigma}{\mathrm{d}\Omega}$, which is proportional to the scattered intensity per solid angle element, is defined by the absolute square of the scattering amplitude. Characterizing a rough interface by a height-height correlation function, the scattering cross section can be separated into two parts [34]

$$\frac{\mathrm{d}\sigma}{\mathrm{d}\Omega} = \left(\frac{\mathrm{d}\sigma}{\mathrm{d}\Omega}\right)_{\mathrm{spec}} + \left(\frac{\mathrm{d}\sigma}{\mathrm{d}\Omega}\right)_{\mathrm{diff}}, \tag{3.12}$$

describing the specular scattering $\left(\frac{\mathrm{d}\sigma}{\mathrm{d}\Omega}\right)_{\mathrm{spec}}$ and the diffuse scattering $\left(\frac{\mathrm{d}\sigma}{\mathrm{d}\Omega}\right)_{\mathrm{diff}}$.

Therefore, it is important to determine the diffuse scattered intensity separately during an x-ray reflectivity experiment to obtain the pure specularly scattered intensity. The specular cross section can be written as [34]

$$\left(\frac{\mathrm{d}\sigma}{\mathrm{d}\Omega}\right)_{\mathrm{spec}} = \left(\frac{\mathrm{d}\sigma}{\mathrm{d}\Omega}\right)_{\mathrm{F}} e^{-q_z^2\sigma^2} \tag{3.13}$$

yielding for the reflectivity R

$$R = R_{\mathrm{F}}\, e^{-q_z^2\sigma^2}\,. \tag{3.14}$$

Thus, the specularly scattered intensity R is described by the reflectivity of a smooth surface (Fresnel reflectivity R_{F}) that is damped by a Debye Waller like factor containing the surface roughness σ of the sample. The wave vector transfer perpendicular to the surface is given by

$$q_{\mathrm{z}} = \frac{4\pi}{\lambda}\sin(\theta) \tag{3.15}$$

where θ denotes the incidence angle of the radiation.

Considering a substrate covered by a layer, the cross section for the specularly scattered intensity, i.e. the reflectivity, can be expressed as [34]

$$\left(\frac{\mathrm{d}\sigma}{\mathrm{d}\Omega}\right)_{\mathrm{ref}} = \frac{1}{q_z^2}\left(\Delta\rho_1^2 e^{-q_z^2\sigma_1^2} + \Delta\rho_2^2 e^{-q_z^2\sigma_2^2} + 2\Delta\rho_1\Delta\rho_2 \cos(q_z l_m) e^{-\frac{1}{2}q_z^2(\sigma_1^2+\sigma_2^2)}\right)\,. \tag{3.16}$$

$\Delta\rho_{1,2}$ define the electron density differences at the interfaces and $\sigma_{1,2}$ are the corresponding interface roughnesses. The last term in equation 3.16 describes the interference of the radiation scattered at different interfaces yielding so-called Kiessig fringes, i.e. oscillations in the reflectivity curves. The distance (Δq_{z}) between the oscillation minima provides information about the layer thickness $d = \frac{2\pi}{\Delta q_{\mathrm{z}}}$ [34, 35].

Assuming two different interfacial roughnesses with $\sigma_1 < \sigma_2$, the scattered intensity at high q_z-values provides information on the smallest interfacial roughness, as the term in equation 3.16 containing $e^{-q_z^2\sigma_1^2}$ is dominant for high wave vector transfers. Thus, investigating $\ln\left(\frac{R}{R_{\mathrm{F}}}\right)$ as a function of q_z^2 at high q_{z} values yields information on the smoothest interface in the system (see equation 3.14).

The simulation of reflectivity curves is feasible by recursive algorithms (e.g. Parratt algorithm) and realized within the software LSFIT [36]. As this program was used to determine the Fresnel reflectivities for the investigated SU-8 sample system the algorithm used by LSFIT is described in the attachment A.1.

3.3. Scanning electron microscopy

For the investigation of nano and micro structures the imaging of these three dimensional systems is of great interest. Scanning electron microscopy (SEM) is a well suited technique for this purpose. Although it generates a two-dimensional image, it creates a spatial impression due to its high depth of field. It can be used to obtain a sample overview as well as to magnify areas of interest.

The SEM operates under vacuum, typically at a pressure of 10^{-5} mbar [37]. Electrons are emitted by an electron gun (mostly tungsten) and are accelerated from the cathode to the anode by an applied voltage of 1 - 50 keV [38]. On their way to the sample they are focused by an electromagnetic lens system consisting of 1 - 2 condenser lenses and an objective lens underneath (figure 3.3) [37–39]. Deflection coils, i.e. two pairs of magnet coils, scan the electron beam across the sample surface.

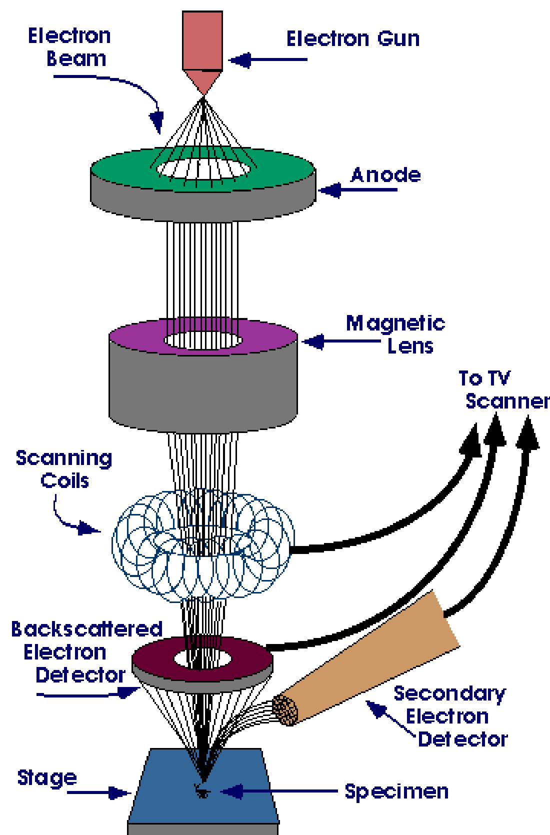

Fig. 3.3.: Setup of a scanning electron microscope. The electron beam is focused by electromagnetic lenses and deflected by scanning coils. Different detectors register the different types of radiation generated in the sample [40].

To compensate the limited maximum deflection of the electron beam, the sample stage can be moved in all three spatial directions. In addition, the sample can be tilted and rotated yielding a precise sample adjustment. The electron beam has a diameter of 1 - 10 nm and a current of $10^{-10} - 10^{-12}$ A at the sample surface [38].

The primary electron beam strikes the specimen and penetrates it to a depth of about 0.1 - 10 µm depending on the electron energy and the sample density [38]. The electron beam generates different kinds of electrons and x-rays in the sample, i.e. secondary electrons (SE), backscattered electrons (BSE), Auger-electrons (AE) as well as characteristic x-rays and bremsstrahlung (figure 3.4) [37–39]. The emerging electrons and x-rays are registered by different detectors and provide several information about the specimen. SE and AE are generated in the surface near region, that is within the first few nm of the sample. BSE are created in a depth of several 100 nm and x-rays originate from up to 1 µm deep regions [39]. Information concerning the sample's material composition can be obtained from SE, BSE, AE and x-rays.

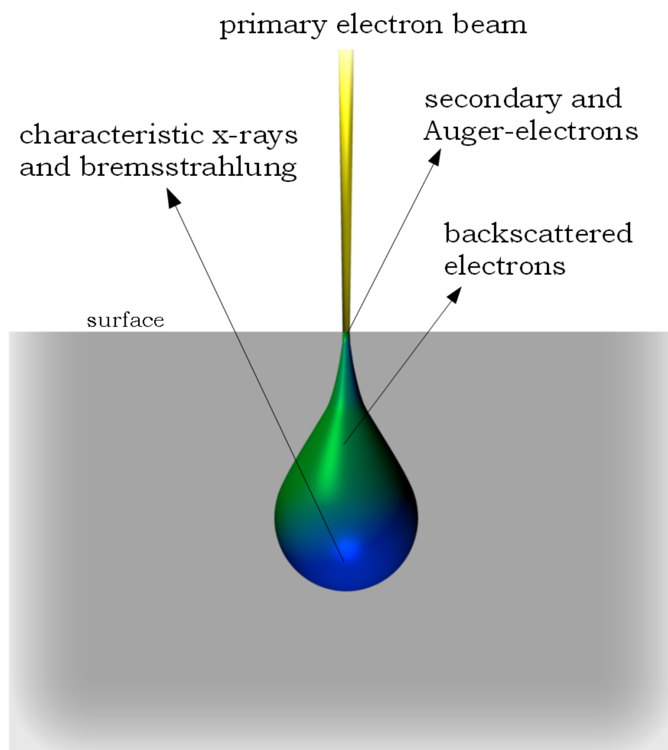

Fig. 3.4.: The primary electron beam strikes the sample and generates different kinds of emitted electrons as well as x-radiation. The electrons and x-rays originate from different depths in the sample.

As in common SEM only detectors for SE and BSE are installed, these electrons are discussed in more detail. In order to obtain a sample topography, SE as well as BSE can be used. The resolution limit is given by the size of the primary electron beam and is therefore in the order of a few nm [37–39]. The energy of SE is less than 50 eV and BSE have an energy in the range from 50 eV up to the energy of the primary electron beam ($E = eU$ (e: elementary charge, U: acceleration voltage)) [38, 39].

Secondary electrons are detected by a so-called Everhart-Thornley detector (ETD). The detector consists of a grid with an applied voltage between +100 V and +200 V which serves as a collection field for the SE. As the scintillator behind the grid is biased with 10 kV, the electrons are accelerated to the scintillator. The photons generated by the scintillator are registered by a photomultiplier and converted into a signal, which is imaged on the monitor [38, 39]. As the BSE have a high energy they are almost unaffected by the collection field of the Everhart-Thornley detector.

The image brightness depends on the electron yield. Therefore, areas with a high electron emission appear brighter than areas with a low electron emission. Furthermore, electrons generated near the detector can be detected easier than electrons from farther regions. Therefore, structures near the detector appear brighter and the observer obtains a three dimensional impression of the sample surface topography [37].

BSE are also used for topographic imaging. In addition, they are carrying information about the elemental material composition at the point of impact, because the BSE yield depends on the atomic number of the material. Therefore, the different materials in the sample are imaged with different intensities [39][37]. A disk shaped semiconducting detector or a pair of semiconducting detectors, mounted above the sample, register the BSE. The disk shaped detector is divided in two sections A and B. By different combination of the signals received in A and B (or in the two separated detectors) either the topographic or the composition information is obtained [39].

Topography imaging is influenced by a sample tilt, shadowing, and structure edges. The electron yield of the sample depends on the sample tilt with respect to the primary electron beam. Low energy SE do not create shadows, whereas BSE generate sharp shadows depending on the detector direction. Small topographic inhomogeneities as a result of edges, spikes etc. show an increased electron emission and are imaged as characteristic edge effects in SE images [38, 39].

The investigated specimens have to fulfill several requirements [39]. First, the sample must be stable under vacuum conditions. In addition, it should be clean, stable under electron bombardment and electrically conducting. Non-conducting samples are charged by the electron beam generating reflections on the sample surface. In order to investigate non-conductive materials the sample can be coated with a thin gold layer (10 - 20 nm) which is evaporated or sputtered on the surface [37, 39].

The working distance (WD), i.e. the distance between the last condenser lens and the specimen, has to be adapted to the investigation requirements [37]. A small WD of 5 - 8 mm improves the image sharpness at high magnifications, but it results in a lower depth of field and a worse signal, as the electrons emitted by the sample hit the pole shoe of the objective lens. A high WD of 40 - 50 mm offers an improved depth of field. However, the signal is decreased due to a high distance to the detector and the sensitivity to scatter fields at high magnifications is increased. The common and established working distance is 10 - 20 mm.

3.4. Confocal microscopy

The technique of confocal microscopy is well suited for a three dimensional investigation of surfaces. Especially the determination of surface roughnesses down to the nanometer scale is an important feature of this method [41]. As confocal microscopy is a contact-less technique in contrast to tactile profiling methods, it is possible to scan samples with very smooth surfaces without scratching them [42]. It is a widely used device in industrial quality control, providing a feasible resolution in the range of a few nm [41, 43].

The first type of confocal microscopes was invented by Minsky in 1955 [44]. The basic principle is the investigation of one single point at the specimen in the focal point. The general setup of a confocal microscope is shown in figure 3.5.

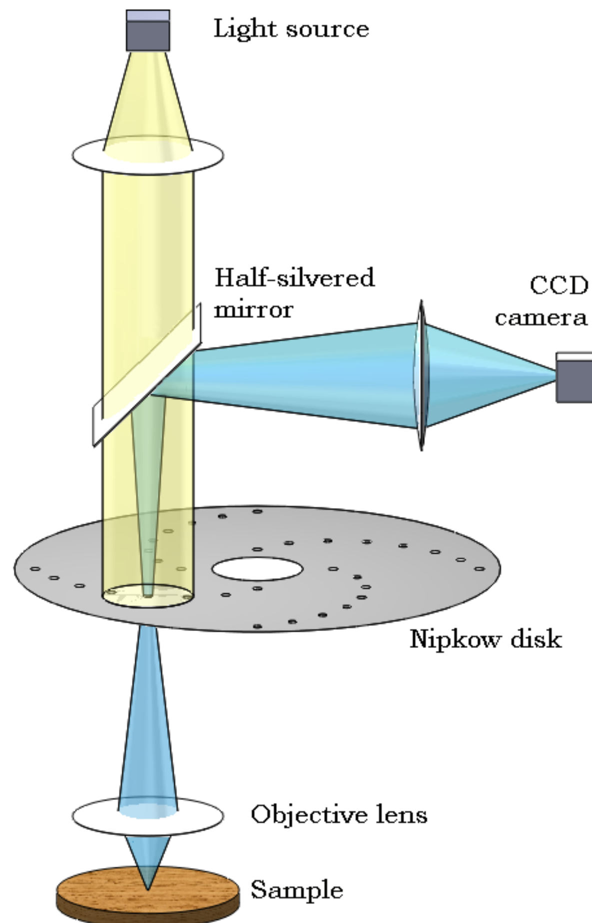

Fig. 3.5.: General setup of a confocal microscope. The light beam passes the Nipkow disk and the spots are focussed on the surface. The reflected radiation also passes the disk and is deflected by a half-silvered mirror to the CCD camera.

Light (e.g. from a Xenon lamp [41]) passes a multi pinhole disk (called Nipkow disk) [41, 43, 45]. This disk contains several holes arranged in a spiral along the disk edge. The pinhole apertures are imaged on the specimen by an objective lens. The light reflected by the sample is imaged by the objective lens to the Nipkow disk which has to be passed again. The light is then deflected to a CCD camera by a half-silvered mirror.

However, solely light emerging from the focal point of the sample can enter the pinhole apertures. Scattered radiation as well as light coming from points outside the focus are absorbed by the opaque disk regions [44, 45]. Due to this spatial filtering the depth of field is much improved compared to common microscopes. The focal points of the excitation system and the detection system are the same and thus the method is called confocal.

As the Nipkow disk rotates around its center, several picture elements can be investigated simultaneously [41, 43, 45]. By moving the sample along the axial direction, an intensity image of the specimen is taken at discrete distances. A subsequent software algorithm calculates the height information from the intensity images for every picture element and generates a three dimensional topography of the sample surface [41].

The functional material properties are often influenced by their surface characteristics [41]. Several surface parameters obtained by quantitative investigations of depth and roughness profiles are standardized by DIN EN ISO regulations [41, 42]. The most important DIN standards for surface characterizations are DIN EN ISO 3274 and 4288 [42, 46]. Important roughness parameters are R_a and R_q, defining the arithmetic mean (a) and root mean squared (q) roughnesses. They are calculated by [46, 47]

$$R_\mathrm{a} = \frac{1}{l}\int_0^l |z(x)|\, dx\,, \tag{3.17}$$

$$R_\mathrm{q} = \sqrt{\frac{1}{l}\int_0^l |z(x)|^2\, dx}\,, \tag{3.18}$$

where $z(x)$ describes the profile function along the measuring direction x and l the measuring length.

4. Setup of Beamline BL 1

The main aspect of this thesis was the setup of a dedicated deep x-ray lithography beamline at the synchrotron radiation source DELTA. Therefore, DELTA is shortly introduced at the beginning of this chapter. Afterwards the lithography beamline setup is described. It includes the presentation of the several required beamline hardware components (section 4.2) and the description of the control systems for beamline operation (section 4.3).

4.1. The storage ring DELTA

DELTA is a synchrotron radiation facility located at the campus of the Technische Universität Dortmund. It is operated by the center of synchrotron radiation involving the chair for accelerator physics and experimental solid state physics E1 of the TU Dortmund.

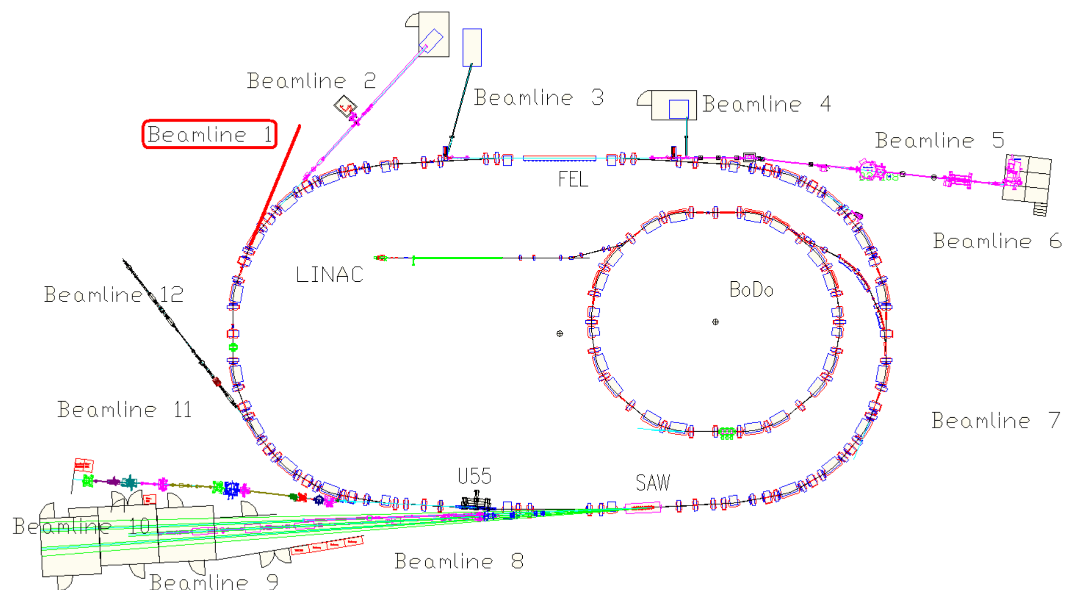

Fig. 4.1.: The schematic layout of DELTA and the beamline positions are shown. The new DXRL beamline BL 1 in the upper left corner is highlighted in red.

The three main components of the electron storage ring are the linear accelerator (Linac), the booster synchrotron (BoDo) and the storage ring (Delta). The Linac accelerates the electrons to an energy of 75 MeV. In the booster synchrotron, which has a circumference of 50.4 m, they are accelerated to an energy up to 1.5 GeV. The storage ring itself has a circumference of 115.2 m. The electrons can be stored with an arbitrary energy between 300 MeV and 1.5 GeV. The typical operation mode is at 1.5 GeV with an electron beam current of 130 mA. At these parameters lifetimes higher than 10 hours are possible [48].

The schematic layout of DELTA is shown in figure 4.1. In addition the beamline positions are depicted. The new deep x-ray lithography beamline BL 1 is located in the upper left corner. It is marked in red for better clarification.

4.2. Beamline hardware setup

Beamline BL 1 at DELTA was built as a dedicated deep x-ray lithography beamline. The beamline uses the white spectrum of a 1.5 T bending magnet. As shown in section 3.1, the deflection radius of the bending magnet can be calculated from equation 3.6. Due to an electron energy of 1.5 GeV and a magnetic field of 1.5 T, the deflection radius is $R = 3.3356$ m. The critical energy is $E_c = 2.2$ keV, corresponding to a critical wavelength of $\lambda_c = 5.5\,\text{Å} = 0.55$ nm. This energy region is well suited for DXRL in order to produce high aspect ratio micro structures, see section 2.3.1.

BL 1 has an overall length of 14 m from the source point in the bending magnet to the wafer location at the experimental end station (figures 4.2 and 4.3). The vertical beam position is 1210 mm from the floor.

The first beamline part contains the section from the source point to the first valve V_0. This section includes the outlet chamber and the photon absorber and has already been constructed by the machine group of DELTA. Thus, the beamline was planned and constructed from V_0 to the experimental end station in the experimental hutch. The whole beamline therefore consists of five vacuum sections.

- section 0: This is the section built by the machine group (source point up to V_0). As it was not constructed within this work it is referred to as section 0. The actual section numbering therefore starts with section 1 behind the valve V_0.

- section 1: The section starts at the first valve V_0 behind the outlet chamber and ends at the all-metal-gate valve V_1 behind the radiation protection wall.

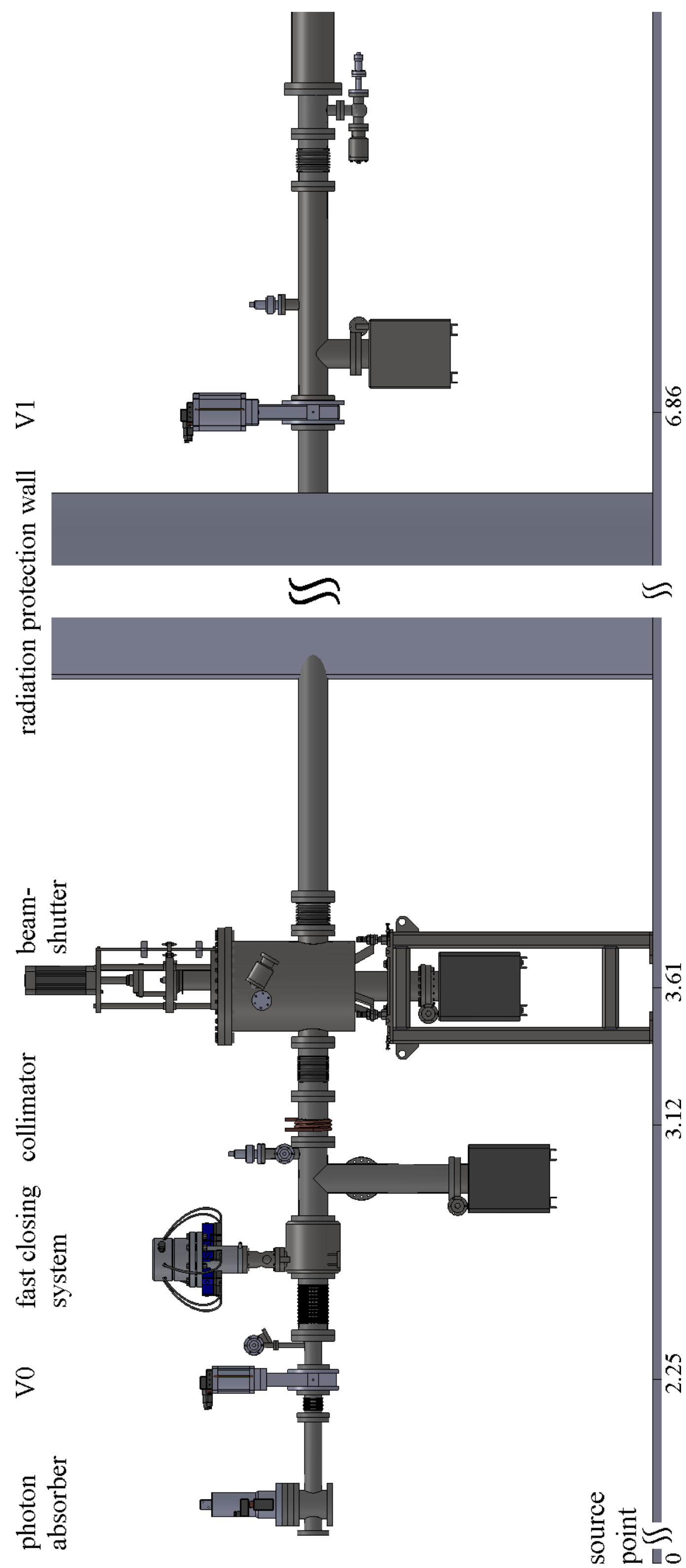

Fig. 4.2.: First part of the schematic drawing of the BL 1 setup. The front end (photon absorber, valve V_0, fast closing valve), the collimator, the beamshutter, and the valve V_1 are shown. The position of the radiation protection wall is depicted as well.

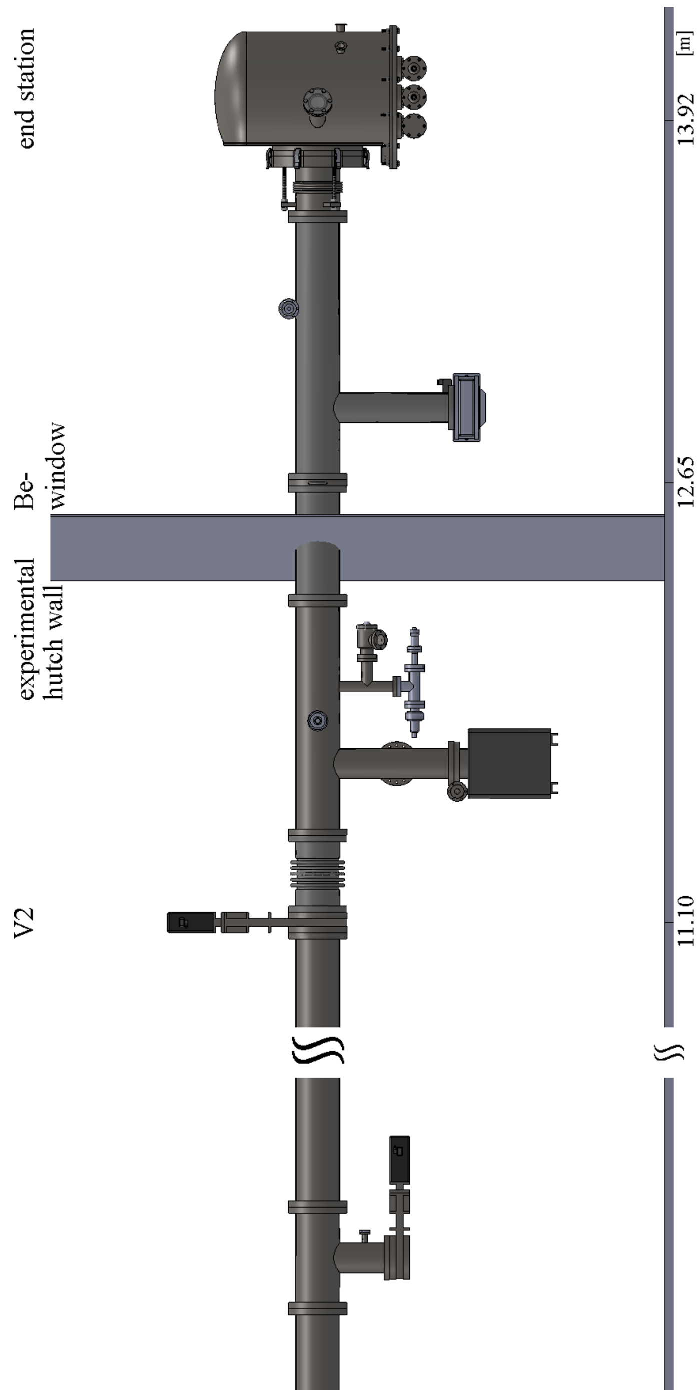

Fig. 4.3.: Second part of the scheme of BL 1. The valve V_2, the beryllium window, the experimental end station and the wall of the experimental hutch are shown.

- section 2: This beamline part proceeds until the gate valve V_2 in front of the experimental hutch.
- section 3: Starting at the end of section 2, it ends at the beryllium window.
- section 4: The last section ranges from the beryllium window to the experimental end station.

Photographs of the real setup are presented in figure 4.4. The first picture (figure 4.4(a)) gives an impression of the beamline section inside the storage ring. It shows the main components like fast closing system, collimator and beamshutter. The beamline sections outside the radiation protection wall are shown in figure 4.4(c). On the left side the beamline enters the experimental hutch. The setup inside the hutch is presented in figure 4.4(b). The first beamline component on the right side is the water cooled beryllium window and the last component is the end station.

The recipients, as the vacuum chambers are called, are made of stainless steel (Ultron by the company Dockweiler) and were cleaned and subsequently filled with N_2 for delivery. The arithmetic mean roughness R_a of the inner recipient surface is less than 0.25 μm. These quality features are necessary to obtain ultra high vacuum. The terms DN 63, DN 100 and so on describe the nominal recipient diameter in millimeter.

The most important components in section 1 are the adapter from DN 63 to DN 100, the fast closing system, the collimator, and the beamshutter. The intermediate recipients are vacuum pipes and bellow expansion joints (abbr. bellow). The bellows are required in order to enable a position correction between two components and to ease a possible change in the setup of a section. The second and third section mainly consist of recipients. The two main parts are another adapter from DN 100 to DN 150 in section 2 and the water cooled beryllium window as separation between the vacuum sections 3 and 4. The last section is built by a recipient and the experimental end station. All constituents along the beamline are connected by flanges with copper sealing rings. The screws (mainly M8) at the flanges are tightened with 18 Nm. In order to avoid an unintended screw fixing, mainly initiated by surface rust, all screws used at the recipient are silver plated.

Every section has two vacuum sensors: one for the low vacuum range (Pirani gauge head) and one for the high vacuum range (cold cathode gauge heads). There are four stationary mounted ion getter pumps along the beamline: two in section 1 and one each in sections 2 and 3. As the vacuum in section 4 does not has to meet very high demands, it is sufficient to

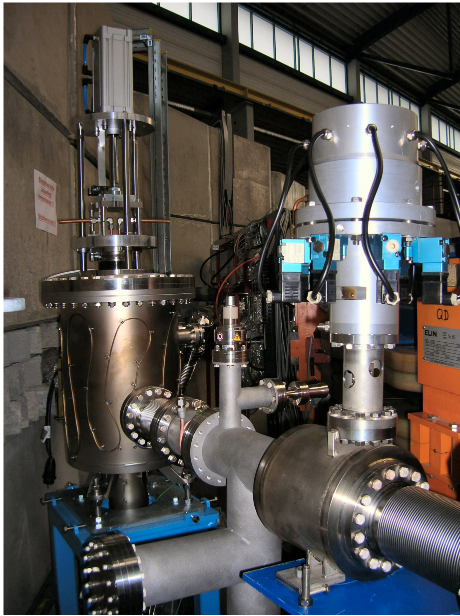

(a) Beamline setup within the storage ring

(b) Setup in the experimental hutch

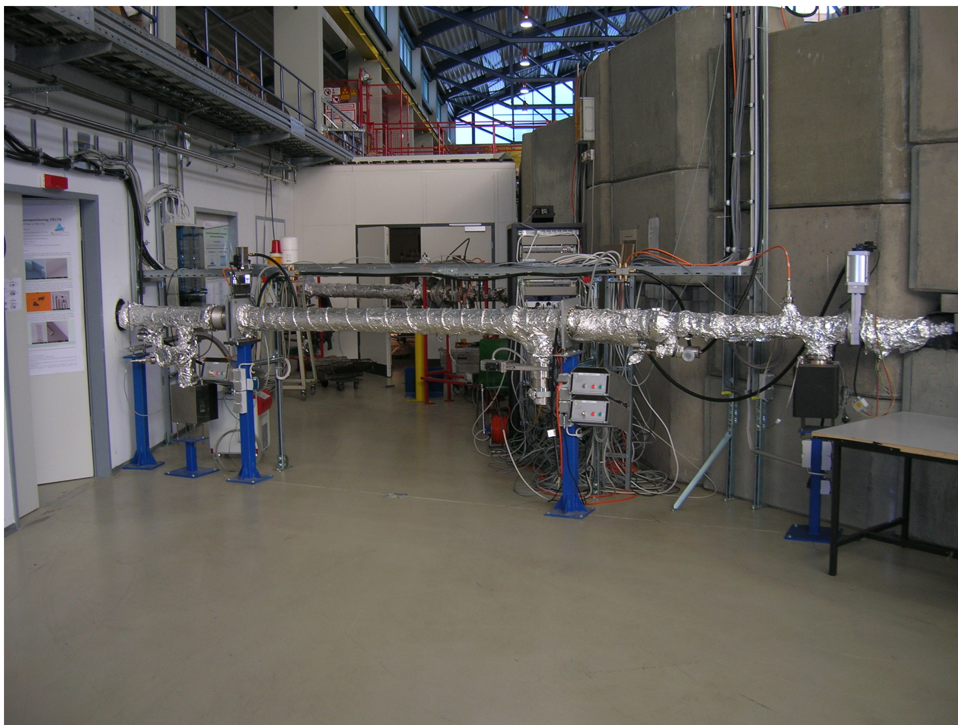

(c) Setup outside the storage ring

Fig. 4.4.: Photographs of the individual beamline sections. (a) Beamline setup in the section located in the storage ring. It shows the main components like fast closing system, collimator and beamshutter. (b) The experimental hutch contains the last beamline section from the beryllium window to the end station. (c) Beamline section outside the radiation protection wall. On the left side the beamline enters the experimental hutch which is located behind the gypsum wall.

use a turbo pump. In addition, every section has a device to vent or to evacuate the section. If a section has to be vented, this has to be performed with dry nitrogen to avoid a pollution of the recipient walls. The dry nitrogen covers the walls and serves as a protection layer. Therefore, the subsequent evacuation and bake-out of the section is much easier and faster. The individual components are described in more detail in the following.

4.2.1. The valves

Beamline 1 consists of three main valves, namely V_0, V_1 and V_2. In addition two valves are installed at recipient extractions in section 2 and 4. The main components of all these valves are made of stainless steel. As it is not allowed to use viton or other elastomer seals in the first beamline section, V_0 and V_1 are all metal gate valves [49]. They are well suited for extreme UHV and can be heated up to 200°C. However, the control valve and the position detector must not be heated higher than 80°C. To open these valves, the pressure difference before and behind the valve has to be less than 500 mbar. V_0 has a size of DN 63 and V_1 is used for a DN 100 recipient. The valve at the extraction in section 4 is a DN 100 all metal gate valve. The valve installed at the extraction in section 2 is a DN 100 valve and V_2 is a DN 150 valve. Both latter valves are viton sealed UHV valves and can be heated up to 200°C with exception of the control valve and the position detector (50°C and 80°C, respectively). The maximum permitted pressure difference for the valve opening is less than 30 mbar.

All-metal-angle valves with a size of DN 40 are installed along the beamline, one in each vacuum section. They are used either for controlled venting with dry nitrogen or to install a turbo pump. This pump generates an adequate fore pressure required before starting the ion getter pumps for UHV (section 4.2.7). These angle valves are operated manually, whereas the other valves are operated with a voltage of 24 V and compressed air.

4.2.2. The photon absorber

The photon absorber is the first component behind the outlet chamber and is part of the BL 1 front end. It absorbs the synchrotron radiation generated in the bending magnet in order to protect the valves in the beamline, especially V_0 as the first valve in the section. During beamline operation, the photon absorber and the beamshutter are the last components to be opened in order to allow the radiation to enter the recipient of BL 1.

The photon absorber is made of a copper plate with a water cooling loop at its back [49]. The maximum allowed power density is 25 $\frac{\mathrm{W}}{\mathrm{mm}^2}$ and the total allowed power input is 7 kW. This is sufficient as the power density of BL 1 is 0.81$\frac{\mathrm{W}}{\mathrm{mm}^2}$. The photon absorber is operated with compressed air and has a closing time of 1 second. As the photon absorber has no welded or brazed seam between the loop for the water cooling and the vacuum, it is suited for UHV applications.

4.2.3. The collimator

The collimator, defining the beam width at the end station, consists of a copper block with a special shaped aperture (figure 4.5). The copper block is vacuum brazed to a recipient on both sides. A cooling coil with two and a half turns is applied at the outer side of the copper block. The tube is made of copper and has a diameter of 10 mm. The coil is connected to the water cooling system of BL 1.

The aperture has a height of 16 mm and a width of 26 mm. As the full vertical opening angle of the synchrotron radiation is given by equation 3.9, yielding a beam height of about 10 mm at the end station, the beam is not limited by the collimator in vertical direction. Thus, the full beam height for exposure is guaranteed. The collimator has to reduce the horizontal beam

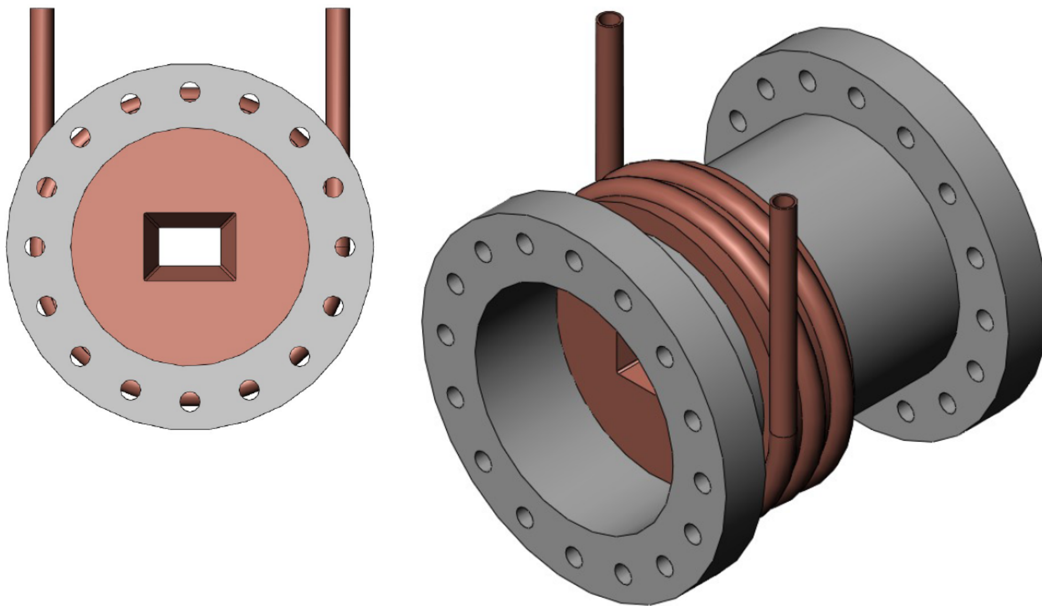

Fig. 4.5.: Drawing of the collimator. The water cooled copper block has an aperture of 26 x 16 mm^2. It reduces the horizontal opening angle of the beam from 26.2 mrad to 8.7 mrad, yielding a beam width of 120 mm at the end station. A cooling coil is installed at the outside of the collimator.

width in such a manner that the width is 120 mm at the end station, assuring a full-wafer exposure of 4 inch wafers. Due to the outlet chamber the beam has a horizontal opening angle of 26.2 mrad.

The collimator is positioned in a distance of 3.12 m from the source point with a horizontal aperture dimension of 26 mm, reducing the horizontal beam divergence to 8.7 mrad. The smallest aperture section is beveled, building the incoming and outgoing part of the aperture. This shape reduces the effect of scattering at the aperture borders. The angle of inclination is 30° with respect to the aperture faces. The collimator can be baked out up to 160°C. It is made by the company Reuter Technologie in Germany in accordance with the stated requirements.

4.2.4. The beamshutter

The task of the beamshutter is to absorb all radiation coming from the bending magnet and passing through the beamline in case of beamline operation and without a running experiment. The position of the beamshutter center is 3.61 m behind the radiation source point. It is the last component in the inner region of DELTA, i.e. in front of the radiation protection wall with respect to the beam direction. The full beamshutter length is 400 mm. The inner part of the beamshutter (figure 4.6) consists of a 240 mm long absorber block made of tungsten corresponding to a lead equivalent of 300 mm in accordance with the radiation protection requirements. The outer diameter of the tungsten block is 130 mm. The block has an overlap of 15 mm with the following DN 100 beamline recipient to guarantee a complete beam coverage.

A water cooled copper plate in front of the tungsten block dissipates the heat from the striking radiation. The beam power is calculated considering equation 3.5. As the horizontal opening angle of the beam is reduced to 8.7 mrad by the collimator, the total beam power is about 56 W, considering a beam current of 300 mA to guarantee an operational reliability even at higher beam currents than usual. The beam has a width of approximately 30 mm and a height of 2.3 mm at the beamshutter entrance, i.e. at the position of the cooling copper plate. Therefore, the calculated power density is 0.81 $\frac{\text{W}}{\text{mm}^2}$.

The beamshutter has an adjustability of ± 10 mm in three spatial directions. The outside of the absorber chamber is covered with heating wires which allow a beamshutter heating up to 200°C. The beamshutter is a custom product of the company FMB in Berlin, Germany.

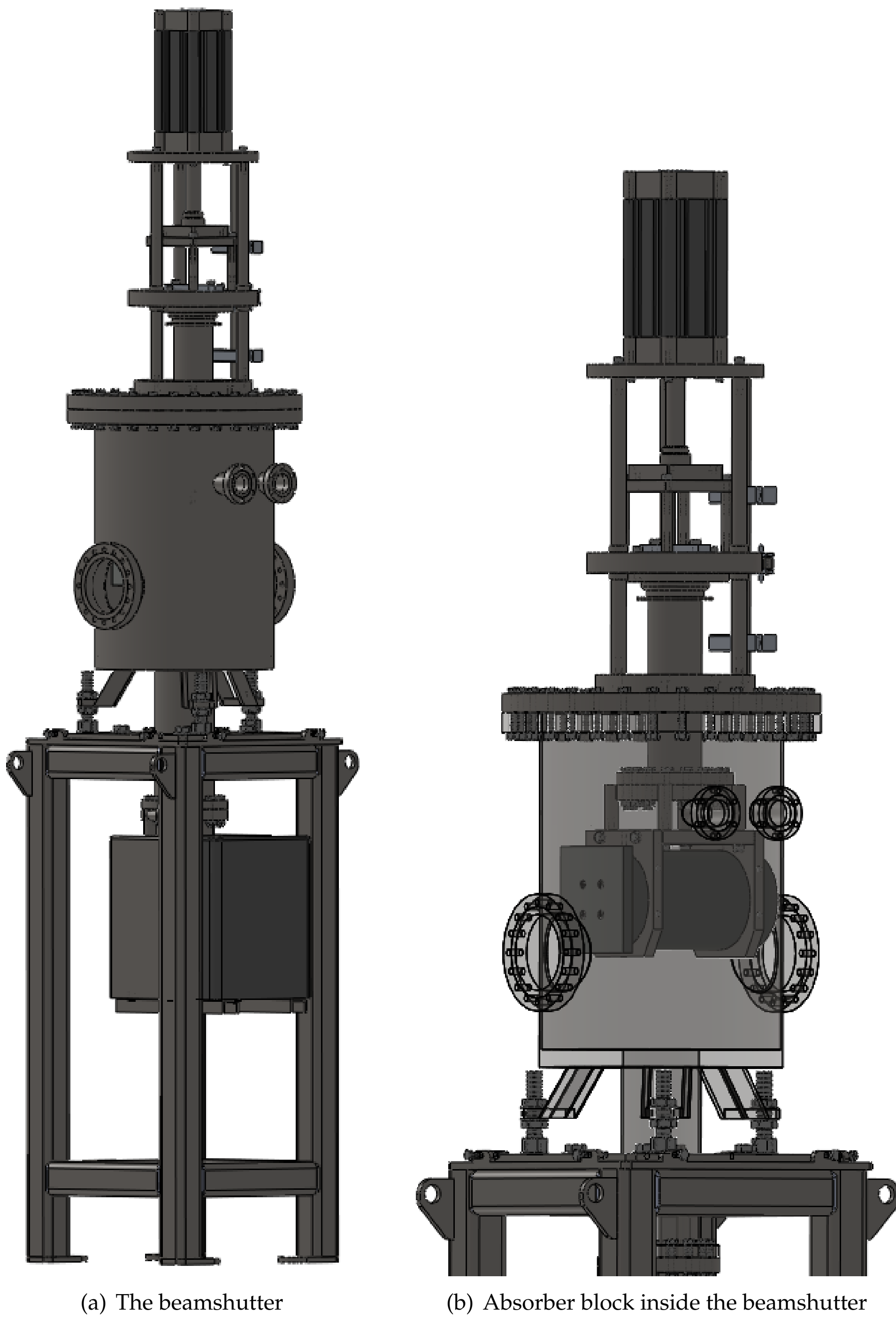

(a) The beamshutter (b) Absorber block inside the beamshutter

Fig. 4.6.: Beamshutter with the absorber block inside. The tungsten absorber has a length of 240 mm corresponding to 300 mm of lead.

4.2.5. The beryllium window

To exclude the long-wavelength radiation at the exposure end station at BL 1, a filter is necessary. This filter has to fulfill special requirements. It has to reduce the low energy radiation as this radiation region causes thermal heating of the x-ray mask and the exposed wafer, leading to distorted structures. However, the Be window has to let pass the radiation above 2 keV, as the energy region around 2 keV is well suited for deep x-ray lithography. It must have a good breaking resistance, as the window also serves as a separation between the ultra high vacuum region of the beamline and the high vacuum section at the end station. The end station is vented for wafer exchange up to atmospheric pressure. A minimum beryllium thickness of 127 μm guarantees a safety factor of two in breaking resistance.

The emitted spectrum of a 1.5 T DELTA bending magnet is shown in figure 4.7. For the calculation a beam current of 130 mA is assumed. The solid line represents the unaffected dipole magnet spectrum with a maximum photon flux of $5.7 \cdot 10^{12} \, \frac{\text{photons}}{\text{sec mrad}^2 \text{ 0.1\%BW}}$ at an energy of 1.9 keV. Considering a beryllium window with a thickness of 127 μm, the obtained spectrum is given by the green dashed curve. The window absorbs the long-wavelength radiation below 800 eV and is nearly transparent for higher energies.

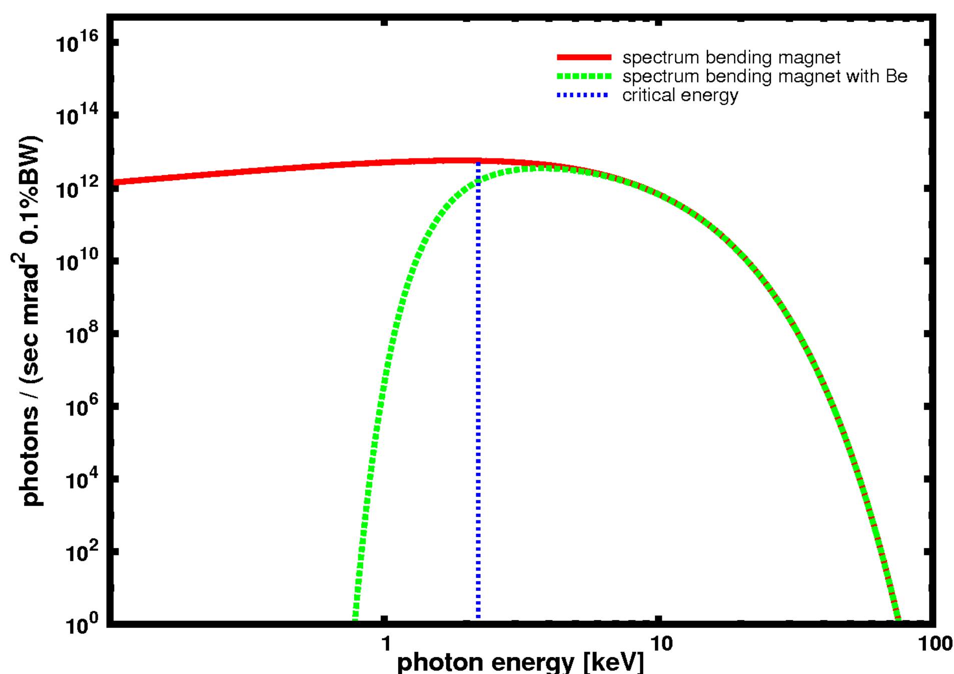

Fig. 4.7.: Photon spectrum of a 1.5 T bending magnet (solid line) at 130 mA beam current. The green dashed curve shows the spectrum considering a 127 μm thick beryllium window. The vertical line indicates the critical energy.

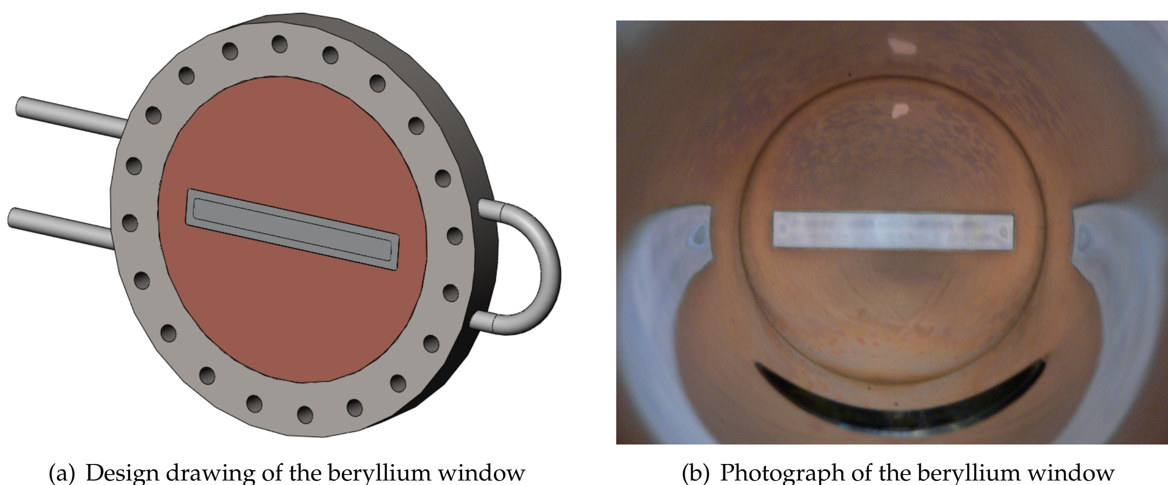

(a) Design drawing of the beryllium window (b) Photograph of the beryllium window

Fig. 4.8.: (a) Double sided DN 150 flange with the copper section and the diffusion bonded beryllium foil in its center. The copper section is actively cooled by a water circuit. (b) Photograph of the beryllium window embedded in the last beamline section. The rectangular inlet shows the beryllium foil which is diffusion bonded to the copper center section.

The window is made of a double sided 304L SST DN 150 ConFlat flange with a copper center section, brazed to the flange. The design drawing and a photograph of the Be window are shown in figure 4.8. The center section has an aperture of 10 x 110 mm^2 (vertically x horizontally), reducing the beam width to 115 mm at the experimental end station. The 127 μm thick beryllium foil is diffusion bonded to this aperture. As the copper center section is actively cooled, the cooling circuit is embedded around the beryllium window. The window is made of IF-1™ beryllium, with a minimum beryllium content of 99.8%. The window is bakeable up to 450°C and is leak tight to $1 \cdot 10^{-9}\ \frac{\text{atm cm}^3}{\text{sec}}$, tested with a helium mass spectrometer. The window is a custom product of the company Brush Wellman Electrofusion Products in California, USA.

4.2.6. The end station

The experimental end station constitutes the last beamline section. It is positioned in the experimental hutch at the end of BL 1 in about 14 m distance to the radiation source point. The applied exposure chamber (figure 4.9) is a device constructed by Körfer during the setup of the first lithography beamline in the early operation period of DELTA [1, 50]. It is made of aluminum and has connections for a vacuum pump and pressure sensors.

(a) The exposure chamber - in reality

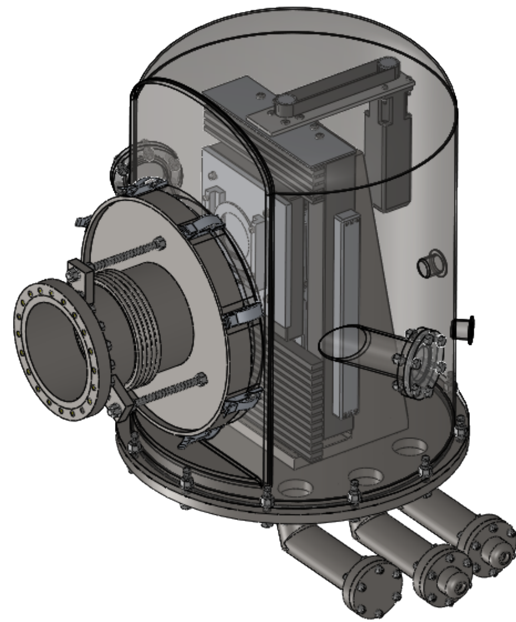

(b) The exposure chamber - design drawing

Fig. 4.9.: The exposure chamber is shown as a photograph (a) and as a reconstructed drawing (b). The wafer stepper inside the chamber is clearly visible in the design drawing.

(a) The wafer stepper

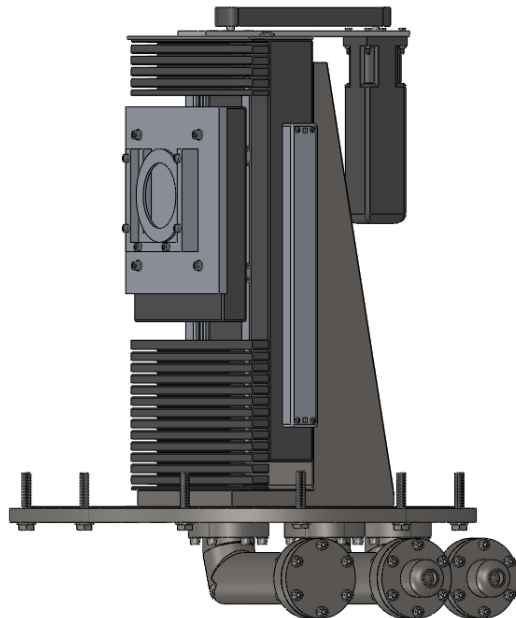

(b) The wafer stepper - design drawing

Fig. 4.10.: Photograph of the wafer stepper (a). The corresponding design drawing is depicted in (b). The adapter plate for the mounting of the wafer-mask system is fixed in front of the carriage.

In addition, the chamber contains a motorized wafer stepper (figure 4.10). This stepper has a maximum length of stroke of $\pm$ 93 mm from the center. The stepper contains a servo-motor that is amplified by a Bautz compact servo amplifier CSK 08. The enabling and disabling of the motor activity as well as the driving direction (up and/or down) is controlled via a relay box that is connected to the motor limit switches. When the motor reaches the limit switch the relay switches and reverses the moving direction. The moving speeds for the up and down direction are regulated separately. For a homogeneous exposure the speeds should be approximately the same.

An adapter plate is fixed at the stepper carriage in order to attach the carrier for the coated wafer and the x-ray mask (section 7.1).

4.2.7. The ion getter pumps and turbo pumps

The different types of vacuum pumps can be mainly summarized in two groups. In the first group are the gas transfer vacuum pumps which remove the gas molecules from the recipient and emit it into the atmosphere. The second group contains the gas binding vacuum pumps. Here, the gas molecules adsorb at the inner pump surface.

Two types of pumps are used at BL 1: a turbomolecular pump (gas transfer vacuum pump) and an ion getter pump (gas binding vacuum pump). The turbo pump (Pfeiffer Vacuum, TSU 261/MVP 055-3 TurboCube) consists of turbine-like rotors with bladed disks. The molecules collide with the blades, are adsorbed at the blades and leave them after a certain time. As the molecules need a mean free path length in the order of the blade spacing to guarantee a molecular flow, a fore pressure of 10^{-2} mbar is necessary [2, 51]. The pressure reachable with turbo pumps is in the range of 10^{-3} to 10^{-10} mbar.

Ion getter pumps (IGP) are used for ultra high vacuum. IGP's can pump noble gases as well as other inert gases. The working principle is as follows: Argon ions are accelerated to a titanium target. Thus, titanium atoms are sputtered from the target and condense at the inner pump surfaces, thereby binding the pumped gas molecules to the pump surface. Titanium is used as it has a high binding capacity and is rather inert in bulkform due to the oxide layer at its surface.

The ion getter pumps at BL 1 are VacIon Plus 150 (Varian) which need a fore pressure of less than 10^{-3} mbar and can reach a pressure below 10^{-11} mbar. They have a DN 100 flange and are bakeable up to maximum 350°C [52]. BL 1 consists of four IGP's which are permanently installed. The first two IGP's are in section 1, i.e. one pump is fixed in front of the collimator

and the second pump is attached beneath the beamshutter. The third ion getter pump is installed behind the valve V_1 and the last pump is mounted in the section between V_2 and the beryllium window. In addition, a turbo pump is used at BL 1 to generate the necessary fore pressures. This pump was attached to an extraction in the beamline section that should be evacuated.

4.2.8. The pressure measuring system

In order to measure the pressure inside the beamline, a system is used that is specialized for the application in accelerators. It is well suited for UHV and resistant to radioactive radiation and electromagnetic fields. Two different vacuum gauge heads measure the pressure at BL 1. Each beamline section consists of a Pirani gauge head (TPR 018) and a cold cathode gauge head (IKR 070). The former detects the pressure down to the HV region (1000 mbar down to $8 \cdot 10^{-4}$ mbar) and the latter quantifies the UHV region ($5 \cdot 10^{-3}$ mbar to $1 \cdot 10^{-11}$ mbar).

The pressure information is displayed by controllers (TPG 300 of the company Pfeiffer vacuum). One controller actuates the two Pirani gauge heads in section 1 and the one at the experimental end station as well as the cold cathode gauge head in section 1. The second controller monitors each one Pirani and one cold cathode gauge head in sections 2 and 3. An individual threshold is programmed for each gauge head, which defines the region of high vacuum. This information about the vacuum quality is transferred to the PLC (**P**rogrammable **L**ogic **C**ontroller) of BL 1 as it is important for the approvals for valve opening. The thresholds for the valve opening approvals are set for the cold cathode gauge heads as they are more reliable than the Pirani gauge heads and as they are well suited for the UHV region.

Two thresholds are set for each cold cathode. The first point defines the entry to the region of good vacuum at decreasing pressure and the second threshold defines the point when leaving this region at increasing pressure. At decreasing pressure the controller sends an OK signal to the PLC from $1 \cdot 10^{-7}$ mbar and lower. This OK signal is withdrawn at a pressure of $5 \cdot 10^{-6}$ mbar at increasing pressure. To protect the cold cathode from contamination in case of low vacuum, certain thresholds are programmed to make sure that the cold cathode switches off at high pressures. These limits are set to $1 \cdot 10^{-5}$ mbar and $5 \cdot 10^{-4}$ mbar. The first value defines the limit for the approval to initiate the cold cathode and the second value is the limit to switch it off.

Thresholds are programmed for the Pirani gauge heads as well. They signalize OK in case the pressure is in the region of HV or better. The two thresholds are set to $1 \cdot 10^{-3}$ mbar and $5 \cdot 10^{-3}$ mbar.

4.2.9. The fast closing system

In order to protect the UHV of the storage ring in case of a sudden pressure increase in the beamline of BL 1, a fast closing system is installed. A dedicated cold cathode gauge head is attached in front of the beryllium window as it is the most critical component concerning breakage. If the gauge head measures a sudden vacuum loss, it sends a signal to the fast closing valve in section 1 of BL 1. The sensor response time is about 2 - 3 ms and the valve closes within 17 ms [53]. The fast closing valve is fragile to obtain a short closing time and it is not resistant to synchrotron radiation. Thus, the photon absorber is closed immediately after the reaction of the fast closing system. The fast closing system consists of a water cooling connection which is solely necessary in case of a bake-out of this beamline section.

4.2.10. The electrical supply

Several power sockets are installed along the beamline. Two isolated electrical supplies separate the heating components and the power supplies for the permanent operating systems (PLC, valve and pressure controllers, pumps, etc.). The power sockets of the two supplies can be distinguished by their cover colors. The electrical supply for the heating circuit has blue covers and the supply for the permanent operating systems has gray covers. As some beamline components require a high power supply, six power sockets of the heating circuit are mounted along the beamline where each socket is interlocked with a 16 A fuse. Three of them are mounted in the inner storage ring region and three are installed outside the radiation protection wall.

4.2.11. The compressed air supply

Several components of BL 1 need compressed air for operation. These components are the valves V_0, V_1, V_2 and the valves at the recipient extractions, the beamshutter and the photon absorber as well as the fast closing valve. For this reason an adequate distribution system for compressed air is installed along the beamline. This supply is connected to the compressed air system of DELTA, which provides a pressure of about 5 - 6 bar.

4.2.12. The cooling water supply

The water cooling supply of BL 1 is connected to the cooling system of DELTA. Water cooling is required for the collimator, the beamshutter, and the beryllium window. As the distance between beamshutter and collimator is about 50 cm these two components are connected to one common water cooling circuit. The beryllium window is attached to a second cooling circuit. The flow rate is set to 5 $\frac{\mathrm{l}}{\mathrm{min}}$. Each cooling circuit consists of a flow controller which sends an OK signal when the flow is higher than 4 $\frac{\mathrm{l}}{\mathrm{min}}$. Two water monitoring systems shall be placed beneath the cooled components in order to detect a possible leakage. In case of a defect in liquid tightness the magnet valve in the corresponding cooling circuit will close and stop the water flow. The magnet valves as well as the water monitoring systems have to be installed in a next step.

4.2.13. The fulfilment of the radiation protection requirements

To comply with the radiation protection requirements, the following aspects have to be kept in mind: Solely the radiation coming from the outlet chamber and passing through the beamline is permitted to leave the storage ring. No other radiation, e.g. radiation deriving from scattering, is allowed to appear outside the storage ring. Therefore, the following assemblies are set up: The main barrier is built by the radiation protection wall. This wall consists of huge concrete stones with dimensions of 1500 x 1000 x 1100/800 mm^3 (LxWxH). This wall surrounds the whole storage ring and defines the border between the restricted area and the normal accessible region. In order to lead the beamline recipient through these stones, the stone at the height of the beam is removed. Instead, the free space is filled with small concrete stones of 200 x 100 x 80 mm^3 (figure 4.11(a)). The recipient is embedded between these stones. Thick strings of leaden fibers are pressed into the free spaces between the recipient and the small concrete stones. As a direct connection from the storage ring to the outer region has to be avoided (apart from the recipient), the stone arrangement must not contain straight grooves. Therefore, the offset pattern shown in figure 4.11(b) is chosen. Leaden plates and thick strings of leaden fibers are applied between the different layers of small concrete stones in order to seal the horizontal grooves. The layered system of the radiation protection wall is shown in figure 4.11(c).

In addition, a wall of lead blocks (200 x 100 x 50 mm^3) is constructed parallel to the recipient at the side pointing to the storage ring. It starts at the beamshutter exit and ends at the

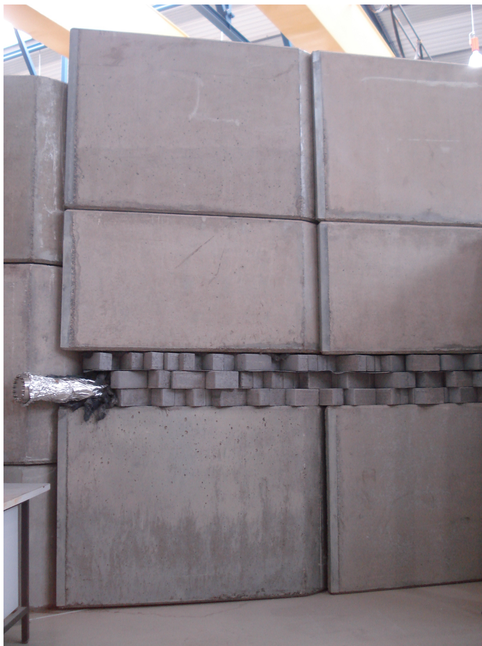

(a) The radiation protection wall

(b) Arrangement of the small concrete stones

(c) Layered system of the radiation protection wall

Fig. 4.11.: Setup of the radiation protection wall. (a) Position of the recipient in the radiation protection wall. It is embedded between small concrete stones surrounded by huge concrete blocks. (b) Arrangement of the small concrete stones. (c) Leaden fibres and plates are applied between the layers of concrete stones.

radiation protection wall. A shielding made of four lead blocks is installed around the recipient right behind the beamshutter exit in order to increase the overlap between the beamshutter lead block and the recipient. All these assemblies are necessary to ensure that no radiation, apart from the defined photon beam coming from the outlet chamber, can cross the radiation protection wall.

The experimental hutch is made of lead-aluminum sandwich plates. They consist of a 3 mm thick lead plate, covered with a 2 mm thick aluminum plate at each side. As it is not allowed to have any free view from inside the hutch to the room outside, the cable feedthrough is shielded by these lead-aluminum sandwich plates. A photograph of the exterior view of the experimental hutch is shown in figure 4.12.

Fig. 4.12.: Exterior view on the experimental hutch build of lead aluminum sandwich plates. The hutch encloses the last beamline section starting at the beryllium window.

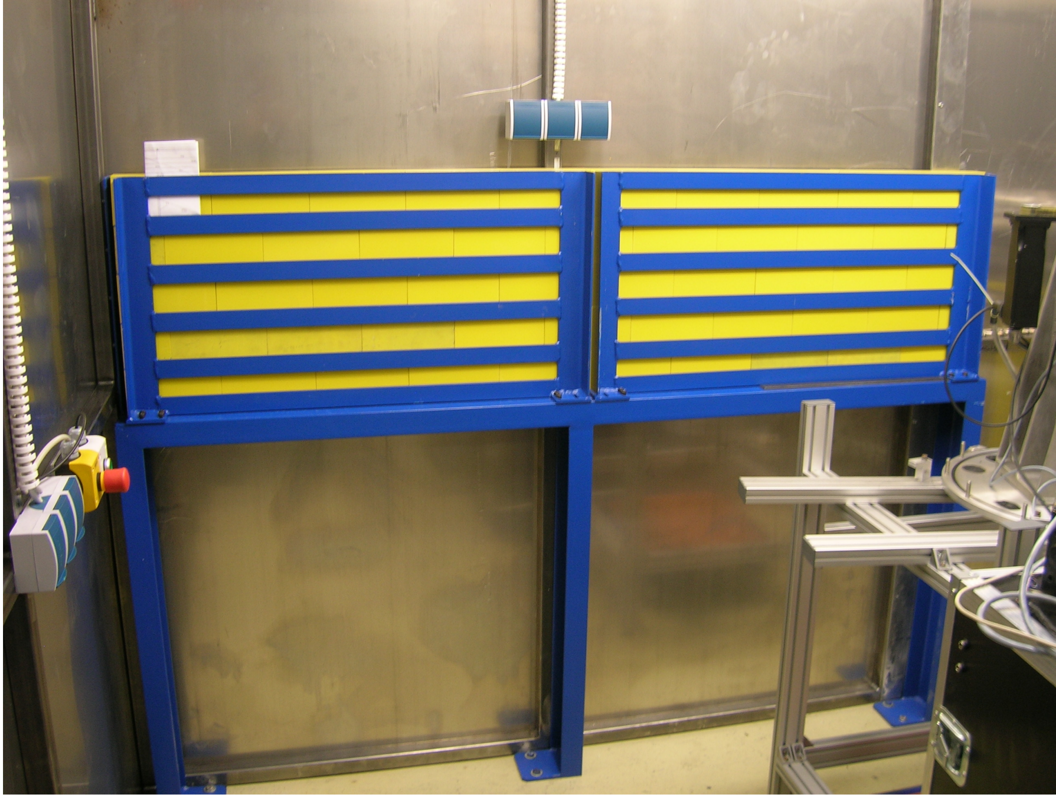

Fig. 4.13.: A wall of lead blocks is positioned behind the experimental end station as the final beam stop. It consists of 50 lead blocks.

Behind the experimental end station a wall of lead blocks is constructed in order to absorb any radiation passing through the end station (figure 4.13). It serves as the final beam stop. It is placed parallel to the experimental hutch wall. The center of this wall corresponds to the beam center. The wall height is ± 250 mm from the center. The protection wall must cover the entire beam cross section plus 300 mm at both beam sides. As the beam has a width of 110 mm and as it strikes the wall under an angle of about 22°, the wall must have a length of 2 meters.

4.3. The interlock and valve control system

Apart from the installed hardware of the beamline itself, a control system is necessary to operate the beamline. It consists of different components like an interlock control and a valve control system, a main relay board as well as a relay box. These components ensure a safe beamline operation, enable the remote control of beamline components like valves, beamshutter and photon absorber and exchange information between the beamline and the DELTA control system. The interlock control and valve control systems consist of adequate front panels shown in figure 4.14. The upper and lower front panels are part of the interlock control and the valve control system, respectively. The black board with the green and red LED's is the main relay board.

4.3.1. The interlock control

The interlock control system consists of a PLC managing the operation of the beamline and the safety system. In case of the interlock control system a Siemens Simatic S7-300 CPU 314 was applied in accordance with the DELTA safety requirements. The front panel design drawing of the interlock control system is shown in figure 4.15.

On the right side of the interlock front panel there is the master key to initiate the interlock control system and the emergency stop button. As the implementation of a frequent injection mode at DELTA is considered for future operation, a LED labeled FIM is installed in the upper left corner of the front panel which is green in case of FIM at DELTA. Below the FIM status LED, there is an orange window, labeled INJECTION. This window is illuminated during the injection procedure of DELTA. The orange key button below the injection status lamp is required for the initiation and the confirmation of the searching procedure. The searching procedure is an essential part of the safe beamline operation consisting of several steps. Before the start of an experiment, i.e. before the beam can enter the hutch, it is necessary to control that nobody remains in the hutch.

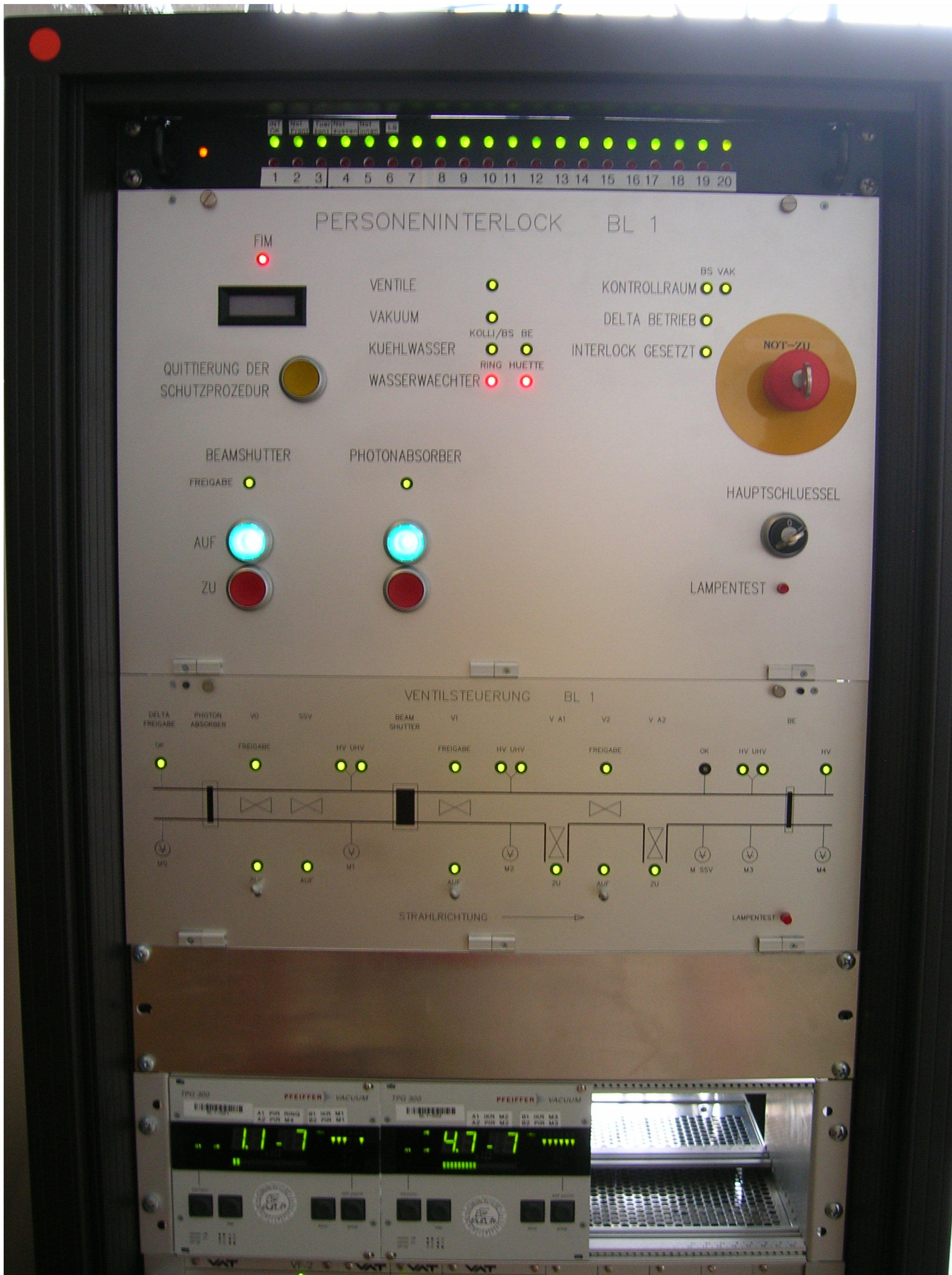

Fig. 4.14.: Front panels of the safety interlock (upper front panel) and the valve control system (lower front panel). The black top insert with the green (and red) LED's is the main relay board.

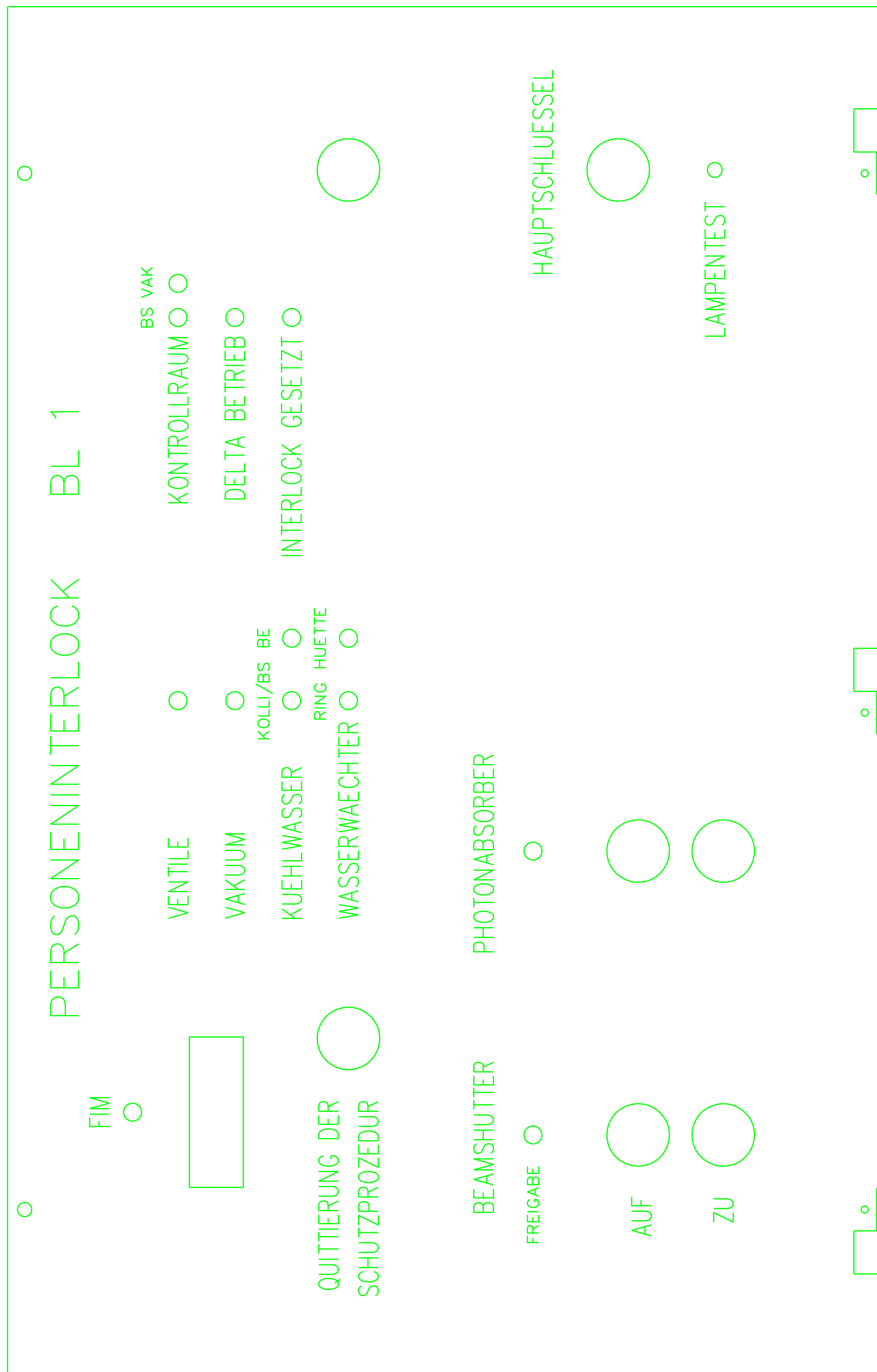

Fig. 4.15.: Scheme of the front panel of the safety interlock control system.

As the search is a very important task, the searching procedure has to be performed in an exactly defined step order:

- Close the experimental hutch door. Otherwise the searching procedure cannot be started.
- Press the orange, blinking search button at the interlock front panel. Afterwards it is illuminated continuously.
- Open the hutch door and enter the hutch. Leave the door open.
- Search the hutch and press the two green, blinking buttons next to the emergency stops. Afterwards they are illuminated continuously, advising the emergency stop activity.
- Exit the hutch through the door, thereby passing the light barrier.
- Close the door within 20 seconds after the second search button has been pressed. The orange confirmation button at the front panel of the interlock control system starts to blink.
- Press the confirmation button within 25 seconds after the door has been closed.

If everything has been performed in the correct order, the interlock is set, displayed by a green LED next to the label INTERLOCK at the front panel and a warning lamp at the outside of the hutch. The hutch is safe now and it is for sure that nobody is inside the hutch. Considering further approvals, that are described at the end of this section, it is allowed to open the beamshutter so that radiation can enter the hutch.

The information concerning DELTA operation is provided by the DELTA control system. The LED in the upper right corner of the front panel is green in case of DELTA operation. Above this display the approvals for the valve V_0 and the beamshutter given by the DELTA control system are shown.

The LED for the valve system (top LED in the middle block) is green in case that the valves V_0, V_1, V_2, and the fast closing valve are open and that the valve VA_1 at the first extraction is closed. This information is provided by the valve control system. The information concerning the vacuum status is a combination of the DELTA vacuum approval and the OK signals attesting the vacuum quality inside the recipient. The latter information is provided by the cold cathode gauge heads in the sections M1 - M3 and the Pirani gauge head in front of the fast closing valve. In case of a water flow higher than 4 $\frac{\mathrm{l}}{\mathrm{min}}$ inside the cooling system the

LEDs displaying the cooling system status switch to green. There is one LED for each cooling circle. As long as the water monitoring systems do not recognize any leak in the cooling circuits, the corresponding LEDs are green.

The beamshutter and photon absorber are controlled by the buttons and displays in the lower left front panel section. Both components consist of a lamp signalizing the status of approval of a device opening and two buttons in order to open (green button) or close (red button) the component. In addition, the buttons act as position detectors for the beamshutter and the photon absorber. Different signals are necessary to open the beamshutter. The interlock must be activated, the OK signal of the main relay board is required as well as the approval of the DELTA control system regarding the beamshutter and the vacuum, the valve status and vacuum status have to be okay, and the cooling circuits must be operational. If all the mentioned information is provided, the beamshutter can be opened by pressing the green button. This initiates the catch system (section 4.3.3) and starts the warning announcement as well as the flashing lights inside and outside the hutch (figure 4.16). After 20 seconds the announcement and the flashing lights stop and the beamshutter starts to open.

The warning panel restricted area above the hutch door at the outside of the hutch is now illuminated. In addition, two warning lamps labeled beamshutter are illuminated. The first lamp is located inside the hutch next to the flashing light and the second lamp is installed above the door of the experimental room. Therefore, the beamshutter status can be seen from positions at the working place and the control rack. If the beamshutter does not reach the open position within 15 seconds it is closed again automatically. In order to open the photon absorber the vacuum and valve status have to be okay and the cooling system must be functional. In this case the photon absorber can be moved immediately. The release buzzer of the hutch door is inactive in case of a non-closed beamshutter and simultaneous DELTA operation. This ensures that an entering of the hutch is not possible in an insecure situation.

For the case of an emergency there are four emergency stops at BL 1. The first one is located at the interlock control front panel and a second one is located next to the light switches of the experimental hutch. There are two emergency stops inside the hutch to guarantee that an emergency stop can be reached from every position inside the hutch without crossing the x-ray beam. The consequences due to an emergency are described in section 4.3.3.

Fig. 4.16.: Warning panels inside and outside the experimental hutch. There is a flashing light and a beamshutter warning panel inside the hutch. The panel restricted area and interlock are installed at the outside of the hutch as well as another flashing light.

4.3.1.1. The main relay board

The main relay board is a standard device at DELTA beamlines and consists of 20 relays (figure 4.14 top insert). It controls the main important signals for a safe beamline operation. It ensures a properly closed hutch door, an active interlock and the operational reliability of all emergency stops at the beamline. The first six relays are connected to the signals of the following components:

- status interlock OK delivered by the interlock control system,
- emergency stop at the front panel of the interlock control system,

- gate contact of the doors of the experimental hutch,
- emergency stop outside the hutch,
- emergency stops inside the hutch,
- light barrier at the entrance of the experimental hutch.

These components are important for the safety system. The remaining relays are bridged as they are not required at BL 1. In case of an OK signal of a device, the corresponding relay switches in a connected mode. This status is displayed by a green LED in the front panel of the main relay board. If all relays are switched, a 24 V signal is delivered as an output signal signifying the OK status of all safety relevant components. This signal is used by the safety interlock system for the beamshutter approval and it is used for the catch system (section 4.3.3).

4.3.2. The valve control

The valve control system consists of a separate PLC (Siemens Simatic S7-300 CPU 313C). It manages the signals concerning the vacuum and controls the triggering of the valves V_0, V_1 and V_2. The function standby of the different components is visualized by red/green LEDs below the corresponding label (figure 4.14 lower front panel and figure 4.17).

Each vacuum section consists of a HV and UHV gauge head. They are labeled as M1 - M3. The display of M0 is of particular importance as it is the approval to open V_0 given by the DELTA control system. In case of a bad storage ring vacuum, an opening of V_0 is not possible in order to protect the beamline vacuum. The fast closing valve must be open for the opening of V_0. This status is displayed by the LED SSV ok (SSV: German abbr. for fast closing system).

A valve opening is only approved if the pressure in front of and behind the valve is at least in the HV region. This information is provided by the cold cathode gauge heads and the corresponding thresholds. The trigger for opening and closing the valves is given by a lever switch. Each valve can be operated separately. The LEDs above the switches display the open or closed status of the corresponding valve. For V_0, V_1 and V_2 the LED is green in case the valves are open.

The lights for the valves at the recipient extractions behave differently. As beamline operation is only possible, if these valves are closed, the LED is green for the closed status. As the valves at the extractions are valves between UHV and atmosphere pressure, a remote

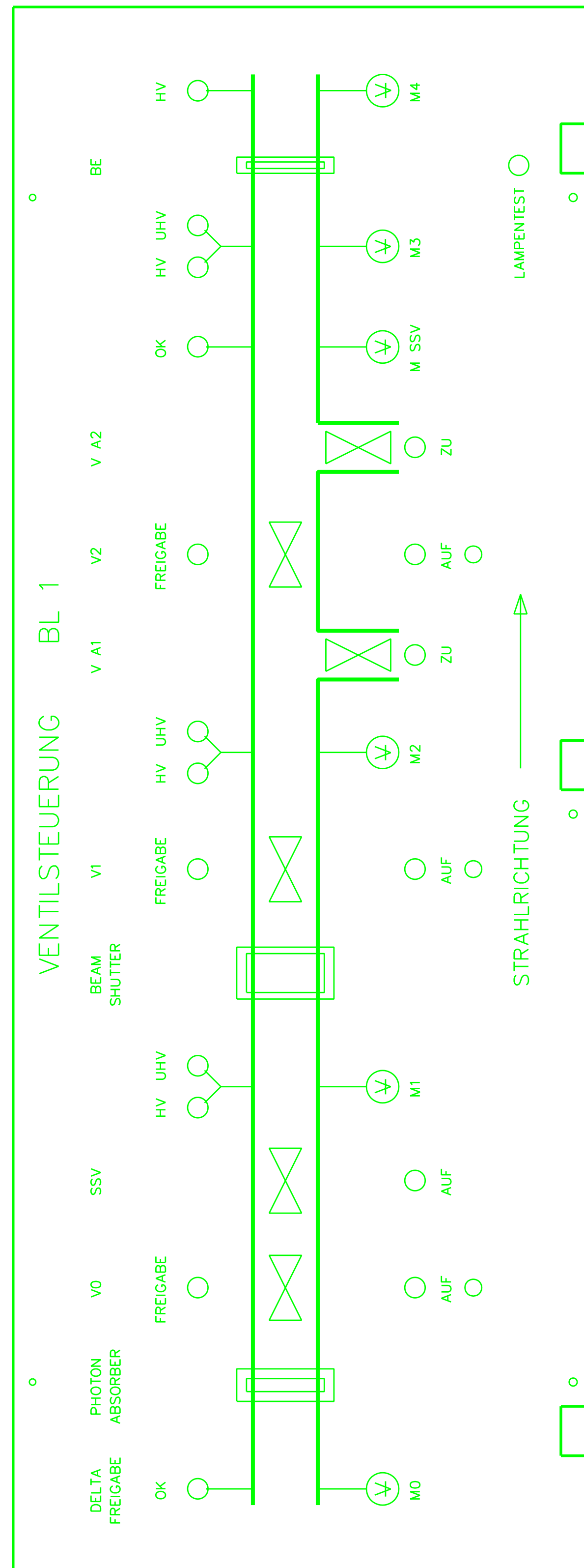

Fig. 4.17.: Scheme of the front panel of the valve control system.

opening must be avoided. For this reason there is no switch available at the front plate for these two valves. In addition solely the status information of the valve positions is connected to the vacuum PLC.

The fast closing valve position and the status of the corresponding pressure gauge head M SSV are displayed by LEDs at the front panel of the valve control system. M4 is an additional HV sensor at the experimental end station, which signalizes that the pressure is at a satisfying condition for exposure.

4.3.3. The catch system

The catch system is one of the most important systems to guarantee a safe beamline operation. It is responsible for a beam dump and the beamshutter closing in case of an interlock break during the performance of an experiment, or in case of pressing an emergency button during beamline operation. The catch system is realized by relay 13 in the relay box (section 4.3.4). The schematic connection diagram is shown in figure 4.18.

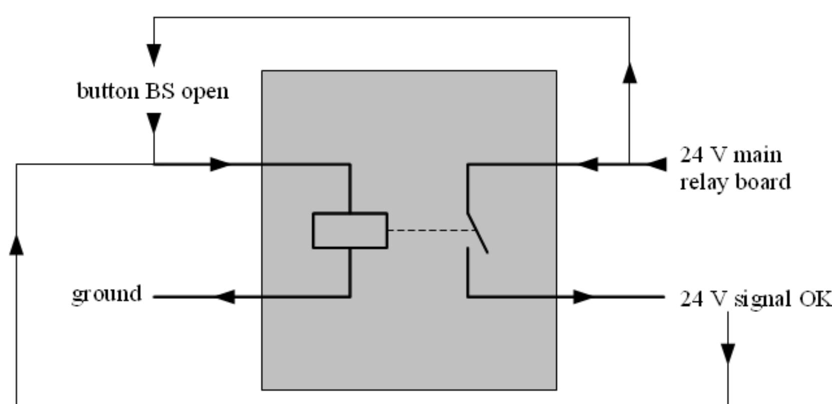

Fig. 4.18.: Schematic drawing of the catch system.

When the main relay board sends the OK signal as a 24 V output, this voltage is transferred to the catch system. The signal is connected to the input of the switching contact as well as to the opening button for the beamshutter (BS open). By pressing the button BS open for a short time, the 24 V of the main relay board are put on the actuation contact input. As a result the relay switches and the 24 V at the switching contact are interconnected. This signal is applied to the actuation contact input and makes sure that the relay is switched as long as there is the 24 V signal from the main relay board.

The interconnected 24 V signal is sent to the control room of DELTA via a separate relay (section 4.3.4). In case of a system failure or an emergency, e.g. the opening of the hutch

door during an exposure, the pressing of an emergency button, or the break of the light barrier, the corresponding relay in the main relay board immediately cuts out the 24 V signal. Therefore, the approval for the interlock and the beamshutter opening is lost and the following consequences are initiated: As the catch system signal is lost in the DELTA control room, the beam is dumped as a first safety measure in case of a non-closed beamshutter. Furthermore, the PLC of BL 1 ensures a closing of the beamshutter. After the catch system interrupt it is not possible to immediately activate the catch system again. Instead, the interlock has to be set again including the searching procedure.

4.3.4. The communication between BL 1 and DELTA control system

Several signals are exchanged between BL 1 and the DELTA control system. All this information is transmitted via relays in order to decouple the DELTA PLC and the BL 1 PLC. The relays ensure a galvanic separation of both control systems. The communication is realized by a separate relay box installed in the beamline control rack (figure 4.19).

The first relay delivers the information on the injection status from the DELTA control system to the PLC of BL 1. Relay 2 signalizes if there is beam operation at DELTA or not. The operation approval for BL 1 given by the DELTA control system is transferred by relays 3 and 4. Here, relay 4 disconnects the beamshutter control from the BL 1 control system, enabling

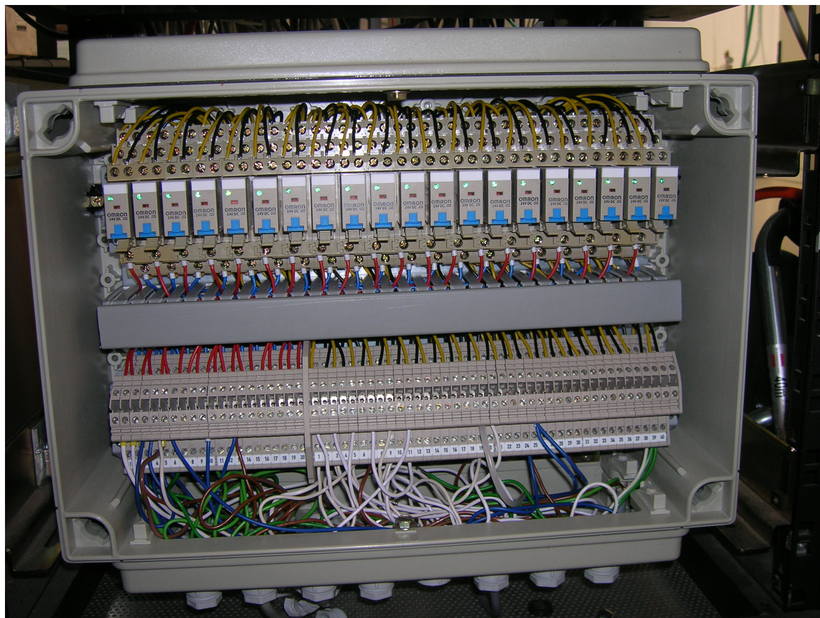

Fig. 4.19.: The relay box installed at BL 1 ensures a galvanic separation of the signals exchanged between BL 1 and the DELTA control system.

a beamshutter closing by the DELTA control system independently from the BL 1 control. This construction is necessary to ensure a closing of the beamshutter in case of the loss of the beamshutter approval. A 24 V signal coming from the DELTA control system and processed by relay 5, enables the status request regarding beamshutter and photon absorber. Relay 13 is used for the catch system (section 4.3.3). In case the catch system is active, the signal is sent to the DELTA PLC via relay 10.

5. Beamline Commissioning

After completion of the beamline setup, different test procedures were performed by the DELTA radiation protection division in order to check the fulfillment of the safety requirements. The performed tests are presented in the first section of this chapter.

Afterwards the beam was characterized with respect to its position in the beamline, its horizontal homogeneity and its vertical profile. In addition, the photon flux at BL 1 was calculated. The measurements and results are described in section 5.2.

5.1. Fulfillment of safety requirements

The safety interlock of BL 1 was checked using the searching procedure described in section 4.3.1. As the correct sequence of the searching steps is crucial to a safe beamline operation, it was checked that solely the default sequence leads to a successful interlock activation. In addition, the communication between BL 1 and the DELTA control system was inspected by simulating beamline operation (operation approval at a beam current of 0 mA). All tests have been completed successfully at BL 1.

In a next step DELTA operation was performed under realistic conditions in order to accomplish radiation protection measurements. At this time the beamshutter and photon absorber at BL 1 opened for the first time. Hence, synchrotron radiation could pass the whole beamline and enter the experimental hutch.

The electron beam current of DELTA was increased stepwise. At each step the photon absorber and beamshutter were opened for approximately 1 - 2 minutes and radiation protection measurements were performed. The first step was at 30 mA, followed by 50 mA, 70 mA, 90 mA and finally 120 mA. The pressure in the first vacuum section (gauge M1) degraded from 10^{-8} to 10^{-6} mbar during the measurement period due to contaminations, which in particular remained at the collimator and the beryllium window despite bake-out.

These contaminations were released by the striking photon beam. With opened beamshutter and photon absorber the pressure stabilized at 10^{-6} mbar within one minute and improved as soon as the photon absorber and beamshutter were closed. No radiation was detected around the beamline and outside the experimental hutch during the measurements. Hence, the permission to perform first beam characterization measurements was given.

5.2. Beam characterization

Different beam characterization measurements were performed at BL 1. The beam position at the end station was checked using photosensitive paper (section 5.2.1) and the beam profile was investigated by use of a pin-diode. The beam homogeneity across the beam cross section as well as the vertical beam profile were determined (section 5.2.2). Finally, the photon flux at BL 1 was calculated (section 5.2.3).

5.2.1. Beam position investigation

The beam position at the end station was characterized by fixing a piece of photosensitive paper in the beam path at the adapter between beamline and end station (figure 5.1). The labels "ol" and "or" mark the upper left and upper right corners, respectively. The terms "left" and "right" are with respect to a viewing direction from the end station to the storage ring. The rectangular beryllium window aperture is visible in the background of the beamline interior view.

The paper was exposed at 82 mA for 20 seconds and removed from the adapter afterwards to take photographs. The exposed region was measured to determine the beam dimensions.

The characteristics of the beam intensity over the width of the beryllium window is shown in figure 5.2. The higher the photon flux, the deeper is the blackening of the photosensitive paper. The maximum intensity is visible at the lower edge of the beryllium window aperture by the dark gray bar (marked by the red arrow). The position of the maximum implies a non-complete illumination of the Be window aperture. In order to gain a homogenous illumination of the beryllium window, the beamline height was lowered by 3 mm in the last beamline section starting at valve V_2 and ending at the end station.

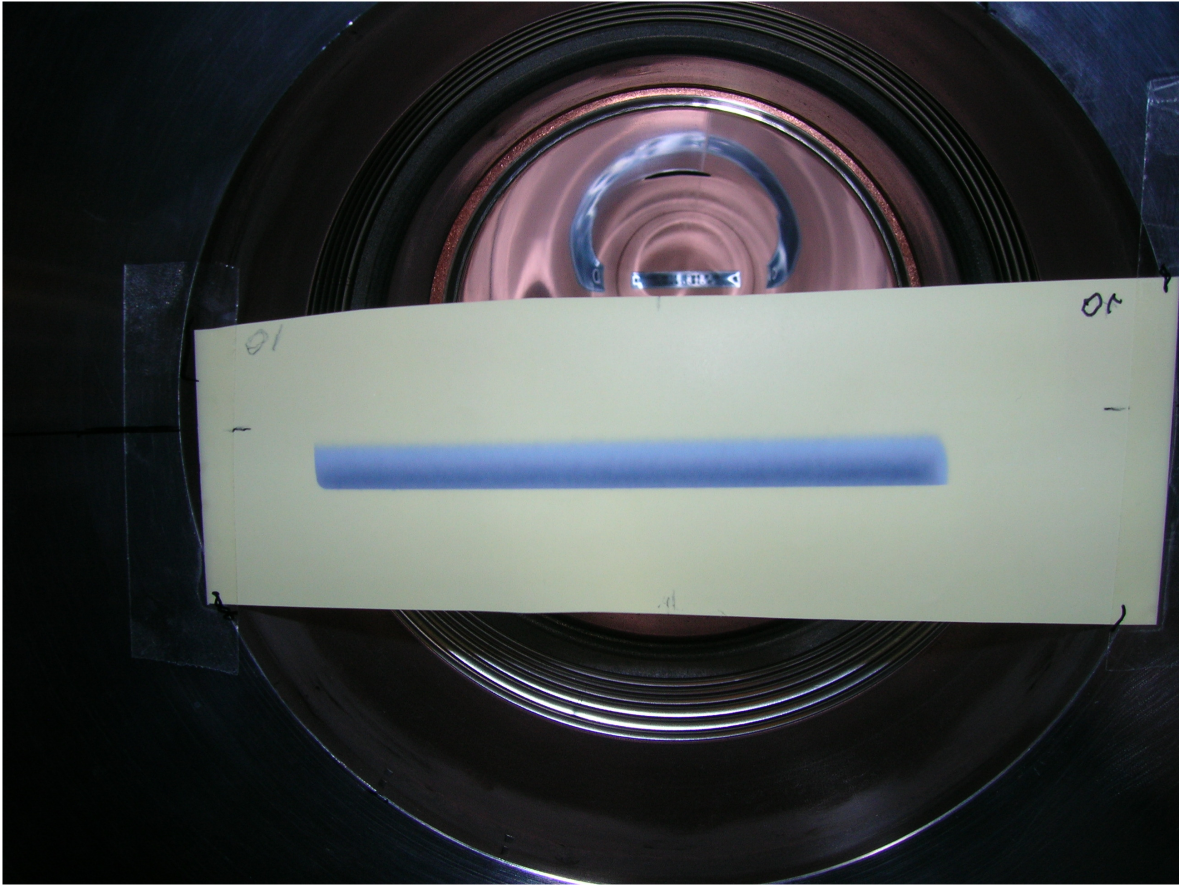

Fig. 5.1.: Photosensitive paper is fixed in the beam path at the adapter piece from beamline to end station. The rectangular beryllium window aperture is visible in the background. The labels "ol" and "or" mark the positions upper left and upper right corner with respect to a view from the end station to the storage ring.

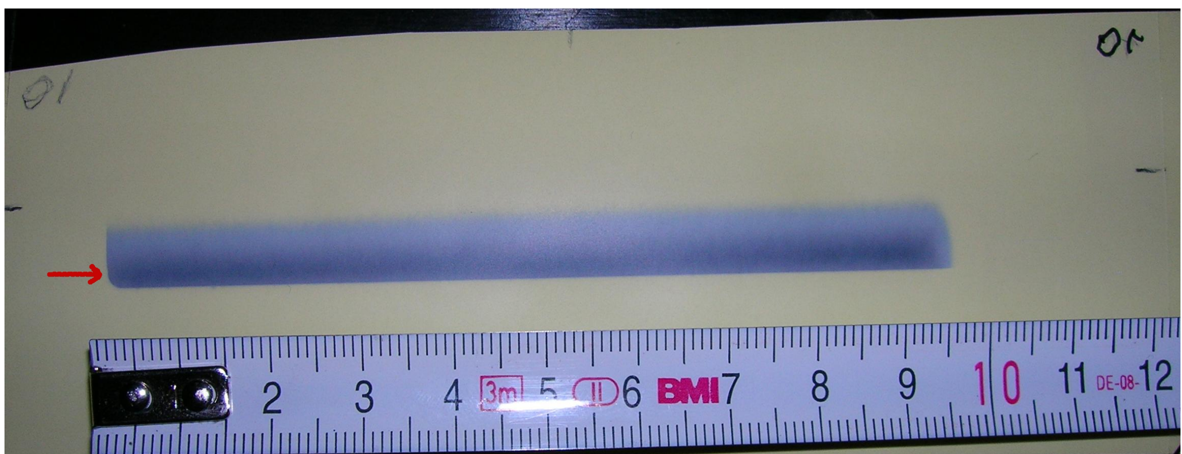

Fig. 5.2.: The first exposed photosensitive paper shows the cross section of the photon beam. The beam maximum does not fit completely in the beryllium window aperture.

Finally, another piece of photosensitive paper was exposed for 30 seconds at a beam current of 60 mA. After the lowering, the beam maximum is positioned slightly below (approximately 1 mm) the vertical window center. However, the beam maximum fits completely in the window aperture, assuring a homogeneous illumination of the window and the end station (figure 5.3).

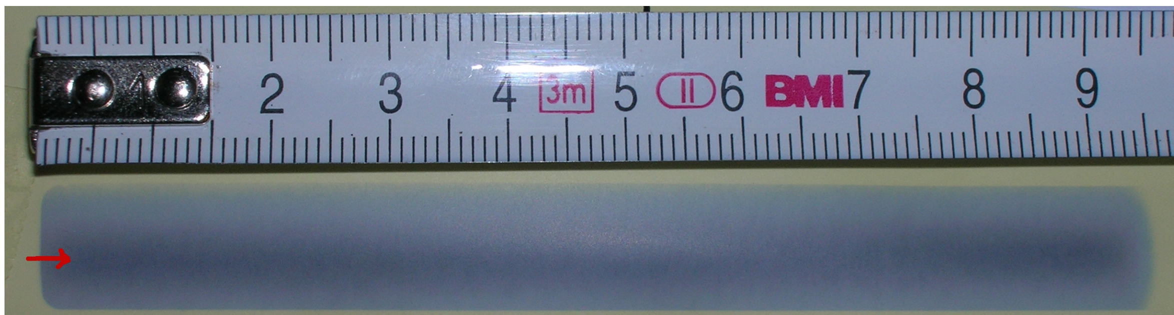

(a) Beam width

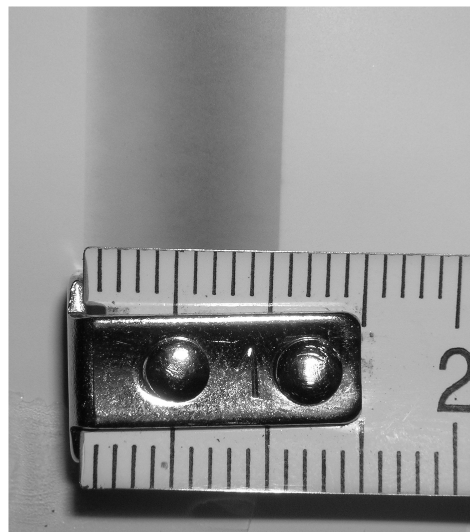

(b) Beam height

Fig. 5.3.: Beam position after the lowering of BL 1. The maximum is now centered in the beryllium window aperture. (a) The beam width is 97 mm. (b) The beam height is 10 mm in accordance with the Be window height.

The beam height is 10 mm in accordance with the aperture height and the full beam width is 97 mm. Due to the beamline setup the theoretical beam width at the measuring position is about 110 mm. Taking the horizontal beamline center into account, the beam width is approximately 53 mm to the left and 44 mm to the right to the center. Hence, the beam width is 13 mm less as intended on the right window side.

A detailed inspection of the left and right beam edges reveals a sharp beam truncation at the left side by the window aperture and a less defined edge at the right side, indicating that the beam does not illuminate the complete window width. This effect requires further investigations considering the following aspects:

- complete illumination of the outlet chamber,
- collimator alignment with respect to the radiation source point,
- beryllium window alignment regarding the collimator position.

Although the beam does not reach its full width at the experiment, exposures of 4 inch wafers are feasible. As these wafers are exposed in a centered area of approximately 80 mm diameter, the beam at BL 1 is wide enough to guarantee a complete and uniform exposure.

5.2.2. Beam profile investigation

After the measurements using photosensitive paper the beam profile was characterized in detail using a pin-diode consisting of a 500 μm thick silicon layer. The diode signal was amplified and transmitted to an oscilloscope, where it was visualized and stored.

The diode was attached to a horizontally moving stepper motor which was mounted to an adapter plate at the front of the wafer stepper (figure 5.4). As the measurements were performed in air at ambient pressure and an estimated temperature of about 300 K, the beam path in air was minimized to reduce scattering. Therefore, the recipient behind the beryllium window was flooded with helium under ambient pressure and sealed with a Kapton window of approximately 230 μm thickness. This was necessary, as an evacuated recipient in combination with the power of a white beam is a risk for the beryllium window in case of a possibly cracking Kapton window as the latter one could not be cooled. The diode was positioned at about 30 mm behind the Kapton window.

Two different kinds of measurements were performed using the pin-diode. The beam homogeneity was measured in horizontal direction and afterwards the vertical profile was determined at different positions in the beam. As the pin-diode has a photosensitive circular area with a diameter of about 20 mm, the area was covered with a sheet of 25 μm thick black Kapton to eliminate all signals but the synchrotron radiation.

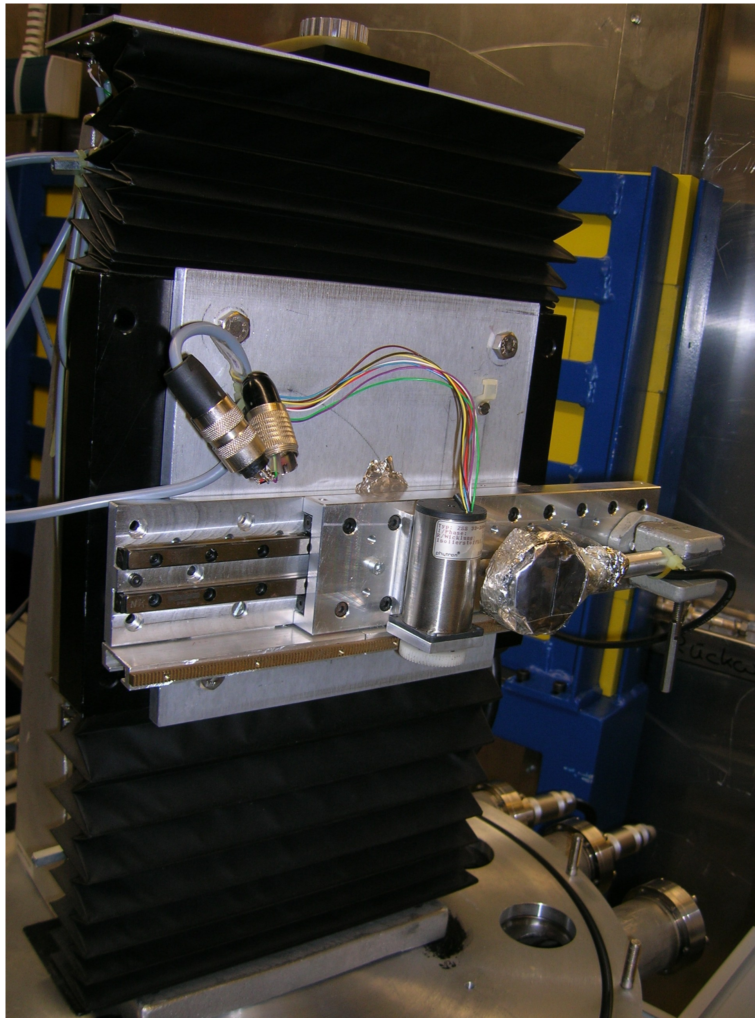

Fig. 5.4.: The pin-diode is fixed to a stepper motor which can move in horizontal direction. The motor is mounted to an adapter plate fixed at the wafer stepper.

Horizontal beam profile

To measure the horizontal homogeneity of the vertically integrated photon flux the pin-diode was covered with lead tape such that a small vertical gap of about 1 mm remained, serving as an aperture slit.

For the characterization of the horizontal beam profile the pin-diode was moved several times along the beam cross section and a data set was stored by the scope for each scan. For these measurements the amplifier was regulated to an amplification factor of 10^3. The electron beam current at DELTA was approximately 80 mA. Data was taken for five runs, i.e. three times in forward and two times in backward direction. “Forward” in this context means from the right to the left side with respect to a view in the direction of the storage ring.

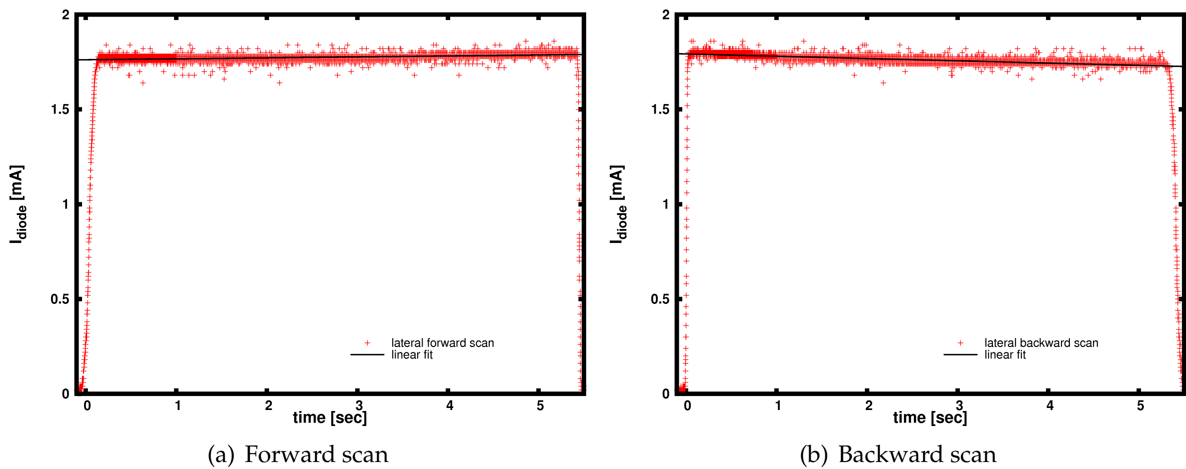

(a) Forward scan

(b) Backward scan

Fig. 5.5.: Horizontal scan of the beam cross section at BL 1. (a) Scan from the right side to the left side. The slope is positive indicating a photon flux increase in this direction. (b) Scan from the left side to the right side. The slope is negative due to the reverse moving direction.

An example of the current measured by the pin-diode (I_{diode}) in dependence of the motor run time is shown in figure 5.5. The signal significantly increases from zero to approximately 1.8 mA and afterwards it remains on a plateau. On the right side of the diagram the signal steeply decreases to zero again. The curve progression is explained by knowledge of the motor end positions, that are located at the right and the left edge of the beam. As there is a small distance between the end positions and the beam edges, the signal at the start and the end of the motor run is zero. By passing the beam in horizontal direction, the vertically integrated photon flux of the beam is measured, yielding an almost constant value of about 1.8 mA.

The profiles corresponding to one direction yield same results. The investigation of the curves shows that the plateau is not constant. The profiles measured in forward direction have a positive slope, which indicates a higher photon flux at the left beam side. For the backward scans there is a negative slope confirming the results of the forward scans. The linear part was fitted by a straight line. For all measurements the range from 0.3 to 5 seconds was chosen for the fit as the curve is linear in this range for all data sets. The slopes were determined with an uncertainty of 0.8% - 2.4% due to the fit. The signal deviation from one side to the other side of the beam was calculated using the formula obtained from the linear regression. For the five data sets the deviations are in the range of 1.5% and 4%. Therefore, the deviation of the measured horizontal beam homogeneity with respect to a constant horizontal

photon flux is very small. Reasons for this deviation are mentioned after the discussion of the results obtained from vertical beam profile measurements.

Valuating the horizontal beam profile on basis of the performed measurements and the results obtained by the observation of the photosensitive paper, an almost homogeneous illumination of the beryllium window can be assumed. The maximum of the photon flux is almost located in the vertical center of the beryllium window aperture and the horizontal photon flux distribution is nearly constant.

Vertical beam profile

The vertical beam profile was investigated using a similar experimental setup used for the horizontal beam characterization. As the aperture slit was exchanged with a pinhole, the black Kapton foil in front of the diode was covered with lead tape that was drilled by a small needle generating a circular hole with a diameter of 0.5 mm. The amplifier was regulated to an amplification factor of 10^4. The horizontal stepper motor was used in combination with the wafer stepper servo motor that performed a vertical movement.

Data was taken by moving the pin-diode in horizontal direction. The diode stopped at discrete positions and performed a vertical movement across the beam. The distance between the discrete stops was 50 motor steps, i.e. 11.8 mm. Eight vertical scans were performed along the beam width, each time from bottom to top. The servo motor needed 11 seconds to cover the vertical distance of 186 mm from the lower motor end position to the top end position.

An example vertical beam profile of the beam at BL 1 (figure 5.6) shows the measured diode current I_{diode} as a function of time. The time parameter is given by the time that the motor needed to cover the beam height.

All measured vertical profiles show a gaussian profile as it is expected for synchrotron radiation [28]. Therefore, the data (red crosses in figure 5.6) was fitted with a gaussian distribution (black curve) to determine the amplitude and the full width at half maximum (FWHM). These parameters provide information concerning the maximum photon flux and the FWHM of the beam in vertical direction. As the pinhole was very small compared to the vertical beam profile the aperture was neglected for profile analysis. The values determined for the amplitude and the FWHM are presented in table 5.1.

The FWHM values are almost constant, indicating a uniform beam height along the entire beam width. The average of 0.227 seconds corresponds to a beam half-width of 3.84 mm. The maximum deviation from the mean is 0.4%.

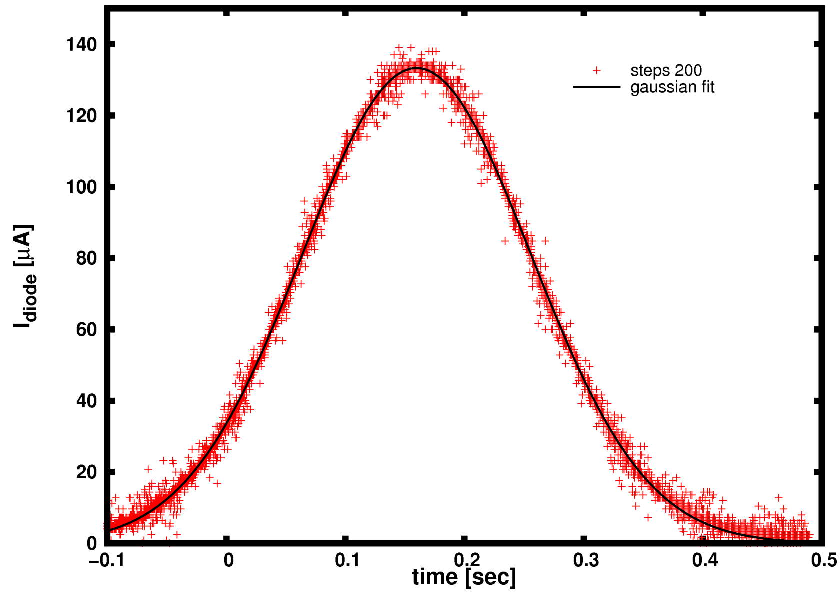

Fig. 5.6.: Vertical profile across the beam cross section. The profile 200 steps from the right end position of the stepper motor is shown. Its shape is conform with a gaussian. The black line indicates the gaussian fit for the shown profile.

Tab. 5.1.: Values of the amplitude and FWHM determined from the vertical beam profiles fitted with a gaussian.

position [steps]	50	100	150	200	250	300	350	400
amplitude [μA]	131.9	132.7	133.1	133.3	136.9	133.5	133.1	132.9
FWHM [sec]	0.228	0.227	0.227	0.227	0.228	0.227	0.227	0.226

The determined amplitudes as a function of the measuring position are depicted in figure 5.7 revealing an almost homogeneous maximum intensity along the beam width. Therefore, the intensity increase observed at the horizontal beam characterization is a systematic effect.

By non-observance of the high value at 250 steps, the averaged amplitude is 132.9 μA, yielding a maximum value deviation to the mean of 0.8%. The error bars result from fitting uncertainties.

The calculation of the maximum photon flux at BL 1, determined from the amplitude is described in section 5.2.3.

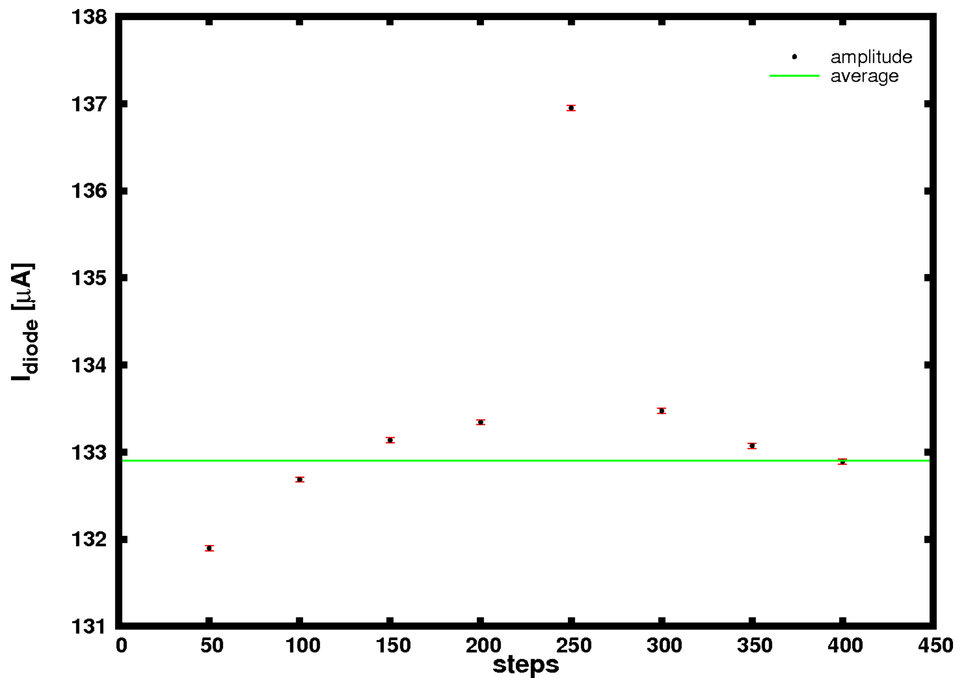

Fig. 5.7.: Measured amplitudes of the gaussian profile as a function of the position along the beam. Compared to the average amplitude (green line) the maximum deviation is about 0.8%. The maximum photon flux is homogeneous along the beam width.

In conclusion, the beam at BL 1 offers the following properties:

- The maximum of the photon flux distribution is vertically centered in the beryllium window.
- The vertically integrated photon flux along the beam width can be considered as homogeneous.
- The vertical beam profile complies with a gaussian distribution.
- The maximum photon flux is constant across the beam width.
- The FWHM is constant across the beam width.

Thus, the beam shows a very uniform profile along the beam width with a homogeneous photon flux distribution. These are the key properties to perform deep x-ray lithography.

5.2.3. Photon flux calculation

The theoretical photon flux as a function of photon energy can be calculated in consideration of the electron energy of the storage ring, the electron beam current, the magnetic field of the bending magnet, and the absorbing materials along the beam path .

The signal of the pin-diode at a discrete photon energy E and a given photon flux can be calculated from the following equation [54]

$$\frac{\varphi}{I} = \frac{\varepsilon}{e\,E\left[1-\exp\left(-A_{\mathrm{pe}}\,t_{\mathrm{Si}}\,\rho_{\mathrm{Si}}\right)\right]}. \tag{5.1}$$

φ[photons/sec] denotes the incident photon flux and I[A] is the corresponding diode current. Photons of energy E[eV] generate electron-hole pairs, where ε is the required energy of 3.66 eV [54]. e is the elementary charge of an electron. To calculate the pin-diode efficiency, the photo-electric cross section of silicon (A_{pe}) as well as the thickness of the silicon layer ($t_{\mathrm{Si}} = 500\mu\mathrm{m}$) and its density ($\rho_{\mathrm{Si}} = 2.33\frac{\mathrm{g}}{\mathrm{cm}^3}$) are required.

As the photo-electric cross section depends on the energy of the incident photons, and as a white spectrum is investigated at BL 1, A_{pe} has to be calculated for each photon energy. The energy dependence can be described by a third order polynomial as shown in equation 5.2 [54]

$$\log_{10}(A_{\mathrm{pe}}) = 4.158 - 2.238\log_{10}E - 0.477(\log_{10}E)^2 + 0.0789(\log_{10}E)^3\,. \tag{5.2}$$

In addition, the following absorbing materials have to be considered at BL 1 due to the experimental setup:

- 127 μm beryllium of the Be window,
- 920 mm helium under ambient pressure and a temperature of about 300 K,
- approximately 230 μm Kapton,
- approximately 30 mm air under ambient pressure and a temperature of about 300 K,
- 25 μm Kapton.

To calculate the photon flux at BL 1 the following steps have to be performed: First the theoretical energy dependent photon flux distribution of a bending magnet is calculated. The influence of absorbing materials is considered by multiplying the photon flux at each energy with the energy dependent transmission of the corresponding material. In a next step

the theoretically generated diode current is calculated for each photon energy. Afterwards the current is integrated over the full photon energy spectrum of the bending magnet. In addition, the photon flux distribution is integrated over the full spectrum in order to obtain the entire photon flux.

The theoretical diode current is compared to the experimentally measured current and the obtained ratio of the currents is translated to the theoretical photon flux. Considering the ratio and the theoretical flux, the effective photon flux at BL 1 is determined.

The theoretical diode current was calculated to be 214.9 μA considering a theoretical photon flux of $4.28 \cdot 10^{10}\ \frac{\text{photons}}{\text{s}\,\text{mm}^2\,\text{mA}}$. The flux was normalized to 1 mA electron beam current and 1 mm^2 of incident area on the pin-diode. As the average measured amplitude of the vertical beam profiles is 132.9 μA, the incident photon flux is determined to be $2.64 \cdot 10^{10}\ \frac{\text{photons}}{\text{s}\,\text{mm}^2\,\text{mA}}$. As the measurements were performed at an electron beam current of about 85 mA the flux was normalized to 1 mA. In addition, the pinhole aperture of the pin-diode with its diameter of about 0.5 mm was considered. The result is given by the number of photons per second, per mA electron beam current, and with respect to 1 mm^2 of incident area. The ratio between experimental and theoretical flux is 0.62. Therefore, the experimentally determined photon flux is less than the theoretically expected photon flux. Several explanations of this deviation can be assumed:

- Uncertainties in the absorption coefficient determination as the temperature of the helium and the air were not investigated during the measurement.
- The thickness of the Kapton foil for the Kapton window was measured with a slide gauge and contains a measuring uncertainty.
- The distance between Kapton window and pin-diode was estimated due to a missing high precision setup.

Despite the possible uncertainties the results demonstrate, that the photon flux at BL 1 corresponds to the order of magnitude of the theoretically expected photon flux.

6. Sample Preparation

The silicon wafers for the test exposures at ISASLine BL 2 and for the exposures at the new x-ray lithography beamline BL 1 were produced by an external company (MRT micro resist technology, Berlin). In order to investigate the photoresist surface x-ray reflectivity experiments were performed. Thus, some wafers were cleaned by the preparation laboratory at the physics department of the TU Dortmund and spin coated in cooperation with the micro technology working group of the ET&IT department (electrical engineering and information technology). The prepared wafers were Si (111) wafers with a diameter of 4 inch (101.6 mm).

6.1. Chemical cleaning of Si (111) wafers

In order to gain a good resist adhesion to the wafer, the wafer had to be cleaned. The cleaning was performed using solvents or diluted acid, followed by a rinse with deionized water [55]. For a thorough wafer cleaning a Piranha etch and/or a RCA cleaning is suggested [56]. As Piranha etch is quite dangerous in handling, this method was replaced by Shiraki cleaning.

6.1.1. Shiraki cleaning

The single process steps of Shiraki cleaning are itemized for a better overview [57].
Degreasing:

- The silicon wafer is cleaned for 10 minutes in an ultrasonic bath with distilled water.
- It is rinsed two times in an ultrasonic bath with methyl alcohol (each time five minutes).
- An ultrasonic bath with trichloroethane is performed for 15 minutes.
- The wafer is rinsed again in methyl alcohol in an ultrasonic bath (two times five minutes).

- The wafer is cleaned in distilled water which is changed ten times.

Boiling in HNO_3:

- The wafer is boiled in HNO_3 (nitric acid, concentration 65%) in order to etch the surface and to generate an oxide layer.
- It is dipped in HF (hydrofluoric acid, 2.5 - 5%) for 20-30 seconds in order to remove the oxide layer.
- It is cleaned in distilled water which is changed ten times.
- The wafer surface is checked for damage.
- This procedure is repeated at least two times.

Boiling in HCl:

- The wafer is boiled for ten minutes in a dilution of distilled water, HCl (hydrochloric acid, 35-40%), and H_2O_2 (hydrogen peroxide, 30%) (3:1:1) to generate an oxide layer. H_2O and HCl are heated to nearly the boiling point and H_2O_2 is added shortly before the wafer treatment.
- The wafer is cleaned in distilled water, which is changed ten times.

Heating:

- The wafer is rinsed in diluted HF.
- It is baked on a hotplate at 200°C under nitrogen atmosphere for five minutes in order to dehydrate the surface [55].

As Shiraki cleaning is very time consuming, the alternative RCA cleaning is mostly used.

6.1.2. RCA cleaning

The second option for an efficient wafer cleaning is RCA cleaning [56, 58]. It generates an oxide layer which subsequently can be removed in case a pure silicon surface is required. The cleaning dilution contains distilled water, NH_4OH (ammonium hydroxide, 27%), and H_2O_2 (hydrogen peroxide, 30%) with the ratio 5:1:1. The distilled water is mixed with NH_4OH and heated up to 70 ± 5°C. Afterwards it is removed from the hotplate and H_2O_2 is added.

After 1-2 minutes the solution starts to boil, indicating that it is ready for use. The wafer is exposed to the solution for 15 minutes. Subsequently, the oxide layer is removed in HF (1-5%). Afterwards, the wafer is removed from the HF bath and thoroughly rinsed in distilled water.

As a silicon oxide layer can reduce the resist adhesion, the last rinse in HF (Shiraki cleaning as well as RCA cleaning) is necessary to remove this layer. In order to completely remove the acid (HF) used for the last process step, the wafer must be rinsed properly in distilled water as acid residues can lead to an undevelopable resist film on the wafer [11].

6.2. Wafer spin coating

The wafers were coated with a SU-8 negative resist provided by MRT. A temperature of 19 - 22°C at a humidity of 38 - 45% is recommended for wafer treatment. It is suggested to use 1 ml resist per 1 inch of wafer diameter [55], i.e. 4 ml resist are required for 4 inch wafers. The company MicroChem Corp. provides the following information concerning the spin coating process [55] yielding a layer thickness of 250 μm.

- 1 ml resist per inch of substrate diameter is dispensed on the wafer.
- The velocity is ramped from 0 to 500 rpm (rounds per minute) with 100 $\frac{\text{rpm}}{\text{s}}$.
- This speed (500 rpm) is retained for 5 - 10 seconds.
- The velocity is ramped to the final spin speed of 1000 rpm with an acceleration of 300 $\frac{\text{rpm}}{\text{s}}$.
- This speed is retained for 30 seconds.

The spin coating is followed by a so-called soft-bake (section 2.1.3.2) to evaporate the solvent and to densify the resist layer. The soft bake can either be performed on hotplates or in a convection oven. With hotplates, the first bake is carried out at 65°C for 30 minutes, followed by 90 minutes at 95°C [55]. Each temperature is reached by ramping.

During the spin coating process the spin speeds and times were adapted to the resist behavior and the experience of the ET&IT department. The final protocol was thus defined as follows:

- 4 ml resist are dispensed on the wafer.
- The speed is ramped to 500 rpm with an acceleration of 200 $\frac{\text{rpm}}{\text{s}}$.
- This velocity is retained for 18 seconds.
- The speed is ramped to 1300 rpm with an acceleration of 300 $\frac{\text{rpm}}{\text{s}}$.
- This speed is retained for 40 seconds.

The bulge of resist generated at the wafer edge was removed by rinsing with acetone while the wafer was spinning at constant velocity. The acetone was applied in a fine jet using a small injection needle and the dissolved resist was centrifuged due to wafer rotation.

The first step of the subsequent soft-bake was performed on a hotplate. The plate was heated up to 65°C and the wafer was baked for ten minutes. Afterwards, the wafer was removed from the hotplate and transferred on a steel plate into a convection oven with a temperature of 95°C where it was kept for 90 minutes. For cooling down, the wafer remained on the hot steel plate and slowly cooled down to room temperature over night.

The final resist thickness was about 300 - 350 µm. Due to the bulge removal the wafer could be used for x-ray reflectivity studies, as there solely remained a flat resist layer on the wafer.

Until exposure the wafers were stored at a temperature of 19 - 22°C at a humidity of about 50% in boxes that are opaque to visible light and UV light [59]. To avoid a resist flowing, the wafers require a horizontal storage. As unexposed resist areas are sensitive to light each wafer treatment prior to chemical development has to be performed at amber light.

7. First Exposures and Photoresist Investigations

Prior to setting up the dedicated deep x-ray lithography beamline BL 1, test measurements were performed at ISASLine BL 2 in order to find out if DXRL is feasible at DELTA. After completing the BL 1 setup, three wafers were exposed at this new beamline to demonstrate its operational reliability. The x-ray masks and the wafer-mask mounting system are presented in the first section of this chapter. The exposure performance at BL 2 and BL 1 is described in sections 7.2 and 7.3, respectively. As the structure quality of the exposed resist structures were investigated, these results are discussed in the context of the exposure performance at the corresponding beamline. As the measurements using a graphite mask showed a significant sidewall roughness of the resist structures, this aspect is discussed separately in section 7.4. The last section provides results concerning the surface roughness of SU-8, determined by x-ray reflectivity measurements.

7.1. Sample holding and x-ray masks

Since two different mask types are used at BL 1, two different mounting systems are required for the wafer-mask system. One system is adapted to a round 4 inch graphite mask while the other one allows to use a rectangular high precision titanium mask.

The graphite mask, which is provided by the company Micromotion GmbH, consists of a 150 µm thick graphite membrane with a gold absorber on top with a thickness of approximately 25 - 30 µm (figure 7.1(c)). This mask is used for the production of micro gear wheels which are used e.g. for micro drives and micro positioning systems applied in medical engineering, sample stage adjustment, actuators, etc. [60]. The titanium masks have a membrane thickness of 2.4 µm and the gold layer on top has a thickness of 10 - 20 µm. Figure 7.1(a) shows a tension test body structure on the first titanium mask [61]. The second

titanium mask contains acceleration sensor structures for air bag systems or seismological investigations (figure 7.1(b)) [61–63].

(a) Titanium mask

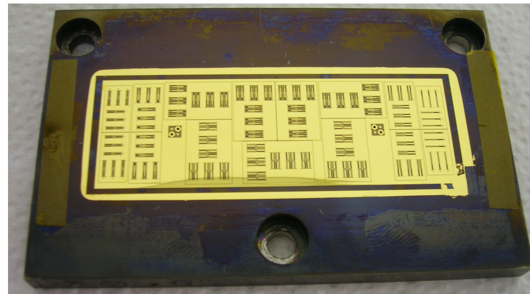

(b) Titanium mask

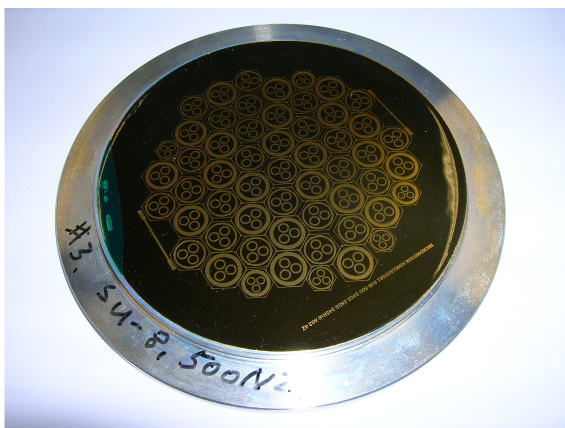

(c) Graphite mask

Fig. 7.1.: X-ray masks for exposures at DELTA. (a) Titanium mask for tension test bodies. (b) Titanium mask for acceleration sensors. (c) Graphite mask for micro gear wheels (from Micromotion GmbH).
For all masks, gold is the absorbing substance.

Both mask types are implemented in proximity exposure mode. When using the graphite mask, the mask is fixed in front of the coated wafer by placing both components in the groove of a u-shaped aluminum bar. The gap for the round graphite mask is about 8 mm high, while it is 25 µm for the titanium masks. This small gap is adjusted using a thin Kapton foil with the required thickness.

The mounting setup for the precision mask (figures 7.2 to 7.4) is attached to the wafer stepper carriage via the adapter plate at the bottom. Two all-thread rods (M6) which serve as a tool for the alignment of the wafer holding and the mask fitting are fixed in the plate. The wafer holding is made of a round aluminum plate with a 850 µm deep centered round recess (figure 7.3(a)). The recess diameter corresponds to the diameter of a 4 inch wafer plus a margin of 0.4 mm. The mask fitting is also made of aluminum and has the same outer diameter as the wafer holding (figure 7.3(b) and 7.3(c)). On the back, the fitting has a centered recess of 80 x 50 x 6 mm^3 for the mask. The aperture along the full fitting height is 75 x 35 mm^2.

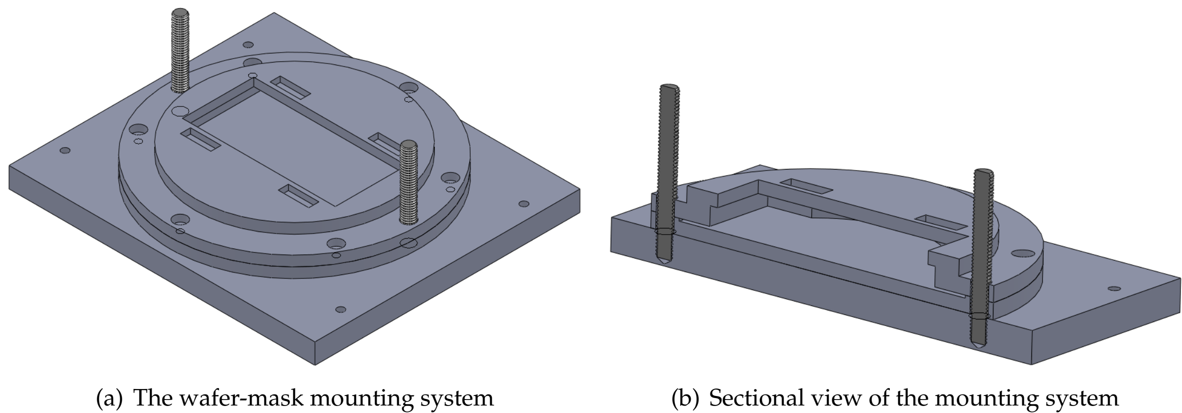

(a) The wafer-mask mounting system (b) Sectional view of the mounting system

Fig. 7.2.: The wafer-mask mounting system for rectangular masks. The adapter plate at the bottom enables the mounting of the system at the wafer stepper carriage. Four strong magnets are embedded in the cavities at the top side of the mask fitting to ensure a mask fixing.

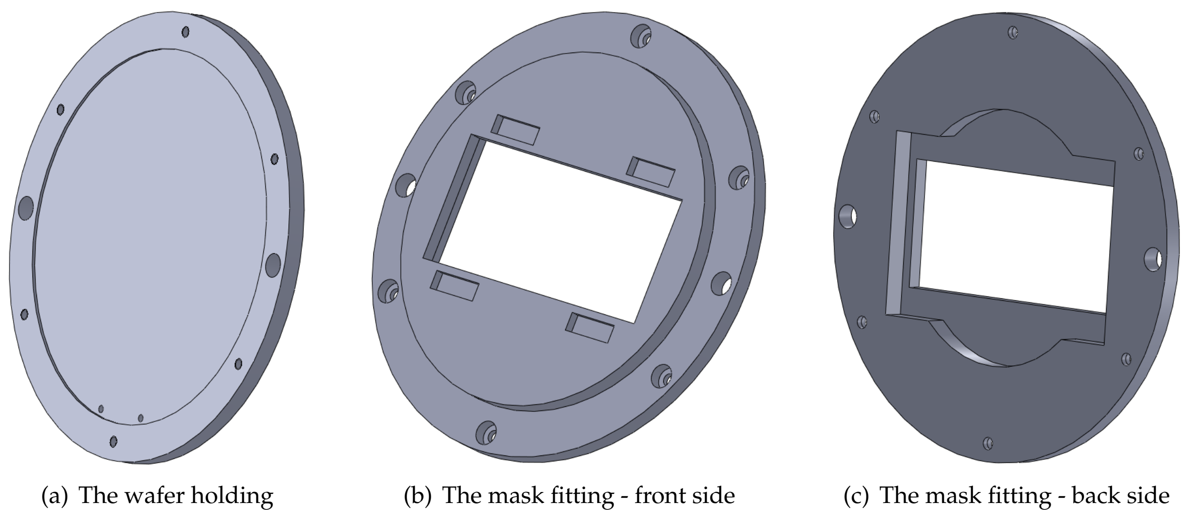

(a) The wafer holding (b) The mask fitting - front side (c) The mask fitting - back side

Fig. 7.3.: Wafer holding and mask fitting. The wafer holding has a recess of 850 μm. The mask is fixed at the back of the fitting and is hold by four magnets embedded at the front of the fitting.

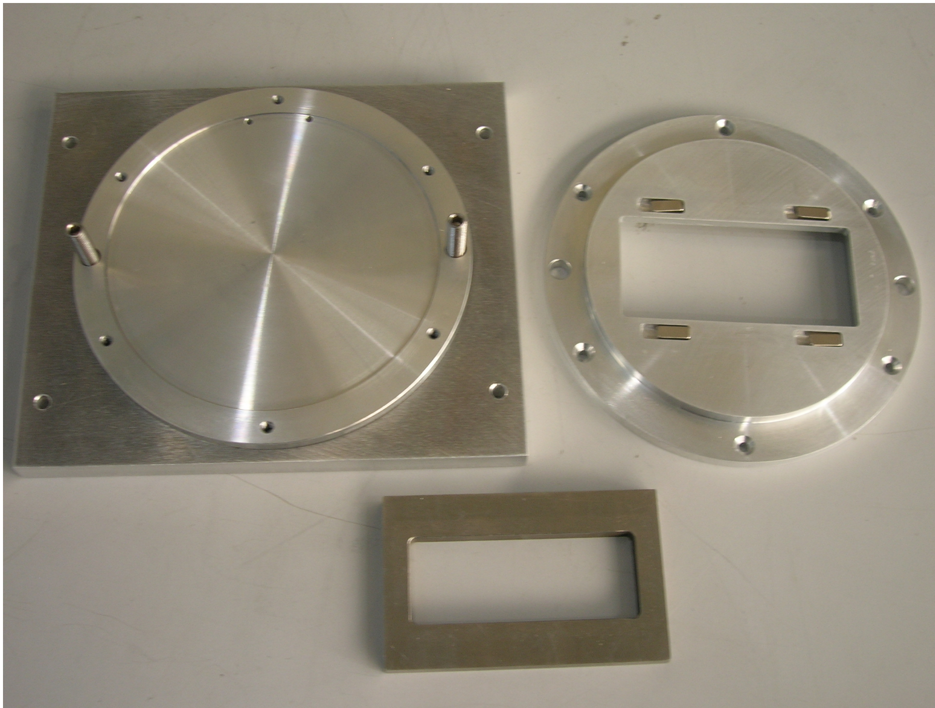

Fig. 7.4.: Photograph of the wafer mounting system for rectangular masks.
Left side: Adapter plate and the wafer holding. Right side: Mask fitting device with its four cavities and the embedded small magnets. The rectangular mask is applied in the recess at the back side. Front: Rectangular mask frame. Such frames are used by mask providers to stabilize the mask membrane.

In this region the radiation can pass the fitting, penetrating the mask from the back side. Four strong magnets with dimensions of 10 x 4 x 3 mm^3 are embedded in small cavities at the front side of the fitting to fix the mask.

7.2. Measurements at BL 2

The test exposures at BL 2 were done to check the feasibility of DELTA to perform DXRL. Thus, they were carried out at a similar setup used for BL 1. However, there was no beryllium window in the general setup of BL 2, which had therefore to be added for the test measurements. The exposure was performed in the exposure chamber presented in section 4.2.6. The wafers were covered with a SU-8 photoresist layer of approximately 550 μm thickness.

7.2.1. Exposure performance

Three test exposures were performed at BL 2 using the graphite mask presented in section 7.1. The pressure inside the exposure chamber was about 10^{-1} mbar for each measurement. Different exposure times were chosen to study possible differences in the structure quality due to different exposure doses.

The stepper had a full range of 186 mm and moved the wafer through the beam with a velocity of about 93 $\frac{mm}{s}$. The stepper acceleration phase at the start and the end of each movement was negligible as the moving range was much longer than the wafer diameter. Therefore, the velocity was constant at the time the wafer crossed the beam. As the beam had a height of 10 mm, the effective exposure time at one point of the resist was about $\frac{1}{19}$ of the total exposure time.

The applied doses were calculated using the software program DoseSim [64] and an additional program was used to calculate the total exposure time [18]. The parameters relevant for exposure, i.e. the electron beam current I_e at DELTA, the resist thickness d_{resist}, the exposure time t_{exp} as well as the top and bottom doses D_t and D_b, respectively, and the top to bottom dose ratio $(tbr = D_t/D_b)$ are listed in table 7.1.

After exposure the wafers were removed from the exposure chamber and baked on a hotplate at 55°C for 20 minutes. Subsequently, the temperature was increased to 75°C within

Tab. 7.1.: Parameters for the test exposures at BL 2.

	d_{resist}[μm]	I_e[mA]	t_{exp}[min]	D_t $\left[\frac{J}{cm^3}\right]$	D_b $\left[\frac{J}{cm^3}\right]$	tbr
wafer 1	548	90	5	85	16	5.3
wafer 2	559	105	10	195	36	5.4
wafer 3	558	75	15	195	36	5.4

5 minutes. The wafer remained at this temperature for 40 minutes. Afterwards, the hotplate was switched off and the wafer cooled down. After cooling down, the wafers were properly packed to avoid exposure to light and were sent to the external company MRT for chemical development. Investigations of the structure quality were performed by MRT as well as by the physics department of the TU Dortmund (chair of experimental solid state physics E1a). The results are presented in section 7.2.2.

7.2.2. Investigation of exposed wafers

A photo of an exposed wafer after the post exposure bake (PEB) is shown in figure 7.5, demonstrating the structuring of the resist layer.

Microscopy investigations performed after the chemical development revealed good results. The structures of wafer 1 were accurately developed and no residue remained in the corners (figure 7.6(a)). The structures of wafers 2 and 3 showed residues of photoresist in the gear teeth despite good developed structures in general (figure 7.6(b), residues are highlighted by red circles). It is supposed that this effect is caused by the higher applied dose [11].

Fig. 7.5.: The structures on wafer 2 are clearly visible after the exposure although the resist has not been developed.

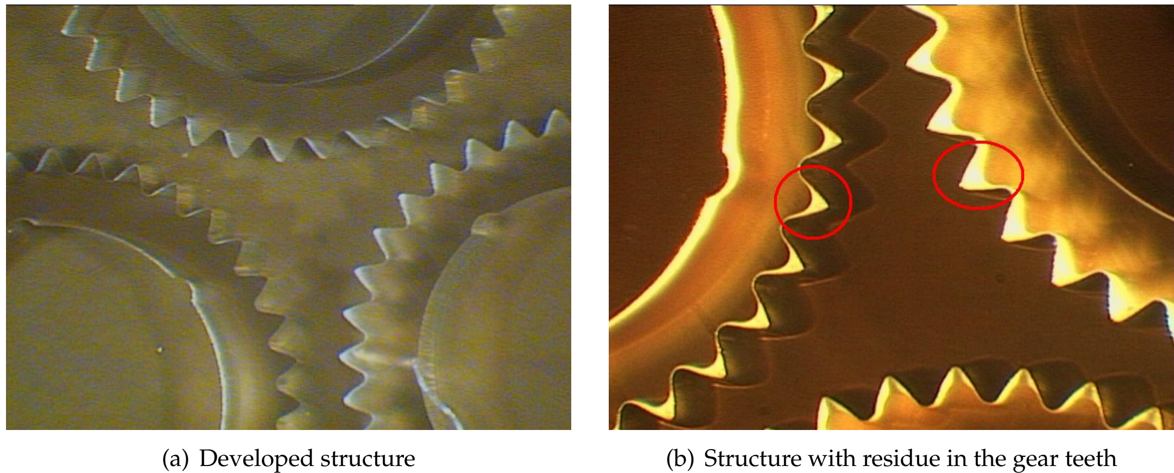

(a) Developed structure (b) Structure with residue in the gear teeth

Fig. 7.6.: Pictures of the exposed and developed wafers made with an optical microscope. (a) Wafer 1 with well developed structures. (b) Picture of wafer 3. At the light regions (highlighted) resist residues are visible.

Apart from wafer 3 the resist layer showed a reduced adhesion to the wafer substrate at large area structures. This effect is supposed to result from internal stress occurring in the baked and hardened resist due to the cross linking of the resist. In general, it is a challenge to obtain a good adhesion at large continuous areas as the adhesion depends on the applied dose and the resulting degree of cross linking: the higher the dose, the more uniform the cross linking. However, the adhesion becomes worse with increasing degree of cross linking [59]. Thus, the choice of dose has to be a compromise between a uniform cross linking and a good adhesion.

As wafer 1 offered the highest quality, this one was chosen for further investigations.

7.2.2.1. SEM micrographs of the developed structures

In order to obtain more information about the quality of the developed structures, scanning electron microscopy (SEM) was performed at the Leibniz-Institut für Analytische Wissenschaften - ISAS - e.V. with the help of Dr. Alex von Bohlen. As the resist was charged by the electron jet, it was sputtered with a thin gold layer. The electron energy of the SEM microscope was 5 keV and the working distance was about 10 - 11 mm. The free-standing resist structures remaining after the chemical development are clearly visible in figure 7.7. The high edge steepness of the structures as well as the orthogonality between structure surface and sidewall are obvious. A small washout (<0.5 µm) at the transition from structure to substrate is visible in figure 7.7(d).

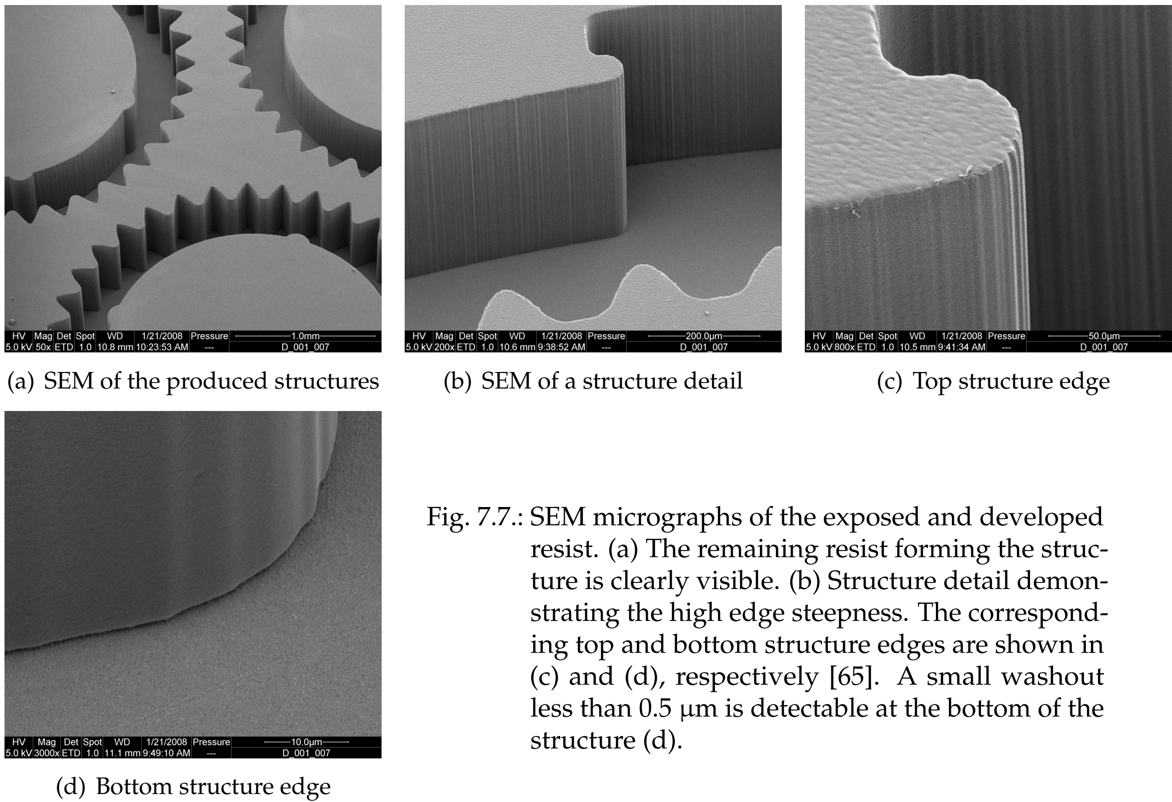

(a) SEM of the produced structures (b) SEM of a structure detail (c) Top structure edge

(d) Bottom structure edge

Fig. 7.7.: SEM micrographs of the exposed and developed resist. (a) The remaining resist forming the structure is clearly visible. (b) Structure detail demonstrating the high edge steepness. The corresponding top and bottom structure edges are shown in (c) and (d), respectively [65]. A small washout less than 0.5 μm is detectable at the bottom of the structure (d).

These results confirm the feasibility of the production of high quality micro structures at DELTA. Thus, the first test measurements carried out at ISASline BL 2 as a proof of principle were a real success. These results were essential for the decision to build a dedicated deep x-ray lithography beamline at DELTA.

Although the quality was very good in general, there occurred vertical striations at the sidewalls, which become visible in figures 7.7(b) and 7.7(c). These striations were the origin for a profound investigation of the sidewall roughness (section 7.4).

7.3. Measurements at BL 1

First test measurements were performed at BL 1, exposing three wafers with a diameter of 4 inch and a SU-8 resist thickness of about 560 μm. The exposure procedure and the results of the structure quality investigations are presented in this section.

7.3.1. Exposure procedure

The first wafer labeled T004 was exposed with the graphite mask (figure 7.1(c)) already used for the measurements at BL 2. It was exposed under similar conditions as wafer 1 during the test measurements at BL 2. The scanner covered each moving direction (up/down) in 2 seconds with a velocity of $v_{\text{stepper}} = 93\ \frac{\text{mm}}{\text{s}}$. The graphite mask was fixed at a distance of about 8 mm from the wafer surface. The next two wafers (T005 and T006) were exposed with two different titanium masks in order to find out if the striations result from the mask membrane material (see detailed analysis in section 7.4). The gap between mask membrane and resist surface was adjusted to 25 μm by applying 25 μm thick Kapton foil on the mask edges. In addition, 200 μm Kapton foil was fixed as a filter at the mask holding entrance, reducing the low energy radiation to decrease the top-to-bottom ratio (tbr) to about 5.

Wafer T005 was exposed through the titanium mask shown in figure 7.1(a) and for the exposure of wafer T006 the mask seen in figure 7.1(b) was applied. For the exposure of wafer T006 the stepper run time was decreased to 11.0 seconds in up-direction and 10.3 seconds downwards yielding motor velocities of $v_{\text{stepper}} = 17\ \frac{\text{mm}}{\text{s}}$ and $18\ \frac{\text{mm}}{\text{s}}$, respectively. This modification was made to investigate a possible effect of the stepper velocity on the structure quality. The important parameters for the exposure setup at BL 1 like mask material, adjusted gap, applied filters, and motor velocities are summarized in table 7.2. The resist thickness of the exposed wafers, the electron beam current at DELTA, the exposure time, and the applied exposure doses are listed in table 7.3 for a better overview.

Tab. 7.2.: Setup parameters for the exposure at BL 1.

	mask material	Kapton filter [μm]	gap[μm]	$v_{\text{stepper}}\ \left[\frac{\text{mm}}{\text{s}}\right]$
T004	graphite	none	8000	93
T005	titanium	200	25	93
T006	titanium	200	25	up: 17 down: 18

Tab. 7.3.: Exposure parameters at BL 1.

	$d_{resist}[\mu m]$	$I_e[mA]$	$t_{exp}[min]$	$D_t\left[\frac{J}{cm^3}\right]$	$D_b\left[\frac{J}{cm^3}\right]$	tbr
T004	557	105	5	86	16	5.3
T005	556	81	11	103	20	5.1
T006	560	113	10	130	25	5.2

All three exposures were performed at a pressure of about 10^{-3} mbar inside the exposure chamber. After each exposure the wafer was removed from the exposure chamber and placed on a hotplate with a temperature of about 55°C for the post exposure bake, where it remained for 10 minutes. The hotplate was then heated up to 70°C within 5 minutes and the wafer remained at this temperature for the next 40 minutes. Afterwards, the hotplate was switched off and the wafer slowly cooled down on the hotplate.

7.3.2. Results of the exposures at BL 1

After the chemical development performed by MRT the structure quality was investigated by microscopy and electron scanning microscopy. The SEM was performed using an Everhart-Thornley-Detector (ETD), in order to measure the secondary electrons and to obtain a topographic image of the sample (see chapter 3.3).

7.3.2.1. Exposure results for the graphite mask

The photograph taken from the exposed and developed wafer clearly shows the gear wheel structures (figure 7.8).

Microscopy investigations performed by MRT show accurately developed structures without structure cracks nor resist residues in the gear teeth (figure 7.9) [66]. The adhesion at large continuous individual areas is bad as indicated by the interference fringes shown in figure 7.9(a). This effect was already observed and explained in section 7.2.2.

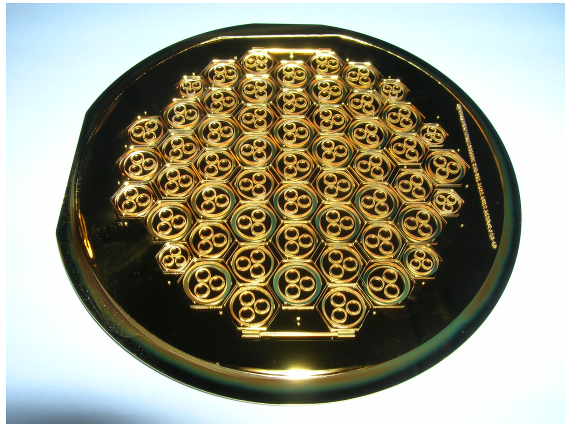

(a) T004 - Overview of the exposed wafer

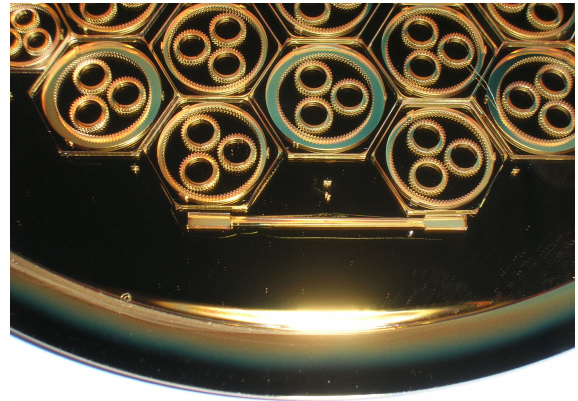

(b) T004 - Detailed view on the developed gear wheels

Fig. 7.8.: Photograph of the exposed and developed wafer. (a) Overview of the gear wheel structures. (b) Detailed view on the wheel structures. The remaining resist and the generated cavities due to the chemical development are clearly visible.

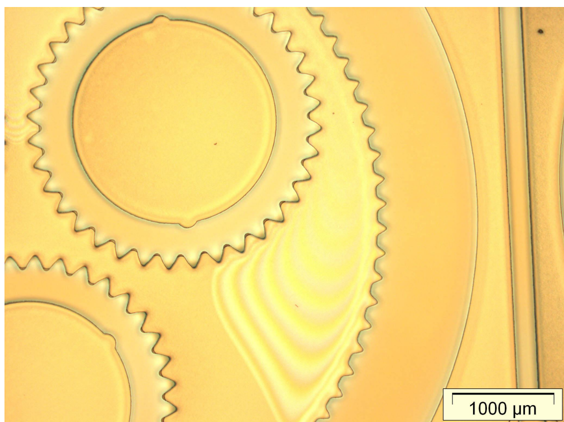

(a) T004 - Bad adhesion

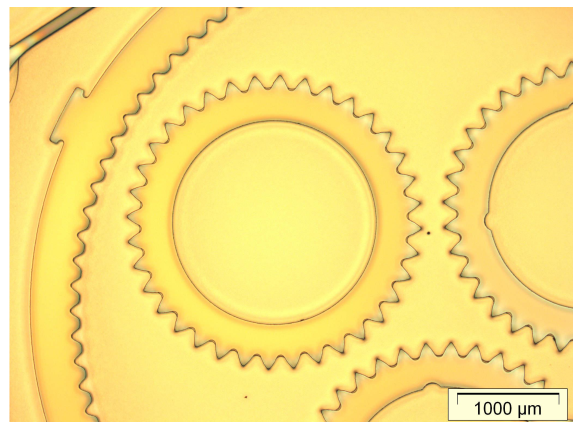

(b) T004 - Good adhesion

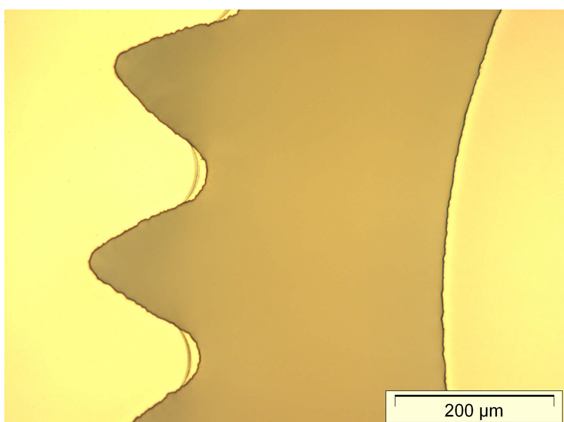

(c) T004 - Accurately developed gear teeth

Fig. 7.9.: Micrographs of wafer T004. (a) At individual large areas the adhesion between the resist and the wafer is decreased, indicated by the interference fringes. (b) These structures show a good resist adhesion. (c) The gear teeth are well developed. There are no residues visible in the spaces between the gear teeth [66].

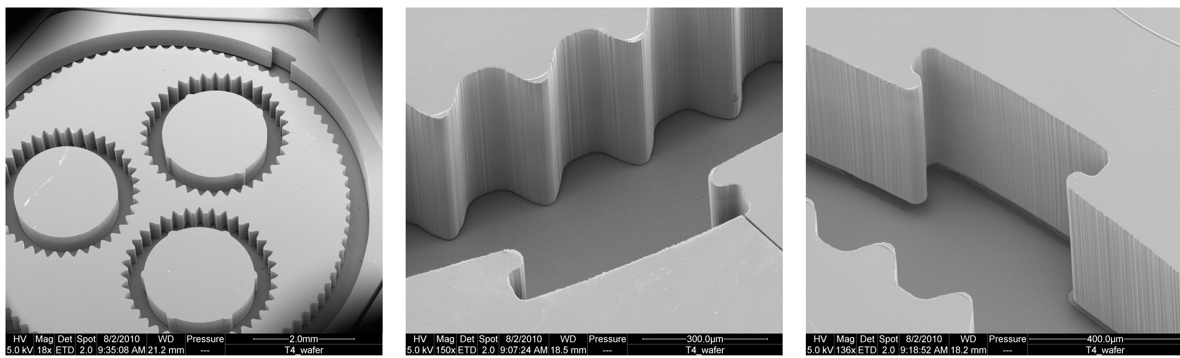

(a) T004 - Overview of a structured area

(b) T004 - Sidewalls of gear teeth

(c) T004 - Outer sidewall of large wheel

Fig. 7.10.: (a) Set of gear wheels consisting of one large and three smaller wheels. (b) and (c) The structures have very steep sidewalls and perpendicular edges. Vertical striations as observed during the test measurements at BL 2 are visible.

After development and optical microscopy investigations the wafer was investigated by scanning electron microscopy measurements performed at the Leibniz-Institut für Analytische Wissenschaften - ISAS - e.V. The results are shown in figures 7.10 to 7.12.

An overview of a typical set of gear wheels is shown in figure 7.10(a). Such sets are distributed in a close package on the whole wafer. The larger wheel has an outer diameter of about 7 mm and the smaller wheels have an inner diameter of approximately 2 mm. Figure 7.10(b) shows the wall of the gear teeth and in figure 7.10(c) the view is directed to the inner sidewall of the large wheel. The high edge steepness and the perpendicular walls are visible as well as the vertical striations that were already seen at the test structures produced at BL 2. The gap between substrate and resist, seen in figure 7.10(c), reveals a detachment of the resist from the wafer due to mechanical stresses in the large-area structures. These stresses occurred during the wafer preparation after the development as the wafer had to be divided into several pieces to perform different investigations like SEM and confocal microscopy.

Although the structures have very perpendicular sidewalls with a high edge steepness, two different kinds of imperfections appear: a small overhang at the edges of the resist surface is visible (figure 7.11) and small globular objects are found at several edges, especially at the bottom structure edges (figure 7.12).

The overhang may be caused by a slight overexposure [11, 15]. In this case, energy was deposited in the regions below the mask absorber structures leading to a generation of a thin insoluble layer. The major part of the layer was removed during the chemical development. The rough edges presented in figure 7.11 show an edge with an overhang and an edge where

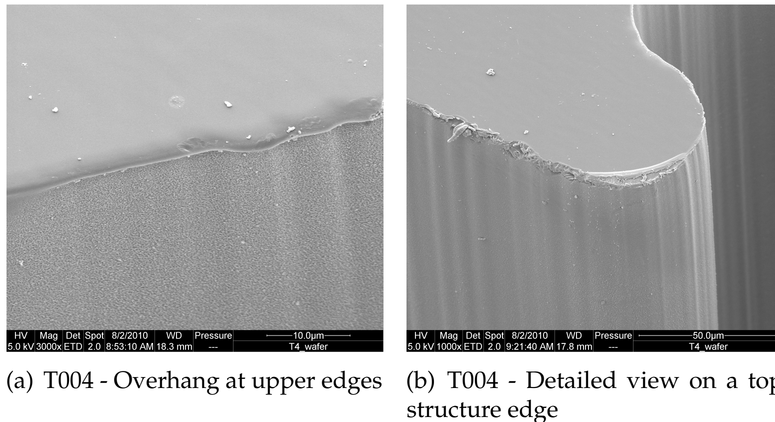

(a) T004 - Overhang at upper edges

(b) T004 - Detailed view on a top structure edge

Fig. 7.11.: (a) Upper structure edge with a small overhang. The thin surface layer broke during the chemical development and removed parts of the top structure edge (b).

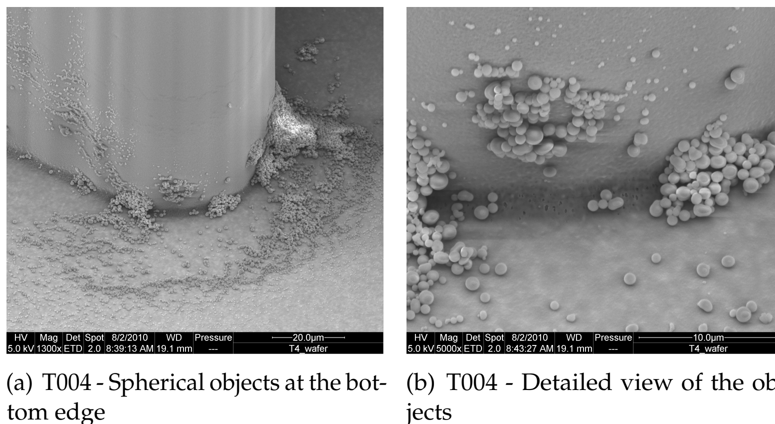

(a) T004 - Spherical objects at the bottom edge

(b) T004 - Detailed view of the objects

Fig. 7.12.: Globular objects at the bottom edge. The beads have a diameter of less than 1 µm. (b) Detailed view on the small spheres.

the layer broke off some part of the surface. These imperfections at the resist surface are not very severe for industry applications as the resist surface is removed by lapping before the electroplating process of LIGA. The lapping has two major tasks: it removes surface imperfections and leads to a constant resist height across the wafer.

The beads with a diameter of approximately 1 µm mainly accumulated at the bottom edge although they appeared at the sidewalls as well (figure 7.12). The beads were generated during the chemical development. The end of the development is initiated by rinsing the wafer with isopropanol. If the development is not complete, the remaining dissolved resist precipitates in the isopropanol and accumulate at the sidewalls and mainly at the bottom structure edges [59].

In conclusion, the exposed and developed structures provide a good quality. The wafer features well developed structures with perpendicular sidewalls and without cracks. Sidewall striations in the observed order of magnitude are negligible for the production of gear wheel

structures. As a small resist overhang at the structure edges is removed prior to electroplating, this effect can be ignored in case the underlying structure is well developed. However, the partly bad adhesion and the globular objects may disturb the production of micro components. The latter effect can be avoided by increasing the chemical development duration. As a good adhesion of large resist areas on the substrate is a general challenge depending on substrate quality and purity as well as exposure dose, further experience is required. However, as these imperfections do not affect the entire wafer, electroplating will yield suitable micro components.

7.3.2.2. Exposure results for titanium masks

Photographs of the exposed and developed wafers show the line structure of tension test bodies and the acceleration sensor structures (figure 7.13). The exposure quality of the developed structures was investigated by different microscopy techniques.

On the basis of microscopy performed by MRT the following results were obtained [66]: Apart from a generally good development, the structures show resist residues in small structure gaps (black areas in figure 7.14) because thin skin like layers, covering these gaps, inhibit the resist dissolution as the chemical developer cannot penetrate these regions. The thin transparent surface layers are clearly visible by light microscopy. Layer residues remaining after the chemical development stick to structure edges and partly cover the structures.

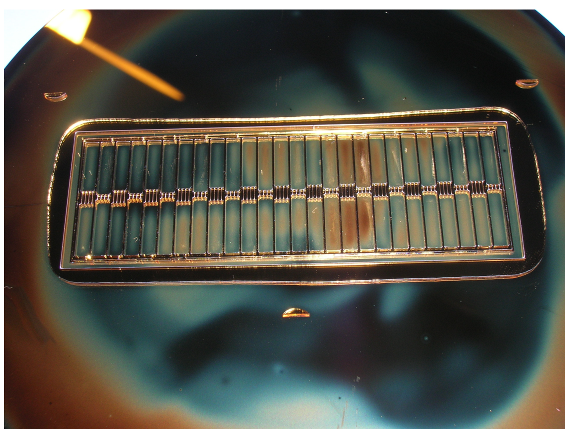

(a) T005 - overview of the exposed wafer

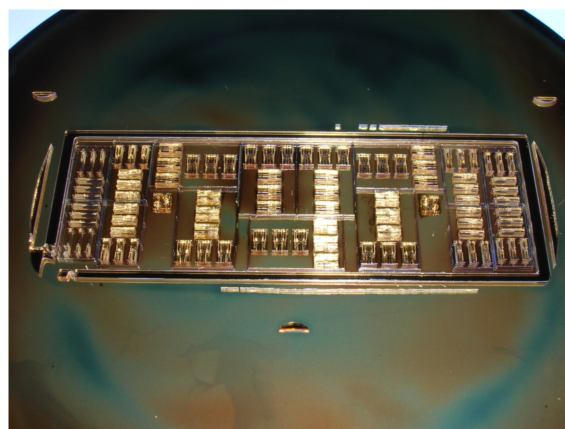

(b) T006 - overview of the exposed wafer

Fig. 7.13.: Photographs of the wafers exposed with titanium masks. (a) The line structure is well developed. (b) As the acceleration sensor structures have a very fine substructure the details are not resolvable by photograph.

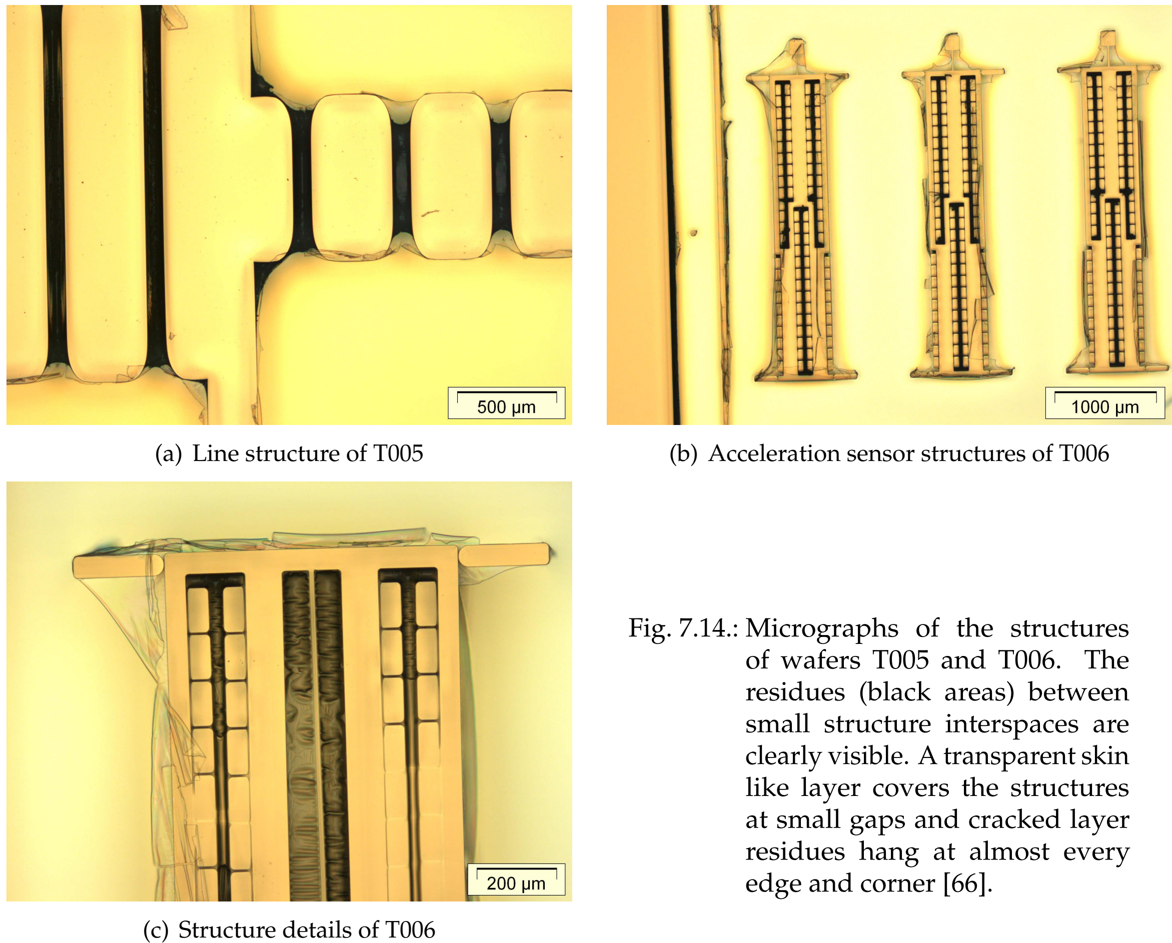

(a) Line structure of T005

(b) Acceleration sensor structures of T006

(c) Structure details of T006

Fig. 7.14.: Micrographs of the structures of wafers T005 and T006. The residues (black areas) between small structure interspaces are clearly visible. A transparent skin like layer covers the structures at small gaps and cracked layer residues hang at almost every edge and corner [66].

The resist at both wafers shows a good adhesion to the substrate and there are no cracks in the structures.

The results obtained from scanning electron microscopy investigations are shown in figure 7.15. Apart from a small washout at the transition between structure wall and substrate, the structure shows a good adhesion on the wafer (figure 7.15(b)).

The high structure orthogonality with the high edge steepness is shown in figure 7.15(c). A decreased sidewall roughness compared to the exposures with graphite masks is visible. Skin like layers cover the spaces between near structure walls and they are spanned between the corner edges. At areas where structure walls have a big distance to each other, the skin like layers crack and layer residues can be seen as an overhang at the top structure edges (figure 7.15(d)).

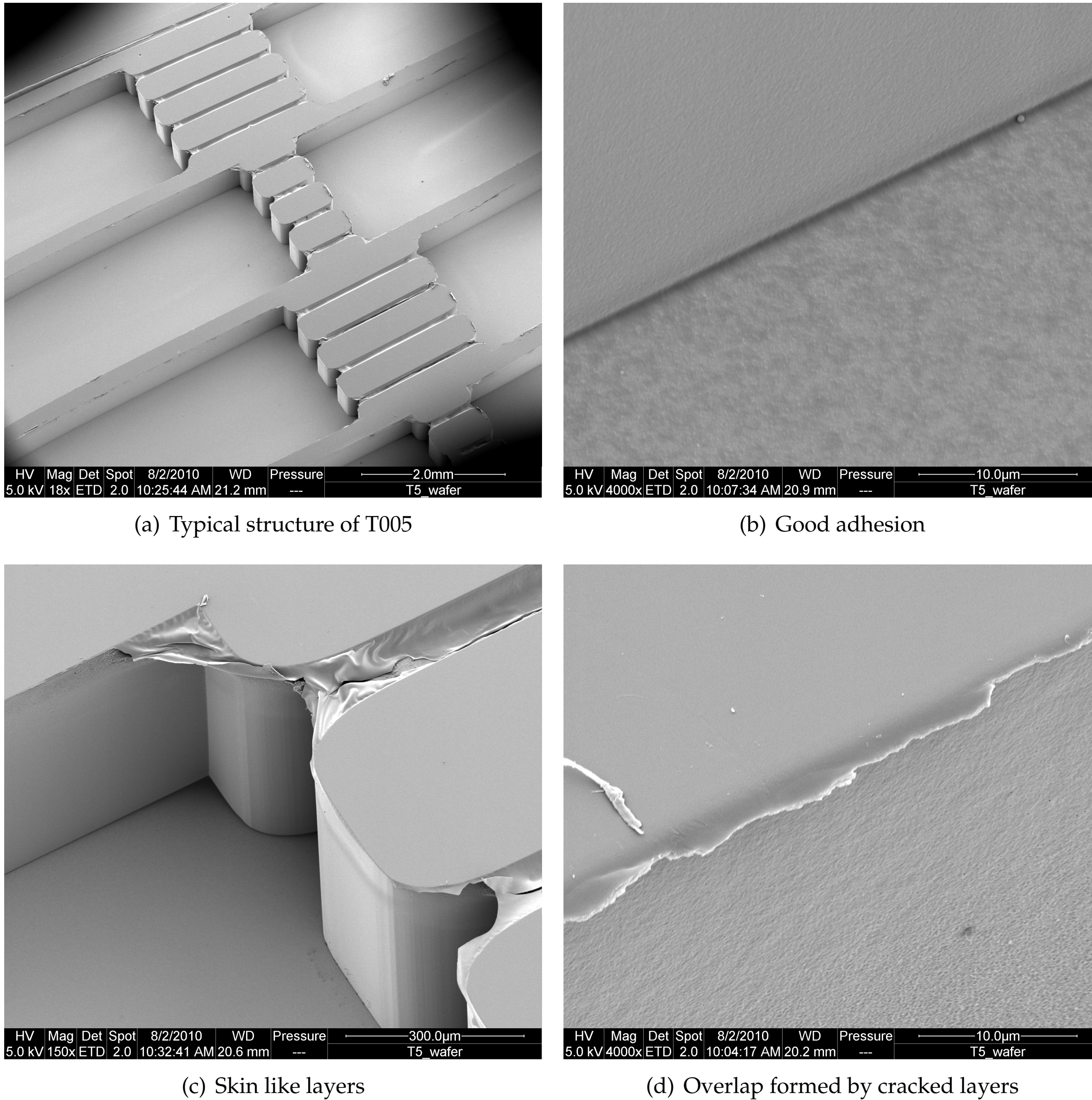

(a) Typical structure of T005

(b) Good adhesion

(c) Skin like layers

(d) Overlap formed by cracked layers

Fig. 7.15.: Different aspects of wafer T005 exposed with a titanium mask. (a) Overview of a typical structure formation that is repeated several times on the wafer. (b) The structures adhere very well to the substrate. (c) Skin like layers stick to several edges and corners. The structure sidewalls appear very smooth. (d) Cracked layers form an overhang at the top structure edges.

Tab. 7.4.: The calculated exposure dose at the top and the bottom of the resist for different absorber thicknesses for both wafers T005 and T006. The top doses beneath the gold absorber structures are higher than the permitted maximum dose.

	T005		T006	
d [μm]	D_t [J/cm^3]	D_b [J/cm^3]	D_t [J/cm^3]	D_b [J/cm^3]
10	0.52	0.39	0.65	0.49
15	0.14	0.11	0.18	0.14
20	0.05	0.04	0.06	0.05

These layers result from an overexposure [15]. As the absorber thickness of the titanium masks was not known at the time of exposure the dose could not be calculated correctly.

After the test exposures, the absorber thickness was estimated by the mask provider to be 10 - 20 μm [61]. Considering this information, the dose in the resist beneath the absorber was calculated with the software DoseSim [64]. The results for different absorber thicknesses are listed in table 7.4 for both performed exposures with titanium masks.

To remove the unexposed areas completely during the chemical development, the maximum permitted dose beneath the absorber is less than 0.05 $\frac{J}{cm^3}$, the threshold dose for chemical solubility [15].

The calculated doses for different absorber thicknesses reveal that even a 20 μm thick gold absorber leads to an overexposure. An absorber thickness of 25 μm gold would suffice even for the more intensely exposed wafer T006. Then, the doses would be $D_t = 0.022 \frac{J}{cm^3}$ and $D_b = 0.018 \frac{J}{cm^3}$.

Images of wafer T006 confirm the results obtained for wafer T005. Small gaps are again covered by skin like layers (figure 7.16(a) and 7.16(b)). A layer thickness <0.5 μm was estimated from figure 7.16(c). Figure 7.16(d) shows the perfect adhesion between structure and substrate without cracks or washouts.

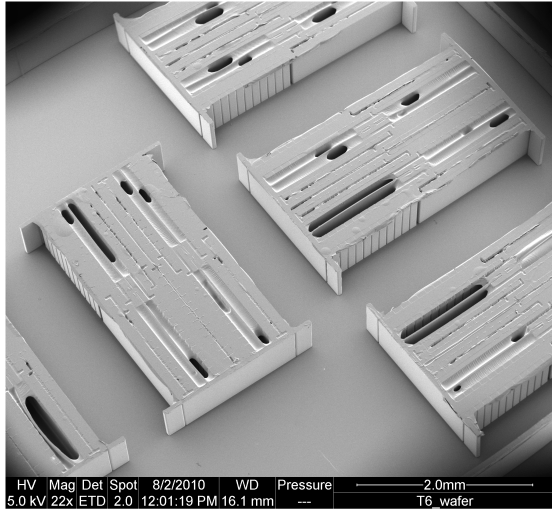

(a) Typical structures on wafer T006

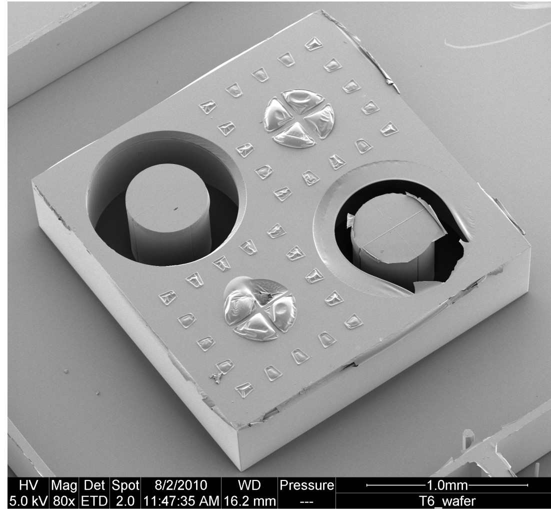

(b) Skin like layers

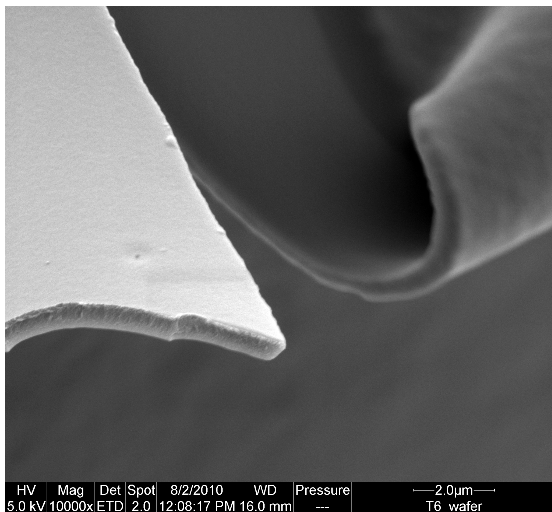

(c) Thickness of the skin like layers

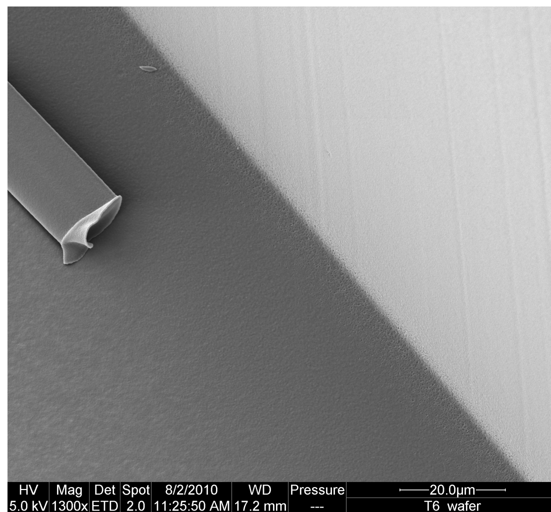

(d) Good adhesion

Fig. 7.16.: SEM micrographs of wafer T006. (a) Overview of the acceleration sensor structures. The structures are covered with skin like layers. (b) Another structure on T006. Small gaps are completely covered with a layer. However, the layer cracked at some regions. (c) Detailed view on the skin like layer. Its thickness is approximately 0.5 µm. (d) The structure adheres very well at the wafer substrate. Neither cracks nor washouts are visible.

On the left side of figure 7.16(d) a small rod is partially visible. Such rods appear at arbitrary positions all over the wafer (figure 7.17). As the rods have the same height as the desired structures, it is assumed that they result from defects in the gold absorber. A detailed investigation of the mask by optical microscopy revealed identically shaped defects in the gold absorber at the respective rod positions.

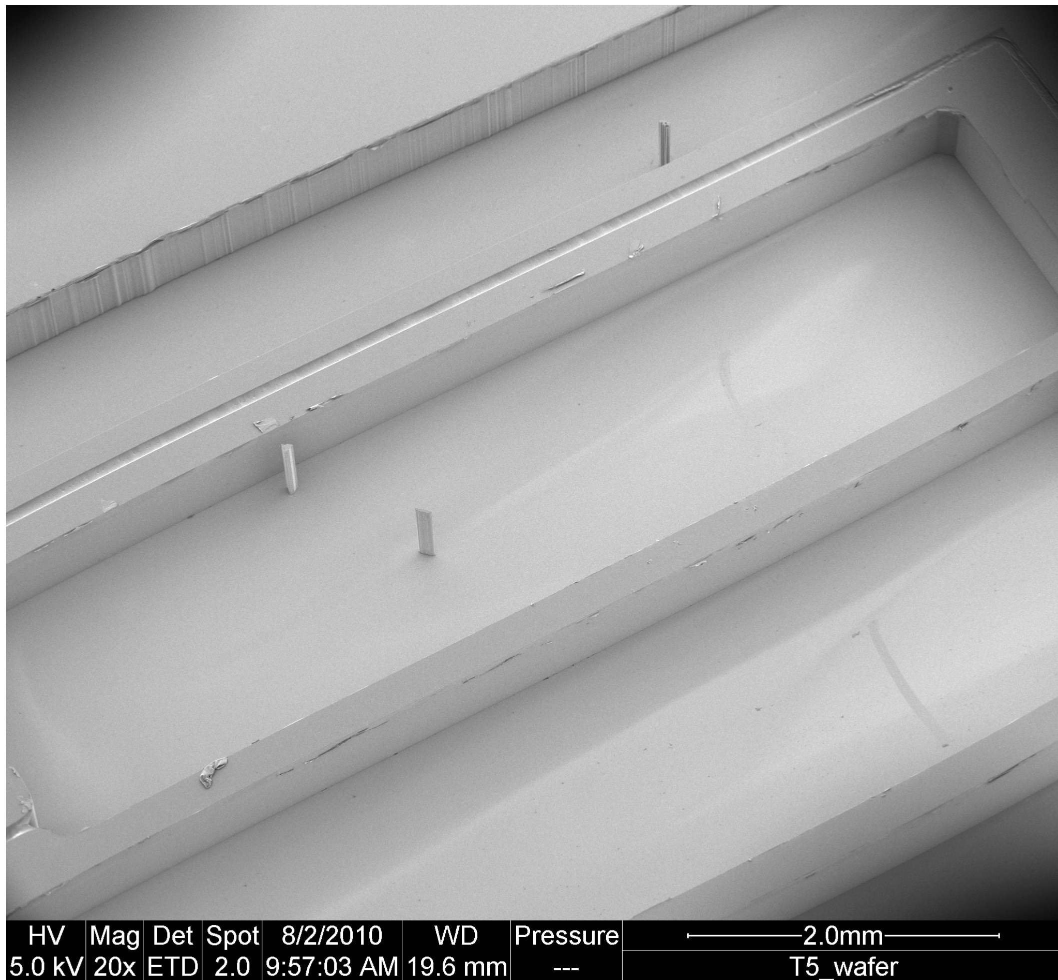

Fig. 7.17.: Several rods appear at arbitrary positions on the developed wafer.

Figure 7.18 shows SEM micrographs of differently shaped rods on developed, free areas on the wafer and the corresponding microscopy image of the gold absorber defect (figure 7.18(b) and 7.18(d)).

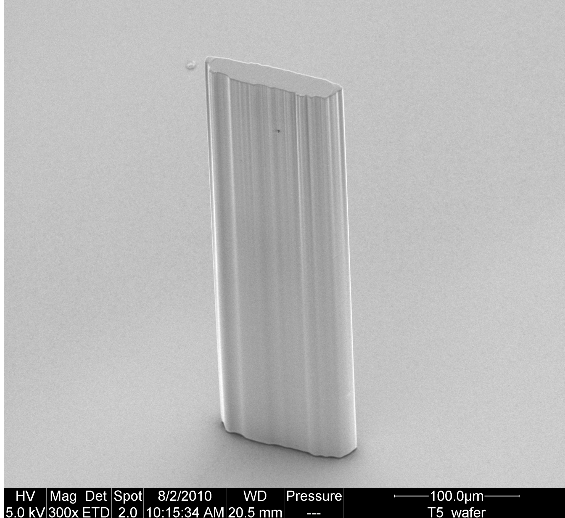

(a) SEM of a long flat rod

(b) Micrograph of the corresponding absorber defect

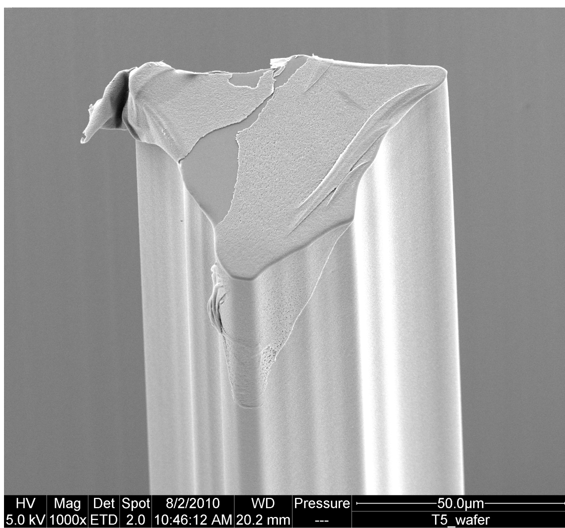

(c) SEM of a triangular rod

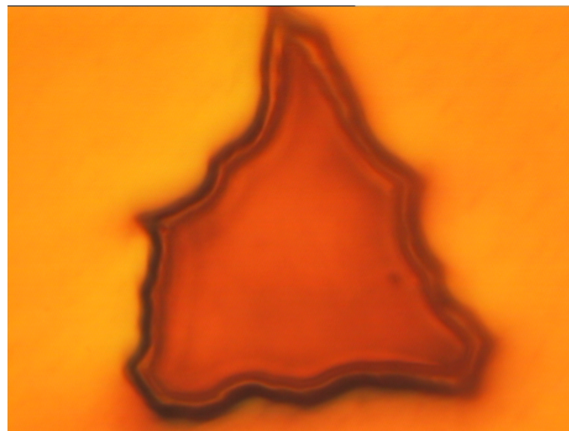

(d) Micrograph of the triangular absorber defect

Fig. 7.18.: The SEM images show the rods on the developed wafer. The micrographs present the corresponding defects in the gold absorber structure of the mask.

A very impressively shaped rod with dimensions of 65 x 20 μm^2 has a hole in its mid whith an edge length of approximately 8 μm (figure 7.19). Two small rods standing next to each other are located in front of the rod and used for an estimate regarding the aspect ratio. As they have a diameter of approximately 5 μm, the aspect ratio is about 100:1. The edges and the sidewalls show a high orthogonality as well as a very good edge steepness. The observed free standing rods, although not desired, make obvious that it is possible to produce high structures with a small base area and a very good adhesion. Using perfect masks without absorber failures, the generation of rods is avoided.

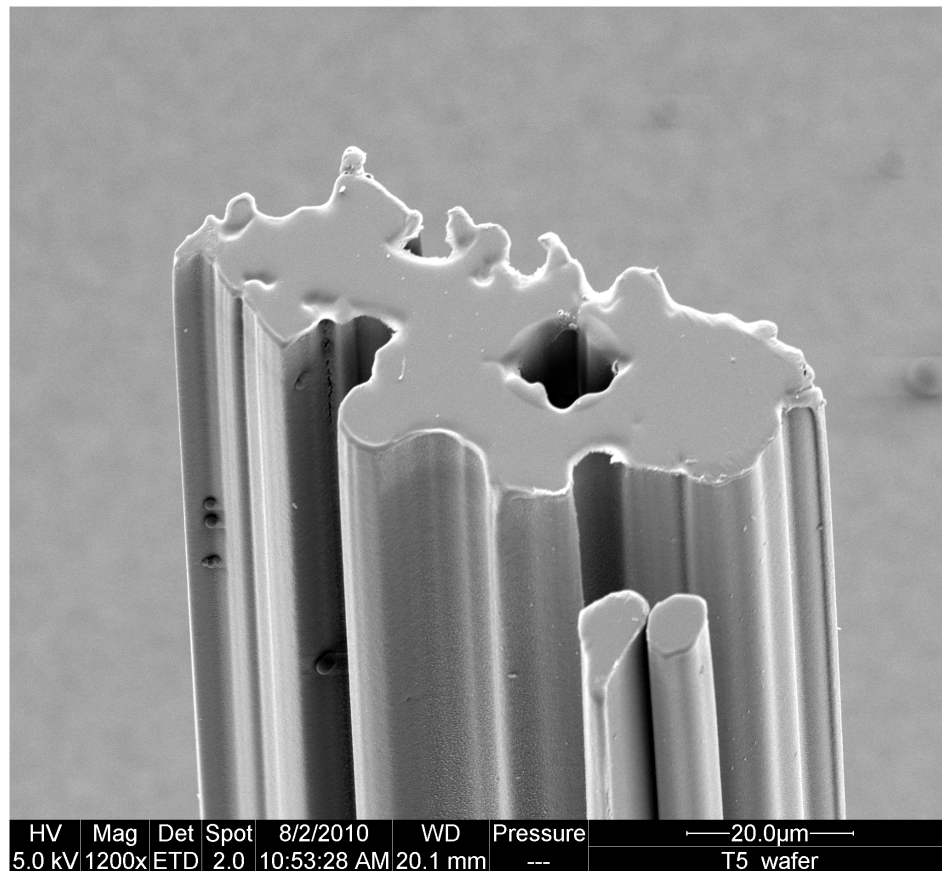

Fig. 7.19.: This impressively shaped rod appeared on wafer T005. It consists of one large rod with a centered hole and two separate standing small rods.

Focussing the optical microscope on either the gold absorber surface or the underlying mask membrane, the outer rod shape and the shape of the remaining gold area in the defect center are visible (figure 7.20). The two separately standing small rods are obvious in figure 7.20(a).

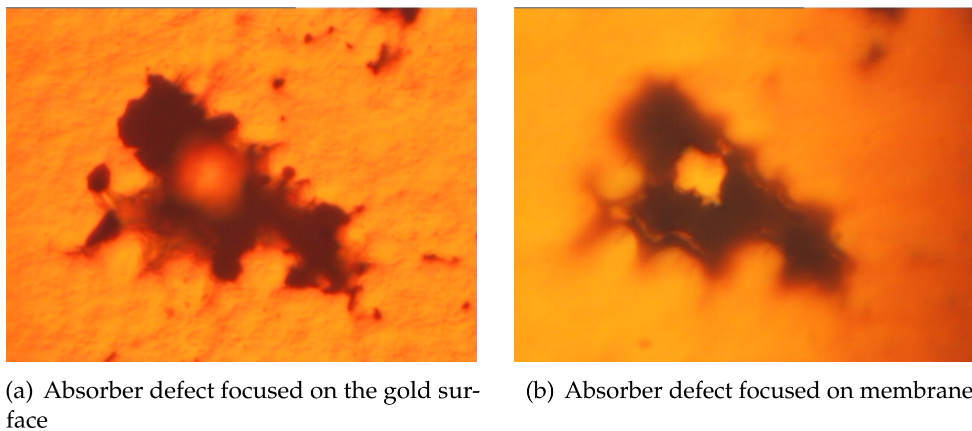

(a) Absorber defect focused on the gold surface (b) Absorber defect focused on membrane

Fig. 7.20.: Depending on whether the image is focused on the gold surface or the membrane of the mask, the outer shape or the shape of the centered hole is visible.

Taking an overview of this defect a second failure appears at the mask absorber (figure 7.21). Focussing on the respective area on the wafer substrate, the corresponding shape becomes visible, i.e. the rod cracked and disappeared during wafer preparation.

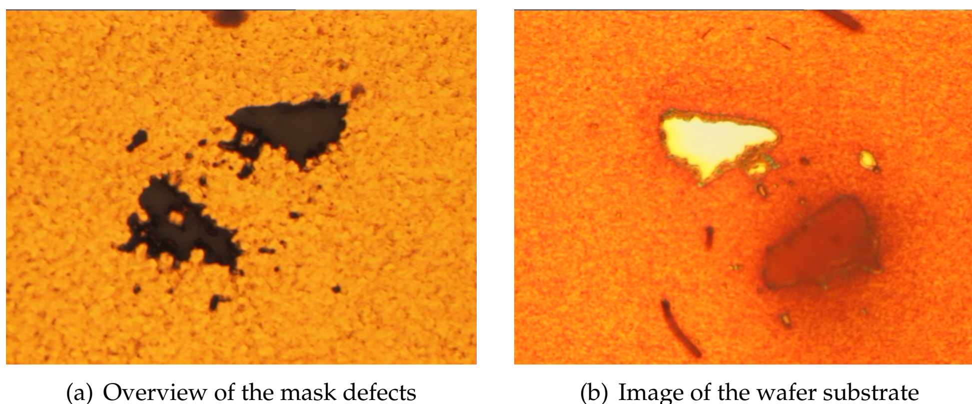

(a) Overview of the mask defects (b) Image of the wafer substrate

Fig. 7.21.: (a) Two defects in the mask absorber structure. (b) Microscopy image of the wafer focused on the substrate. The light area presents the base area of the cracked rod.

Apart from skin like resist layers, the wafers show a good structure quality. The developed spaces are clean and the structures have smooth sidewalls. In addition, the structures are very steep with an aspect ratio of about 100:1 and have a good adhesion on the resist. Skin like layers and the resulting insufficient chemical development of small structures will be prevented by decreasing the top to bottom dose ratio. Therefore, it is possible to produce high quality micro structures at BL 1 complying with industrial standards.

7.4. Sidewall roughness investigations

The striations seen at the sidewalls of the structures exposed with graphite masks were expected to be an effect of either the mask absorber edge profile or the mask membrane material.

7.4.1. Investigation of the mask absorber profile

The production process of an x-ray mask includes the writing of the structure by a fine particle jet. This process step is controlled by a computer program which contains the computer aided structure design. The structure shape is often designed by an adequate combination and superposition of polygons [2]. As a result it is possible that the absorber structure edges contain small corners which are transferred to the photoresist during exposure. The absorber edge smoothness was investigated by scanning electron microscopy.

In figure 7.22 the edge of the developed resist structure is opposed to the gold absorber edge on the mask. Both figures have the same scaling.

The dimension of the lateral striations at the resist structure is in the order of 3 μm. However, there is no comparable roughness observable at the edge of the gold absorber structure. The profile of the mask absorber edges can therefore be eliminated as a possible origin for the striations at the developed resist structure.

7.4.2. Effect of the membrane material

The investigation of the mask absorber edges showed that the sidewall roughness of the exposed structures does not depend on the shape of the absorber edges. Aigeldinger et al. investigated the sidewall roughness in dependence of the membrane material [27]. They found out that titanium leads to a minimum sidewall roughness of $R_q = 17$ nm. Therefore, titanium x-ray masks were used at BL 1 for a comparison.

The sidewall roughness of the differently exposed structures were determined by scanning electron microscopy as well as confocal microscopy. For the latter method the profilometer μsurf produced by the company NanoFocus was used. This profilometer is available at the ISF of the TU Dortmund (institute of metal-cutting manufacturing). SEM micrographs were taken at the Leibniz-Institut für Analytische Wissenschaften - ISAS - e.V.

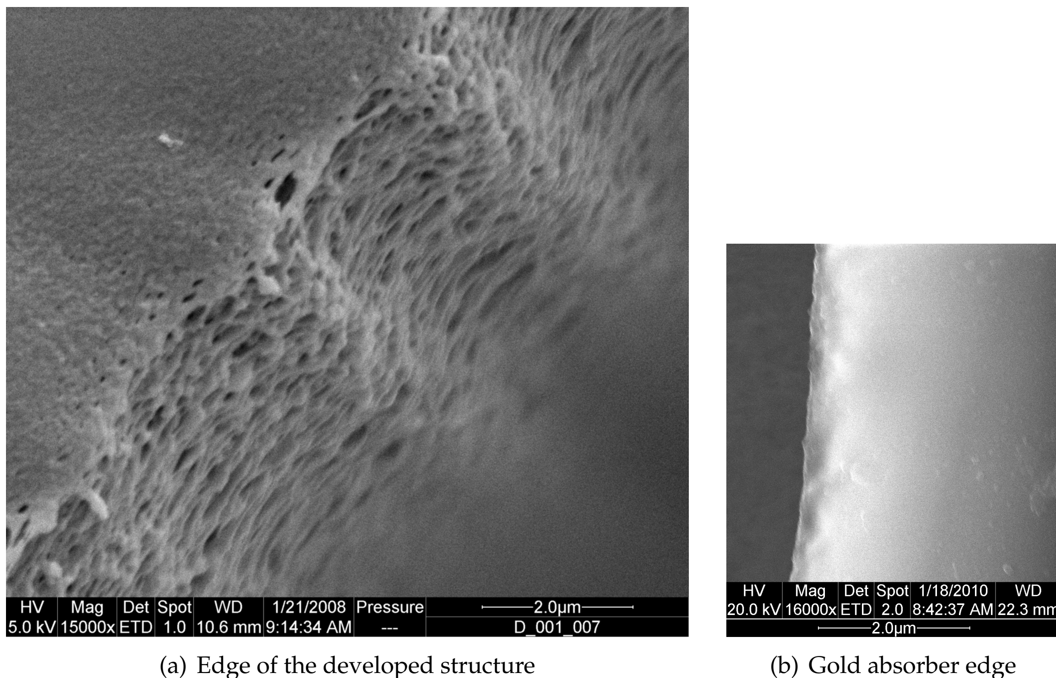

(a) Edge of the developed structure

(b) Gold absorber edge

Fig. 7.22.: Comparison of the smoothness of the structure edge and the gold absorber edge. The figures have the same length scales. The corrugations in the resist sidewall at a distance of about 3 µm cannot be found in the gold absorber edge.

The following samples were investigated:

- gear wheel structure exposed at BL 2 with the graphite mask (wafer 1),
- gear wheel structure exposed with the graphite mask during the first measurements at BL 1 (T004),
- tension test bodies exposed with a titanium mask during the first measurements at BL 1 (T005),
- acceleration sensor structure exposed with a titanium mask during the first measurements at BL 1 (T006).

Figure 7.23 shows typical SEM images of sidewalls of the investigated structures. These images clearly show a decreased sidewall roughness when using titanium masks.

The sidewall roughness was investigated quantitatively with the confocal microscope µsurf. Sidewall ares with dimensions of 200 - 450 x 690 - 800 μm^2 (height x length) were imaged. The analyzed areas had dimensions of 200 - 450 x 190 - 330 μm^2 (height x length).

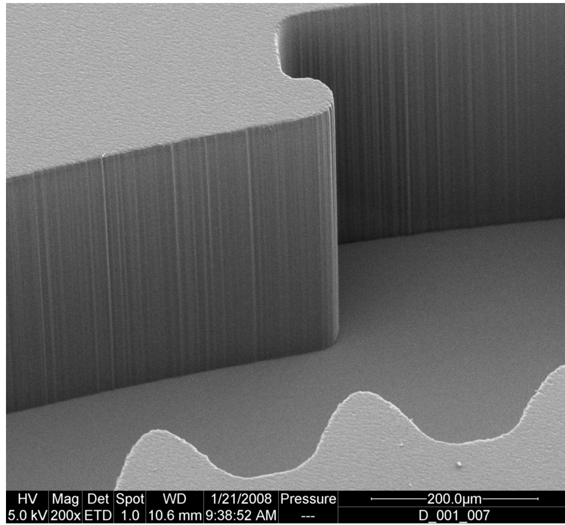

(a) Wafer 1 - graphite mask

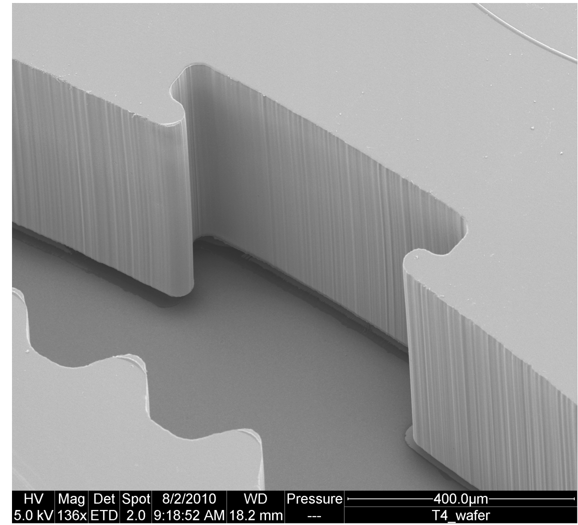

(b) T004 - graphite mask

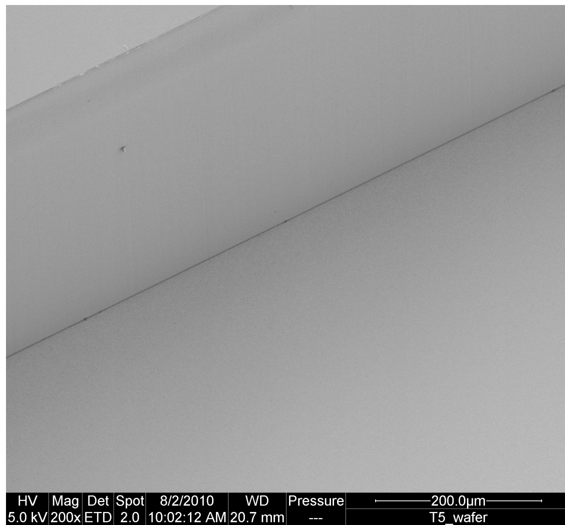

(c) T005 - titanium mask

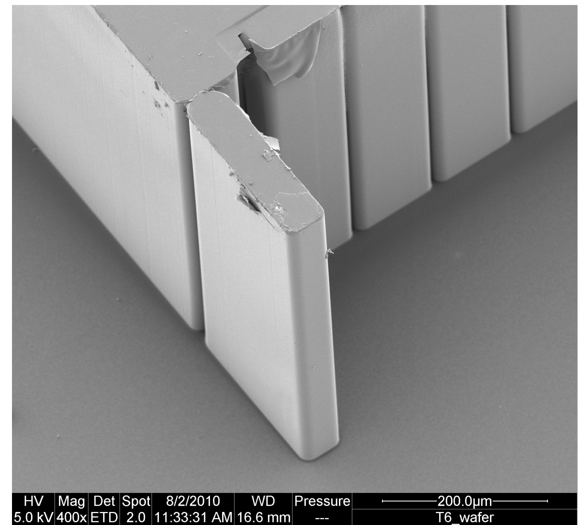

(d) T006 - titanium mask

Fig. 7.23.: Different sidewall roughnesses due to the choice of mask membrane material. Structures exposed with the graphite mask show an increased sidewall roughness compared to structures generated with titanium masks.

Several line profiles were measured across the analyzed area to determine the arithmetic and square mean roughnesses $\overline{R_a}$ and $\overline{R_q}$ of the sidewall.

An example of a line profile (across the entire imaged area) is shown in figure 7.24. The profile was measured perpendicular to the vertical striations and is composed of a roughness profile and an underlying waviness profile. The software subtracts the waviness from the measured profile yielding the pure roughness profile. The roughness value R for each line is determined from the waviness-free roughness profile using equations 3.17 and 3.18. The $\overline{R}$ values were obtained by averaging over all measured line profiles, yielding the roughness and the corresponding standard deviation listed in table 7.5.

Tab. 7.5.: Roughness in dependence of different mask materials.

	$\overline{R_a}$ [nm]	$\overline{R_q}$ [nm]	analyzed area [μm^2]
wafer 1	320±40	400±60	318 x 330
T004_1	1080±120	1450±210	449 x 302
T004_2	380±60	560±80	419 x 223
T005_1	130±20	180±60	205 x 273
T005_2	120±10	170±10	223 x 273
T006_1	90±10	160±20	263 x 270
T006_2	170±10	240±60	223 x 190
T006_3	100±30	140±30	356 x 273

The roughness at the first investigated position at wafer T004 (T004_1) seems to be severely increased compared to the roughnesses determined for graphite mask exposures, which are about $R_a = 350$ nm and $R_q = 480$ nm. Aigeldinger et al. found $R_q = 365$ nm for an exposure using a graphite mask and Coane determined $R_a = 200$ nm [27, 67]. Considering the standard deviation of the measurements performed at the ISF, the result of Aigeldinger is comparable to the results for a exposure with a graphite mask at BL 1. Although Coane determined a lower roughness than measured by Aigeldinger and at BL 1, the results are of the same order of magnitude.

The roughness determined from exposures performed with titanium masks is in the range $R_a = 90 - 170$ nm and $R_q = 140 - 240$ nm. The exposure of T005 and T006 show similar roughnesses keeping the high standard deviation in mind. Thus, the wafer stepper velocity has no significant effect on the sidewall roughness.

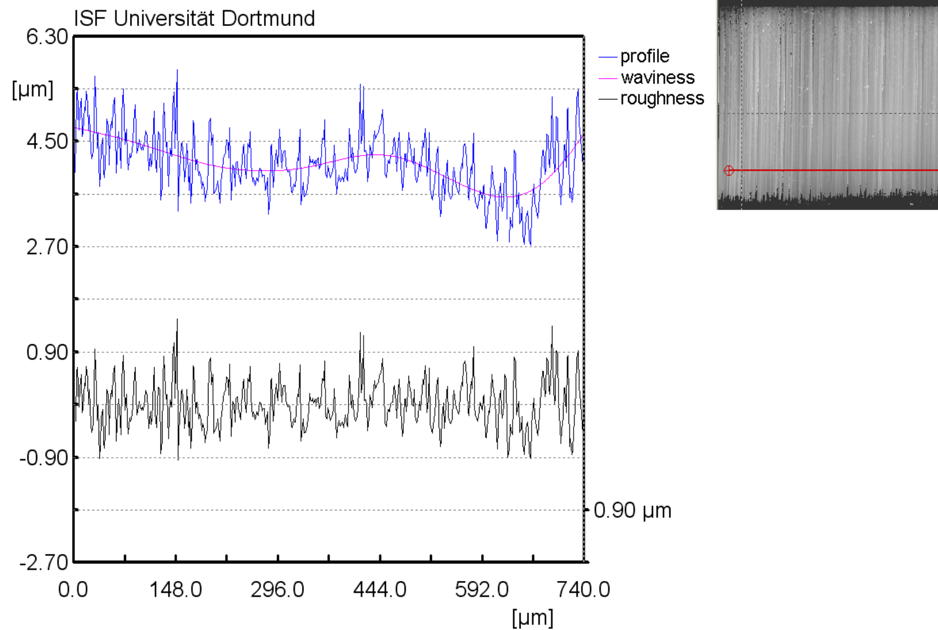

(a) Line profile across wafer 1

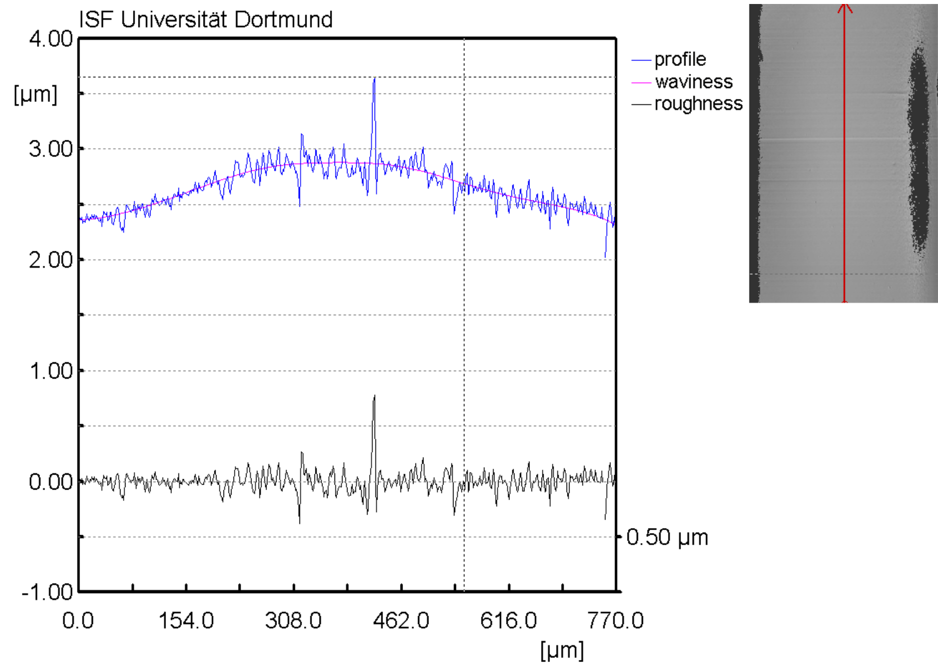

(b) Line profile across wafer T006_3

Fig. 7.24.: Example line profiles across sidewalls generated by exposures that were performed with a graphite mask (a) and a titanium mask (b). The exposure with a titanium mask offers a much smoother sidewall than structures generated with a graphite mask.

Considering measurements 1 and 3 of wafer T006, as they offer the lowest determined roughness, the roughness of titanium mask exposures is about 3 - 4 times lower than exposures performed with graphite masks. Although the sidewall roughness of $R_q = 17$ nm measured by Aigeldinger [27] and $R_a = 13$ nm determined by Mappes [20] could not be obtained for titanium mask exposures at BL 1, the higher quality of structures produced by exposures with titanium masks compared to structures generated by a graphite mask is obvious.

In addition to the pre-mentioned measurements, three line profiles were measured manually across the sidewalls for each investigated area. The lines were positioned in the middle, the top and the bottom region.

Tab. 7.6.: Roughness parameters determined from line profiles, that were laid in the mid, the upper and lower region of the investigated area. Structures generated by titanium masks offer a significantly lower sidewall roughness.

sample	line position	R_a [nm]		sample	line position	R_a [nm]
wafer 1	top	436		T005_2	top	117
	mid	408			mid	122
	bottom	322			bottom	128
T004_1	top	1024		T006_1	top	66
	mid	1083			mid	80
	bottom	1116			bottom	97
T004_2	top	547		T006_2	top	147
	mid	450			mid	162
	bottom	429			bottom	178
T005_1	top	108		T006_3	top	83
	mid	131			mid	64
	bottom	150			bottom	79

The arithmetic mean roughness R_a determined from the individual line profiles (table 7.6) do not show a systematic variation from top to bottom region. As only three lines were measured manually for each area it is not possible to draw a definite conclusion if the roughness changes consistently from top to bottom.

The increased sidewall roughness using graphite masks in contrast to titanium masks was explained by Coane to be an effect of x-ray scattering from graphite [67]. Aigeldinger confirmed this result after detailed investigations of different mask membrane materials [27].

Altogether it has to be kept in mind, that the structure quality, which includes different aspects like adhesion, cracks, sidewall roughness, structure fidelity, etc. depends on several process parameters. These are the temperatures during the substrate coating, the exposure and

the development, the resist thickness and the exposure dose. In addition the resist/developer-system and the mask contrast (mask absorber thickness in dependence of the resist height) are affecting parameters. A study of the structure quality in dependence of several process parameters was performed by Achenbach [24].

7.5. Conclusion

The measurements performed to investigate the structure quality of the exposed wafers at DELTA clearly demonstrated that deep x-ray lithography is feasible at DELTA:

- The exposed structures were accurately developed and showed perpendicular sidewalls and a high edge steepness.
- The high sidewall roughness observed at structures exposed with graphite masks was explained as an effect due to the mask membrane material. Using e.g. titanium masks, the roughness was decreased by a factor of 3 - 4.
- The small globular objects seen at the graphite mask exposure at BL 1 were a result of the duration of development.
- For future exposures the gold absorber thickness of the mask will be known and the dose can be adapted. Therefore the generation of skin like layers will be avoided.
- The appearance of small rod-like artifacts was explained by failures in the mask absorber structure.
- However, these rods demonstrate that a high aspect ratio of 100:1 is feasible at BL 1.

Although the procedure of deep x-ray lithography at DELTA has to be improved and as further investigations are required, the exposures performed at BL 1 demonstrate the feasibility of DELTA and BL 1 to produce high quality structures with a high aspect ratio. Considering the current experience, micro structures suitable for industrial applications will be produced at BL 1 in the near future.

7.6. X-ray reflectivity investigations of the resist

Additionally to the beamline setup and the structure quality investigations, the photoresist SU-8 was analyzed concerning its surface roughness by x-ray reflectivity measurements. The experiment and the obtained results are presented in the following.

7.6.1. Sample environment and preparation

The x-ray reflectivity measurements were performed at the TU Dortmund, faculty of physics, using a Bruker D8 Advance diffractometer in $\Theta - \Theta$ geometry. X-rays are generated by a copper anode with a characteristic $Cu_{K_{\alpha,1}}$ photon energy of 8048 eV. The sample stage is movable along the three spatial directions. A detailed description of the D8 diffractometer can be found in [34, 68].

As the investigated photoresist is sensitive to visible light, the windows of the sample cell, shown in figure 7.25, were covered with black Kapton. The sample cell has an inner diameter of 110 mm and contains an insert to hold the coated wafer (disk at the right side of figure 7.25).

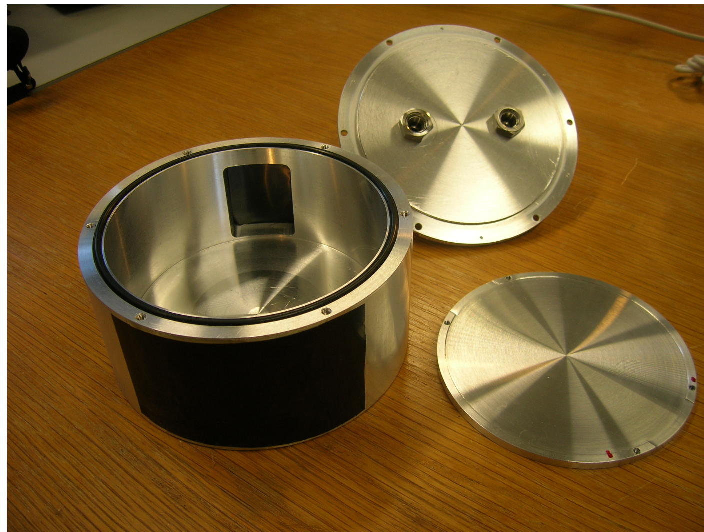

Fig. 7.25.: Sample cell for reflectivity measurements at the D8 laboratory diffractometer. The cell consists of two windows covered with black Kapton foil. The disk at the right side is the wafer holder. The top cover of the sample cell is shown in the background.

4 inch wafers were prepared at the faculty of ET&IT of the TU Dortmund (see chapter 6.2). The wafer spin coating process was followed by the removal of the bulge (see chapter 6) yielding suitable wafers for x-ray reflectivity investigations.

7.6.2. Measurement and analysis

During the sample alignment the scans revealed a splitting of the reflected beam, indicating a surface waviness of the resist layer which is assumed to be a result of the spin coating process or the heating procedure of the soft-bake. In order to reduce this splitting effect, the sample was moved along the y-direction of the diffractometer (perpendicular to the beam in the horizontal plane) to find a less wavy position. However, the subsequent data analysis showed that measurements under extreme low incident angles did not yield suitable data, as this region is extremely sensitive to surface waviness.

Figure 7.26 shows an example reflectivity curve and the corresponding measurement of the diffuse scattering signal with a detector offset of 0.1°.

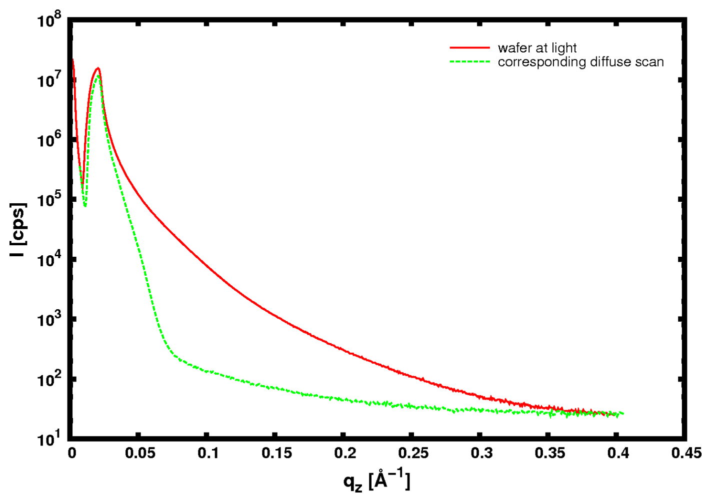

Fig. 7.26.: Reflectivity curve (red) and diffuse scan (green) of the coated wafer. At low scattering angles the diffuse scattering reaches an intensity in the order of magnitude of the reflectivity curve.

As the signals of the diffuse scattering and the specular reflected beam are in the same order of magnitude for low incident angles, a subtraction of the diffuse scattering signal yielded useless data sets. Hence, the diffuse scattering signal was neglected for low incident angles and only the reflectivity signal at high scattering angles was analyzed for two wafers.

The first wafer, labeled wafer 4, was handled at amber light all the time. Reflectivity curves of the native SU-8 resist were taken (curve refl 02), followed by a bake of the wafer with respect to the PEB procedure. After cooling down, the wafer was investigated a second time in order to analyze the influence of the wafer heating (curves PEB 01 and PEB 02).

A second wafer was kept at daylight for one day in order to determine the effects of exposure (curves wafer at light 01 - 04).

The obtained reflectivity curves were fitted in the region of the critical angle using the software LSFIT in order to determine the Fresnel reflectivity (see attachment A.1) [36]. Afterwards, the reflectivity curves R were divided by the corresponding Fresnel reflectivity R_F and $\ln(R/R_F)$ as a function of q_z^2 was analyzed at high q_z-values as this region contains information about the smallest interfacial roughness of the investigated sample system (see section 3.2). The corresponding curves in figure 7.27 were shifted against each other for better illustration. All data sets were fitted between $q_z^2 = 0.07$ Å^{-2} and the highest q_z-value, as this region was linear for all investigated curves.

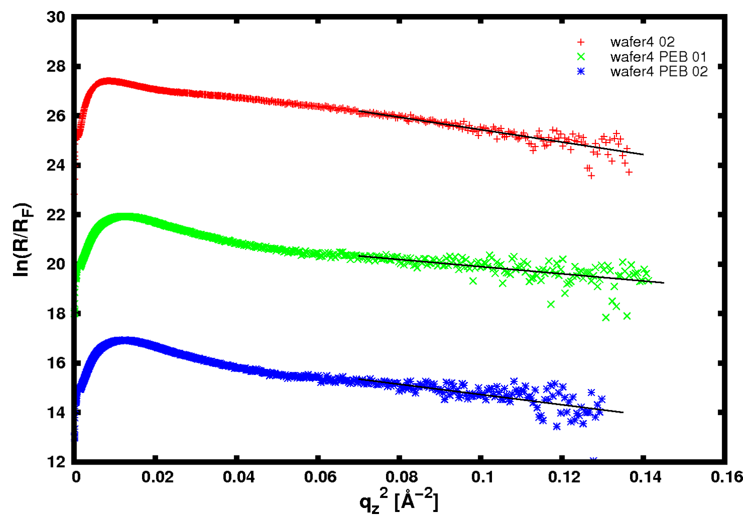

(a) Reflectivity curves of wafer 4

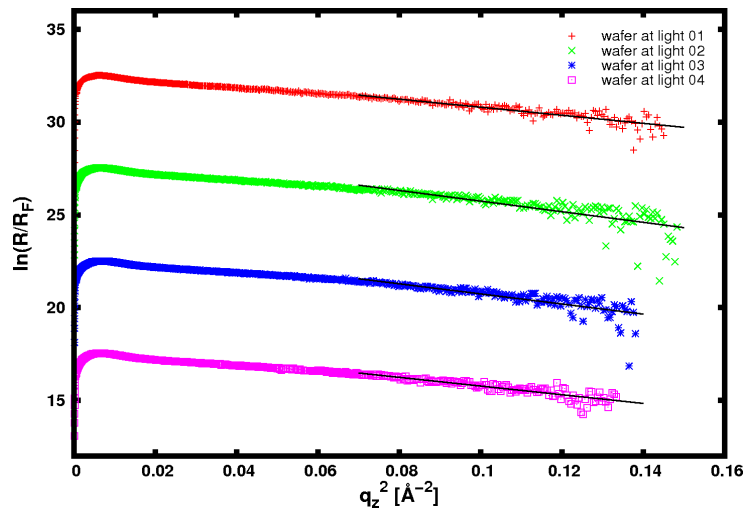

(b) Reflectivity curves of the wafer kept at light

Fig. 7.27.: $\ln(R/R_F)$ versus q_z^2 obtained for wafer 4 and the wafer that was kept at light. The linear sections at high q_z-values are fitted by a linear regression. They contain the information about the surface roughness of SU-8.

As the investigated SU-8 layers have a thickness of approximately 300 - 350 μm, the x-ray penetration depth into the resist is too low to reach the substrate surface. Therefore, the determined roughnesses listed in table 7.7 correspond to the SU-8 surface roughness.

Tab. 7.7.: Roughnesses obtained from the surface of the SU-8 layer. The values determined from the wafer that was kept at light are constant within the uncertainties. Wafer 4 shows a decreased roughness for the first measurement after the PEB.

	Wafer 4			Wafer kept at light			
	refl 02	PEB 01	PEB 02	refl 01	refl 02	refl 03	refl 04
σ [Å]	5.0 (± 0.1)	3.8 (± 0.2)	4.5 (± 0.2)	4.7 (± 0.1)	5.4 (± 0.1)	5.2 (± 0.1)	4.8 (± 0.1)

All measurements show roughnesses in the range of 3.8 - 5.4 Å. Wafer 4 seems to have a decreased roughness at the first measurement performed after the PEB. The other values are constant within the uncertainties.

The surface tension γ of SU-8 can be calculated from [69][70]

$$\sigma^2 = \frac{k_B T}{2\pi\gamma} \ln\left(\frac{q_{max}}{q_{min}}\right) , \tag{7.1}$$

where k_B is the Boltzmann constant, T the temperature and q_{min} and q_{max} define the lower and upper wave vector cutoff, respectively.

Considering the average surface roughness $\sigma = 4.8$ Å of SU-8, the surface tension at room temperature is determined to $\gamma = 25 \frac{mN}{m}$. This value is characteristic for polymers. The investigation of PDMS (polydimethylsiloxane) by Sauer et al. revealed a surface tension of 20 $\frac{mN}{m}$ [71] and Sprung et al. determined surface tensions of 38 $\frac{mN}{m}$ and 36 $\frac{mN}{m}$ for polypropylene glycol PPG-425 and PPG-4000, respectively [72].

In conclusion, reflectivity data of two wafers were analyzed regarding the surface roughness of SU-8. Further systematic investigations regarding possible resist modifications due to a variation of process parameters remain to future work.

An important challenge is the reduction of surface waviness, e.g. by a variation of the coating process parameters, i.e. spinning velocity, duration of spinning, temperature and duration of the soft-bake.

8. Summary and Outlook

The progress in device miniaturization during the last decades and the increasing demands regarding structure quality, component height, and lateral resolution of micro components required new technologies. The development of the process line LIGA, including x-ray exposure, electroplating, and molding, meets the respective requirements, as deep x-ray lithography (DXRL) using synchrotron radiation yields high aspect ratios, a high edge steepness and smooth sidewalls of the exposed resist structures. The subsequent process steps of electroplating and molding allow the production of high quality micro components in a high quantity.

Summary

Within this thesis proof of principle measurements were performed successfully at the ISAS-Line BL 2, demonstrating the feasibility to accomplish DXRL at DELTA. Based on this result, a DXRL beamline was planned and constructed at the synchrotron radiation facility DELTA in Dortmund. The synchrotron radiation of the 1.5 T bending magnet with a critical photon energy of 2.2 keV is well suited for exposure of thick resist layers. The white photon beam at BL 1 with a height of 10 mm and a width of about 100 mm at the experimental end station allows full-wafer exposures of 4 inch wafers. A beryllium window absorbs the low energy radiation and reduces the heating of mask and wafer.

The complete beamline setup was accomplished within the course of this thesis, including the beamline commissioning. Thus, BL 1 is ready for DXRL exposures of 4 inch wafers.

The photon beam at BL 1 was characterized during the beamline commissioning phase and was found to provide a high photon flux homogeneity and a uniform beam profile along the beam width of 97 mm. Furthermore, the beam intensity maximum is located in the vertical center of the beryllium window aperture, thus the photon beam meets the demands for large-area DXRL exposures.

Micro structures exposed at DELTA using 550 µm thick SU-8 resist layers were investigated regarding structure quality, sidewall roughness, and aspect ratio. The structures were well developed and showed a high edge steepness with an aspect ratio of about 100:1. Apart from a good adhesion in general, the adhesion was reduced at large continuous structures. The appearance of thin skin like layers observed at structures exposed through titanium masks were found to result from a slight overexposure of the resist surface. This effect can be avoided in future work by knowledge of the mask absorber thickness.

As vertical striations were observed at the sidewalls of structures exposed through a graphite mask, the sidewall roughness was investigated in detail by confocal microscopy measurements. Determination of sidewall roughnesses from structures exposed through a graphite mask or titanium masks showed a dependence of the roughness on the mask membrane material. Using titanium masks the roughness was reduced by a factor of 3 - 4.

Within this study silicon wafers were cleaned and spin coated with the negative photoresist SU-8 to determine the surface roughness of SU-8 by x-ray reflectivity measurements (XRR). A surface roughness of about 4.8 Å was determined, yielding a surface tension of SU-8 of about 25 $\frac{\text{mN}}{\text{m}}$ which is a typical value for polymers.

Outlook

As the current end station requires at least two persons for wafer exchange, a new exposure chamber has to be constructed in future work. Furthermore, the control of the servo motor, moving the wafer mask system across the beam, has to be modified such that a computer based remote control is feasible, including a precisely tunable motor velocity.

The photon beam reveals good characteristics and the feasibility to expose 4 inch wafers. However, the observed beam width at the experimental end station is a little bit smaller than intended by the position of the collimator. This effect requires further investigations regarding the beamline alignment and the positions of collimator and beryllium window.

To obtain a good resist adhesion even at large area structures, the choice of adequate exposure doses needs further investigation. Since the structure quality regarding aspect ratio and edge steepness was qualitatively determined in this study, quantitative investigations remain to future work to find out the minimum feasible resolution, the maximum reachable aspect ratio and the quality of the edge steepness. Therefore, exposures using a particular quality test mask are recommended.

To determine the minimum feasible sidewall roughness, systematic measurements with respect to mask membrane materials and the influence of parameters like exposure dose and wafer stepper velocity are necessary.

Further investigations of SU-8 to find out systematic changes of the resist in dependence of exposure dose, temperature, and photon energy are required.

Conclusion

The performed studies showed that the constructed beamline is ready for operation and that it provides all necessary properties to perform DXRL exposures. Investigations of the structure quality of the first exposed wafers attest the feasibility of BL 1 to produce high quality micro structures. Following modifications of the end station will improve the exposure process and the applicability for industrial requirements.

A. Attachment

A.1. X-ray scattering from matter

To investigate the negative photoresist SU-8 regarding its surface structure, x-ray reflectivity measurements were performed as this is a surface sensitive x-ray scattering technique. The wavelength of x-rays is in the order of an Ångström (1 Å $= 10^{-10}$ m) yielding atomic resolution. The method of x-ray reflectometry (XRR) is outlined in the following section [35].

A.1.1. Scattering from surfaces and interfaces

For x-ray reflectivity experiments x-rays are considered as plane electromagnetic waves $\vec{E}(\vec{r}, t)$ depending on time t and space $\vec{r}$ [31]

$$\vec{E}(\vec{r}, t) = \vec{E}_0 \, e^{i(\vec{k} \cdot \vec{r} - \omega t)} \, , \tag{A.1}$$

where $\vec{E}_0$ is the amplitude of the plane wave, $\vec{k}$ is the wave vector and ω the angular frequency.

The wave hits the sample surface under an angle of incidence α_i, is reflected by the surface and scattered into the volume above the sample (figure A.1). The wave vector $\vec{k}_f$ of the scattered wave encloses an angle of α_f with the surface and is turned out of the plane of the incident wave and of the surface normal by an out-of-plane angle ϕ.

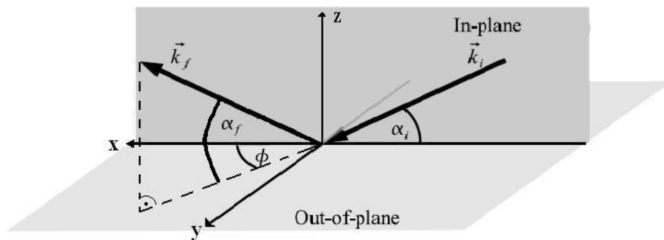

Fig. A.1.: The incident wave with wave vector $\vec{k}_i$ hits the sample and is scattered into the volume above the sample under an angle α_f with respect to the surface. ϕ denotes the deviation of $\vec{k}_f$ from the plane defined by the incident wave vector [34].

The scattering depends on the wave vector transfer $\vec{q}$, which is defined by the difference of the wave vectors of the incident and reflected waves

$$\vec{q} = \vec{k_f} - \vec{k_i}\,. \tag{A.2}$$

The wave vector transfer depends on the angles of incident and reflected wave, and on the out-of-plane angle

$$\vec{q} = k \begin{pmatrix} \cos(\alpha_f)\cos(\phi) - \cos(\alpha_i) \\ \cos(\alpha_f)\sin(\phi) \\ \sin(\alpha_f) + \sin(\alpha_i) \end{pmatrix} \tag{A.3}$$

with k as the wave number, which is identical for the incident and reflected wave in case of elastic scattering

$$k = |\vec{k_i}| = |\vec{k_f}| = \frac{2\pi}{\lambda}\,. \tag{A.4}$$

For XRR measurements $\phi = 0$ and $\alpha_i = \alpha_f = \Theta$ is assumed. Using these relations in equation A.3 the wave vector transfer has solely a contribution in z direction

$$q_{\text{XRR}} = q_z = \frac{4\pi}{\lambda} sin(\Theta)\,. \tag{A.5}$$

A.1.2. Basic principles

X-rays hitting matter interact with the electrons in the material. The electromagnetic waves excite the electrons, yielding oscillations. Therefore, the electrons themselves emit electromagnetic waves.

Scattering from a smooth interface assumes a discrete change of the index of refraction. For x-ray scattering the index of refraction n can be written as [31, 73]

$$n = 1 - \delta + i\beta\,. \tag{A.6}$$

Here, δ is the dispersion and β the absorption of the material.

The dispersion is a positive number and for x-rays it has a value of about 10^{-5}. Thus, the real part of the index of refraction is a little smaller than 1. As a result, external total reflection occurs in case that α_i is smaller than the critical angle of total reflection α_c. If x-rays strike the sample under an incident angle smaller than α_c (grazing incidence), the radiation only penetrates the sample to a depth of a few nanometer.

From Snell's law of refraction a dependency of the dispersion δ and the critical angle α_c is derived

$$\alpha_c = \sqrt{2\delta}\,. \tag{A.7}$$

Since the dispersion is in the order of 10^{-5} for x-rays, the critical angles are in the region of some mrad.

In the following the relation between the refraction index, the dispersion, and the electron density of the material will be derived. As the electrons in the sample oscillate due to irradiation, the scattering process can be described by the oscillator model. The scattering signal can be derived from the scattering amplitude [31]

$$f(\vec{q},\hbar\omega) = f^0(\vec{q}) + f'(\hbar\omega) + if''(\hbar\omega)\,. \tag{A.8}$$

Here, $f^0(\vec{q})$ is the atomic form factor, which corresponds to the fourier transformation of the electron density ρ. The terms f' and f'' are dispersion corrections of the atomic form factor and depend on the energy $\hbar\omega$ of the incident radiation. Considering the dispersion corrections, the dispersion and absorption can be written as

$$\delta = \frac{2\pi\rho r_0}{k^2}\sum_{j=1}^{N}\frac{f_j^0 + f_j'(\hbar\omega)}{Z}\,, \tag{A.9}$$

$$\beta = \frac{2\pi\rho r_0}{k^2}\sum_{j=1}^{N}\frac{f_j''(\hbar\omega)}{Z} = \frac{\mu}{2k}\,, \tag{A.10}$$

where Z is the atomic number of the elements in the investigated material. The absorption β can be calculated from the linear absorption coefficient μ.

Equations A.9 and A.10 can be reduced under the assumptions of a homogenous medium and a photon energy far away from the energy of absorption edges of the system to

$$\delta = \frac{2\pi\rho r_0}{k^2}\,, \tag{A.11}$$

$$\beta = \frac{\mu}{2k}\,. \tag{A.12}$$

Reflectivity

X-ray radiation striking a sharp ideally flat single interface under incident angles higher than α_c is partly reflected and partly transmitted into the sample under an angle α_t (figure A.2).

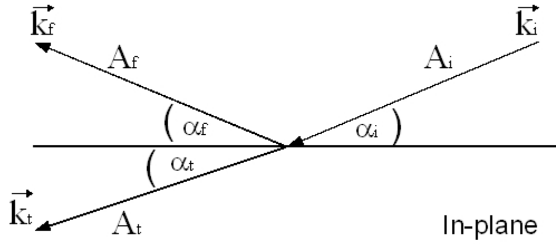

Fig. A.2.: The incident radiation is partially transmitted into the sample and reflected by the surface [35].

Here, A_i, A_f, and A_t are the amplitudes of the incident, reflected and transmitted waves, respectively. The transmission and reflection coefficients are given by [31, 34]

$$r = \frac{A_f}{A_i} = \frac{k_{i,z} - k_{t,z}}{k_{i,z} + k_{t,z}} \approx \frac{\alpha_i - \alpha_t}{\alpha_i + \alpha_t}, \quad (A.13)$$

$$t = \frac{A_t}{A_i} = \frac{2k_{i,z}}{k_{i,z} + k_{t,z}} \approx \frac{2\alpha_i}{\alpha_i + \alpha_t}. \quad (A.14)$$

As only components perpendicular to the surface are considered, $k_{i,z}$ and $k_{t,z}$ are the z components of the wave vectors of incident and transmitted wave. The reflectivity R and the transmission T are given by

$$R = |r|^2, \quad (A.15)$$

$$T = |t|^2. \quad (A.16)$$

The angle of transmission is calculated from α_i, α_c, and β following

$$\alpha_t = \sqrt{\alpha_i^2 - \alpha_c^2 + 2i\beta}. \quad (A.17)$$

On the left side of figure A.3, the transmission T is shown as a function of the angle of incidence (normalized to the critical angle). The transmission increases when approaching the critical angle and decreases afterwards to a constant value of 1. On the right side the reflectivity R of an ideally flat surface (Fresnel reflectivity) is depicted as a function of the incident angle, scaled to the critical angle. The effect of total reflection ($R = 1$) is visible for incident angles smaller than the critical angle of total reflection. Above the critical angle the reflectivity decreases with the fourth power of the incidence angle [32].

The imaginary part of the angle of transmission $\Im(\alpha_t)$ in combination with the wave number of the incident wave defines the penetration depth of the x-rays into the sample [31]

$$\Lambda = \frac{1}{2k_i \Im(\alpha_t)}. \quad (A.18)$$

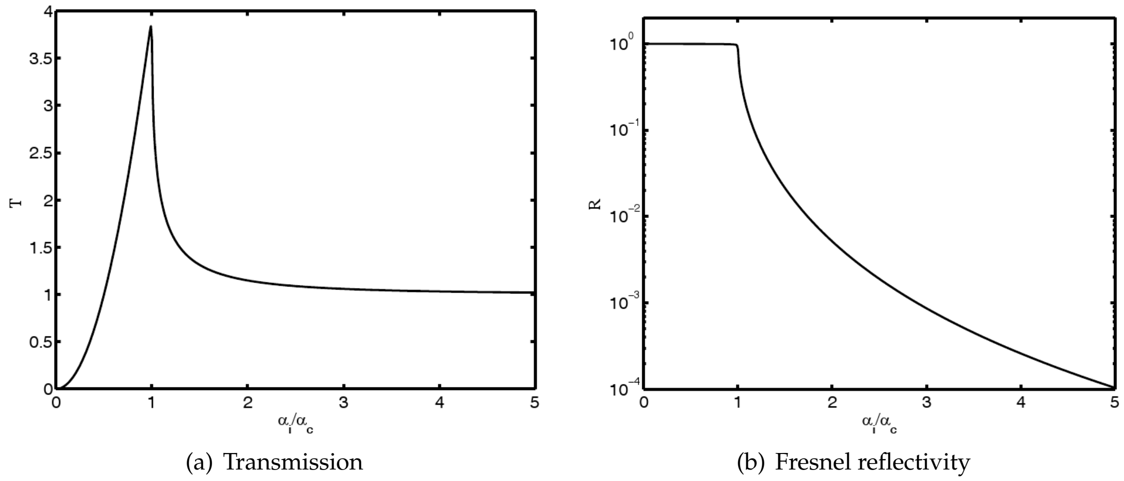

Fig. A.3.: (a) Transmission as a function of α_i/α_c. (b) Fresnel reflectivity. The region of total reflection below the critical angle and the subsequent, strong decrease of R is clearly visible [34].

Multi-layer systems

Up to now, an ideally flat single interface was discussed. In nature, systems are often multi-layered with rough interfaces. Therefore the above developed model for reflectivity is to be extended. As a first approach the roughness is disregarded and a system of several flat layers is examined. In a multi-layer system the layers lie on each other with the first layer at $z_1 = 0$, defining the interface between the top layer and the vacuum, which is considered as infinitely expanded (figure A.4). The undermost interface at z_N defines the substrate surface.

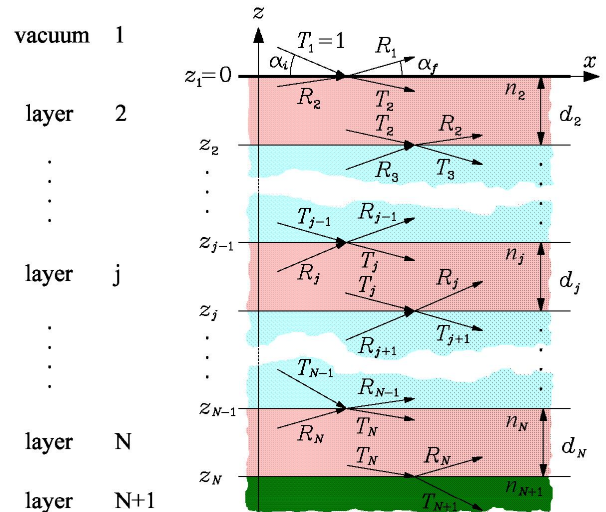

Fig. A.4.: System built by N layers with different thicknesses d_j and refractive indices n_j. Radiation striking the sample is partly reflected and transmitted at each interface [32].

The refraction indices are different for the individual layers and are given by

$$n_j = 1 - \delta_j + i\beta_j \,, \qquad \text{(A.19)}$$

and the layer thicknesses are

$$d_j = z_{j-1} - z_j \,. \tag{A.20}$$

The incident x-ray beam is reflected and transmitted at the individual interfaces. R_j and T_j are the amplitudes of the reflected and transmitted parts of the beam at the jth layer. T_1 is defined as the incident wave and thus is set to 1. As the thickness of the substrate is much higher than the radiation penetration depth, the substrate is considered as infinitely expanded and therefore the reflectivity R_{N+1} is set to 0.

Considering the correct phases for the addition of the single reflectivities, the total reflectivity of the system is obtained. L.G. Parratt developed a recursive algorithm to calculate the specular reflected intensity, which is measured in an experiment [74].

The relation from reflected to transmitted beam in the $(j+1)^{\text{th}}$ layer is given by

$$X_{j+1} = \frac{R_{j+1}}{T_{j+1}} \,. \tag{A.21}$$

For the overlying layer the relation can be calculated by

$$X_j = \frac{R_j}{T_j} = e^{-2ik_{z,j}z_j} \frac{r_{j,j+1} + X_{j+1}e^{2ik_{z,j+1}z_j}}{1 + r_{j,j+1}X_{j+1}e^{2ik_{z,j+1}z_j}} \,. \tag{A.22}$$

$r_{j,j+1}$ is the Fresnel coefficient of the jth layer and can be described by the z components of the wave vectors of the layers j and $j+1$

$$r_{j,j+1} = \frac{k_{z,j} - k_{z,j+1}}{k_{z,j} + k_{z,j+1}} \,. \tag{A.23}$$

The specular reflected intensity is obtained after N iterations

$$R = |X_1|^2 = |R_1|^2 \,. \tag{A.24}$$

As natural interfaces are rough, the model is expanded to multi-layered systems with rough interfaces. Considering ideally flat interfaces the density which is constant below and above the interface (and therefore the index of refraction) changes mercurially at the interface as a function of z. In reality the density along an interface is not constant but depends on the coordinates x,y, and z. For XRR measurements solely the signal in z-direction is investigated (equation A.5) and thus, the scattering signal reveals the laterally averaged roughness.

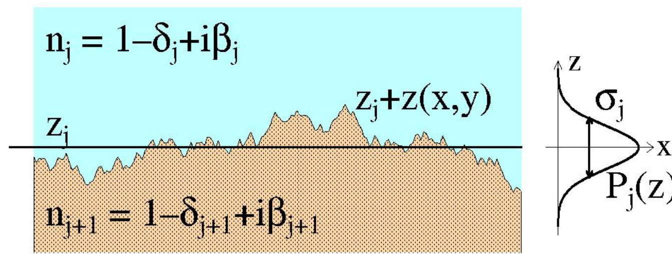

Fig. A.5.: Roughness is a phenomenon caused by differences in the height of a sample [32].

The height profile of a rough interface is shown in figure A.5. The black line indicates the average height. On the right side the height distribution around the average is shown which is a Gaussian distribution for the depicted example. The roughness σ of the system is defined as the full width at half maximum [32]. In many cases, the roughnesses are small compared to the layer thickness. In this case, it is sufficient to modify the Fresnel coefficients in order to describe the system. If the roughnesses are in the order of the layer thicknesses, the effective density model [32] has to be applied, in order to avoid discontinuities in the electron density profile.

A.2. Remark

Figure 7.1(c) is a photograph of the graphite mask provided by the company Micromotion GmbH.

The following figures show structures that were exposed at DELTA using the above mentioned graphite mask: 7.5, 7.6, 7.7, 7.8, 7.9, 7.10, 7.11, 7.12, 7.22, 7.23(a), 7.23(b).

Bibliography

[1] Markus Körfer; Entwurf und Aufbau einer Bestrahlungsanlage für die Röntgentiefenlithographie mit periodischer Bewegung der Synchrotronstrahlung am Speicherring Delta; Ph.D. thesis; Universität Dortmund; 1997

[2] Wolfgang Menz and Jürgen Mohr and Oliver Paul; Mikrosystemtechnik für Ingenieure; (Wiley-VCH; third edition; 2005)

[3] http://www.mieming-plus.at/images/224263995f0937914.jpg

[4] Wolfgang Menz and Peter Bley; Mikrosystemtechnik für Ingenieure; (VCH; 1993)

[5] Volker Saile and Ulrike Wallrabe and Osamu Tabata and Jan G. Korvink; LIGA and its Applications; (Wiley-VCH; 2009)

[6] http://www.halbleiter.org/bilder/photolithography/methods/elektronenstrahllithografie.gif

[7] Rainer Brück and Nadeem Rizvi and Andreas Schmidt; Angewandte Mikrotechnik; (Carl Hanser Verlag; 2001)

[8] Anand Kumar Dokania; Laser Lithography

[9] http://www.halbleiter.org/bilder/photolithography/methods/projektionsbelichtung.gif

[10] E. Spiller and D.E. Eastman and R. Feder and W.D. Grobman and W. Gudat; Application of synchrotron radiation to x-ray lithography; Journal of Applied Physics **47** (1976) 5450–5459

[11] Charles Becnel and Yohannes Desta and Kevin Kelly; Ultra-deep x-ray lithography of densely packed SU-8 features: II. Process performance as a function of dose, feature

height and post exposure bake temperature; J. Micromech. Microeng **15** (2005) 1249–1259; http://dx.doi.org/10.1088/0960-1317/15/6/016

[12] http://www.mems-exchange.org/users/masks/fig2.png

[13] F. Asmussen and H. Sotobayashi and W. Schnabel; Entwicklung und Untersuchung empfindlicher und prozeßkompatibler Polymere für die Röntgenlithographie; (BMFT-FB-T 83-122; 1983)

[14] Sven Achenbach; Deep sub micron high aspect ratio polymer structures produced by hard x-ray lithography; Microsystem Technologies **10** (2004) 493–497; http://dx.doi.org/10.1007/s00542-004-0379-2

[15] Linke Jian and Yohannes M. Desta and Jost Goettert and Martin Bednarzik and Bernd Loechel and Yoonyoung Jin and Georg Aigeldinger and Varshni Singh and Gisela Ahrens and Gabi Gruetzner and Ralf Ruhmann and Reinhard Degen; SU-8 based deep x-ray lithography/LIGA; Micromachining and Microfabrication Process Technology VIII **4979** (2003) 394–401; http://dx.doi.org/10.1117/12.478246

[16] Olaf Mertsch; Nanoporöse und ultra-hydrophobe Strukturen im Negativresist SU8; Ph.D. thesis; Technische Universität Berlin; 2008

[17] http://en.wikipedia.org/wiki/SU-8_photoresist

[18] Pascal Meyer; e-mail correspondence

[19] F. Chollet; SU-8: Thick Photo-Resist for MEMS

[20] Timo Mappes and Sven Achenbach and Arndt Last and Jürgen Mohr and Roman Truckenmüller; Evaluation of optical qualities of a LIGA-Spectrometer in SU-8; Microsystem Technologies **10** (2004) 560–563; http://dx.doi.org/10.1007/s00542-004-0403-6

[21] E.W. Becker and W. Ehrfeld and D. Münchmeyer and H. Betz and A. Heuberger and S. Pongratz and W. Glashauser and H.J. Michel and R. v.Siemens; Production of Separation-Nozzle Systems for Uranium Enrichment by a Combination of X-Ray Lithography and Galvanoplastics; Naturwissenschaften **69** (1982) 520–523

[22] L. Hahn and P. Meyer and K. Bade and H. Hein and J. Schulz and B. Löchel and H.U. Scheunemann and D. Schondelmaier and L. Singleton; MODULIGA: The LIGA

process as a modular production method - current standardization status in Germany; Microsystem Technologies **11** (2005) 240–245; http://dx.doi.org/10.1007/s00542-004-0368-5

[23] B. Loechel and J. Goettert and Y.M. Desta; Direct LIGA service for prototyping: status report; Microsyst Technol **13** (2007) 327–334; http://dx.doi.org/10.1007/s00542-006-0241-9

[24] S. Achenbach and F.J. Pantenburg and J. Mohr; Optimierung der Prozeßbedingungen zur Herstellung von Mikrostrukturen durch ultratiefe Röntgenlithographie (UDXRL); (Wissenschaftliche Berichte FZKA 6576; 2000)

[25] Hansgeorg Hofmann and Jürgen Spindler; Verfahren der Oberflächentechnik; (Carl Hanser Verlag; 2004)

[26] A.L. Bogdanov and S.S. Peredkov; Use of SU-8 photoresist for very high aspect ratio x-ray lithography; Microelectron. Eng. **53** (2000) 493–496; http://dx.doi.org/http://dx.doi.org/10.1016/S0167-9317(00)00363-4

[27] G. Aigeldinger and C.-Y.P. Yang and D.M. Skala and D.H. Morse and A.A. Talin and S.K. Griffiths and J.T. Hachman and J.T. Ceremuga; Influence of mask substrate materials on resist sidewall roughness in deep X-ray lithography; Microsyst Technol **14** (2008) 277–286; http://dx.doi.org/10.1007/s00542-007-0419-9

[28] Klaus Wille; Physik der Teilchenbeschleuniger und Synchrotronstrahlungsquellen; (B.G.Teubner; 1992)

[29] Ulf Berges; Hochauflösende optische Strahldiagnose mittels Synchrotronstrahlung am Beispiel der Synchrotronstrahlungsquelle DELTA; Ph.D. thesis; Universität Dortmund; 2000

[30] http://www.synchrotron-soleil.fr/images/Image/IndustrieValorisation/EquipementIndustrie/image002.jpg

[31] J. Als-Nielsen and D. McMorrow; Elements of Modern X-Ray Physics; (Wiley; 2001)

[32] Metin Tolan; X-ray scattering from soft matter thin films; (Springer; 1999)

[33] Simone Streit; Surface structure and dynamics of supercooled polymer melts and metal-polymer nanocomposites; Ph.D. thesis; Universität Dortmund; 2007

[34] Michael Paulus; Röntgenstreuung an Flüssigkeits-Gas Grenzflächen; Ph.D. thesis; Universität Dortmund; 2006

[35] Daniela Lietz; Hochenergiereflektometrie an Festkörper-Gas und Festkörper-Flüssigkeits-Grenzflächen; Master's thesis; Universität Dortmund; 2007

[36] O. H. Seeck; LSFIT; 1999; Software for analysis of x-ray and neutron reflectivities

[37] Richard Eckert; Sehen heißt wissen - Das Rasterelektronenmikroskop im Fehleranalyselabor; (Druckerei E. Kurz & Co.; first edition; 1998)

[38] Ludwig Reimer; Scanning Electron Microscopy - Physics of Image Formation and Microanalysis; (Springer Verlag; 1985)

[39] Klaus Wetzig and Dietrich Schulze; In situ Scanning Electron Microscopy in Materials Research; (Akademie Verlag; 1995)

[40] http://www.purdue.edu/rem/rs/sem.htm

[41] J. Valentin and M.A. Weber and R. Brodmann and A. Sharp; 3D-Characterisation of Sheet Metal and Roller Surfaces by Means of Confocal Microscopy; Advanced Materials Research **6-8** (2005) 543–550; http://dx.doi.org/10.4028/www.scientific.net/AMR.6-8.543

[42] Michael Wegner; Konfokale Mikroskopie zur Topografiebestimmung technischer Oberflächen; Ph.D. thesis; Universität Stuttgart; 2002

[43] FRT GmbH; Oberflächen zerstörungsfrei und hochauflösend messen

[44] Marvin Minsky; Memoir on Inventing the Confocal Scanning Microscope; Scanning **10** (1988) 128–138

[45] M.David Egger and Mojmir Petran; New reflected-Light Microscope for Viewing Unstained Brain and Ganglion Cells; Science **157** (21) 305–307; http://dx.doi.org/10.1126/science.157.3786.305

[46] Mahr GmbH; MarSurf. Oberflächen-Kenngrößen

[47] Michael Nimz; Methoden zur quantitativen Erfassung der lokalen Verformung und schädigung bei der Blechumformung; Ph.D. thesis; TU Darmstadt; 2002

[48] G. Schmidt and U. Berges and K. Dunkel and J. Friedl and A. Gasper and M. Grewe and P. Hartmann and R. Heine and E. Kasel and B. Keil and D. Schirmer and T. Weis and K. Wille and D. Zimoch; Status of the synchrotron light source DELTA; Proceedings of EPAC 2002 (2002)

[49] VAT; Vakuumventile 2009

[50] Metin Tolan; personel communication

[51] Pfeiffer Vacuum Technology; Vacuum Technology Know How - Pfeiffer Vacuum 2009

[52] Varian; Product Catalog 2006

[53] Thorsten Rüspeler; e-mail correspondence

[54] Robin L. Owen and James M. Holton and Clemens Schulze-Briese and Elspeth F. Garman; Determination of X-ray flux using silicon pin diodes; Journal of Synchrotron Radiation **16** (2009) 143–151; `http://dx.doi.org/10.1107/S0909049508040429`

[55] MicroChemicals; Nano SU-8

[56] MicroChemicals; Substratreinigung und Haftvermittlung

[57] Gisela Pike; e-mail correspondence

[58] Mark Bachmann; RCA-1 silicon Wafer Cleaning; 1999; Integrated Nanosystems Reasearch Facility application note

[59] Gisela Ahrens; personel communication

[60] micromotion®; micromotion products

[61] Johannes Kenntner; e-mail correspondence

[62] Manfred Strohrmann; Intelligentes Mikrosystem zur Messung von Beschleunigungen basierend auf LIGA-Mikromechanik; Ph.D. thesis; Forschungszentrum Karlsruhe; 1995

[63] A. Both and W. Bacher and M. Heckele and K.-D. Müller and R. Ruprecht and M. Strohrmann; Fabrication of LIGA-acceleration sensors by aligned molding; Microsystem Technologies **2** (1996) 104–108

[64] P. Meyer and J. Schulz and L. Hahn; DoseSim:Microsoft-Windows graphical user interface for using synchrotron x-ray exposure and subsequent development in the LIGA process; Review of Scientific Instruments **74** (2003) 1113–119; `http://dx.doi.org/10.1063/1.1532542`

[65] D. Lietz and M. Paulus and C. Sternemann and U. Berges and B. Hippert and M. Tolan; The New X-Ray Lithography Beamline BL1 At DELTA; AIP Conference Proceedings **1234** (2010) 363–366; `http://dx.doi.org/10.1063/1.3463213`

[66] Gisela Ahrens; quality protocol; 26. July 2010

[67] P. Coane and R. Giasolli and S. Ledger and K. Lian and Z. Ling and J. Göttert; Fabrication of HARM structures by deep-X-ray lithography using graphite mask technology; Microsystem Technologies **6** (2000) 94–98

[68] Robert Fendt; Strukturuntersuchungen an dünnen Flüssigkeitsfilmen; Master's thesis; Universität Dortmund; 2003

[69] Felix Lehmkühler and Michael Paulus and Simone Streit-Nierobisch and Metin Tolan; Determination of microscopic interaction constants by X-ray reflectivity measurements; Fluid Phase Equilibria **268** (2008) 95 – 99; `http://dx.doi.org/DOI:10.1016/j.fluid.2008.04.007`

[70] Streit-Nierobisch, S. and Gutt, C. and Paulus, M. and Tolan, M.; Cooling rate dependence of the glass transition at free surfaces; Phys. Rev. B **77** (2008) 041410; `http://dx.doi.org/10.1103/PhysRevB.77.041410`

[71] Sauer, Bryan B. and Dee, Gregory T.; Molecular weight and temperature dependence of polymer surface tension: comparison of experiment with theory; Macromolecules **24** (1991) 2124–2126; `http://dx.doi.org/10.1021/ma00008a070`

[72] Sprung, M. and Seydel, T. and Gutt, C. and Weber, R. and DiMasi, E. and Madsen, A. and Tolan, M.; Surface roughness of supercooled polymer melts; Phys. Rev. E **70** (2004) 051809; `http://dx.doi.org/10.1103/PhysRevE.70.051809`

[73] J.D. Jackson; Klassische Elektrodynamik; (de Gruyter; second edition; 1985)

[74] L.G. Parratt; Surface Studies of Solids by Total Reflection of X-Rays; Phys. Rev.95 **2** (1954) 359.

Danksagung

Zum Gelingen dieser Arbeit haben viele Leute beigetragen. Bei ihnen allen möchte ich mich ganz herzlich für ihre Hilfe und Unterstützung bedanken.

Zu Beginn danke ich meinem Doktorvater Herrn Prof. Dr. Metin Tolan, der mir durch das Lithographie-Projekt die von mir gewünschte anwendungsbezogene Dissertation ermöglicht hat. Danke für Ihr Vertrauen in meine Arbeit und die freie Hand, die Sie mir während des Projekts gewährt haben. Die Zeit, die ich an Ihrem Lehrstuhl verbringen durfte, hat mir sehr viel Spaß gemacht.

Ich bedanke mich bei der Firma Micromotion GmbH und insbesondere bei ihrem Mitarbeiter Herrn Dr. Kirsch. Dank der zur Verfügung gestellten Maske war es möglich, Testbelichtungen bei DELTA durchzuführen und die Möglichkeiten von DELTA für DXRL zu bestimmen.

Ein herzliches Danke schön geht an die Mitarbeiter der AG von Herrn Dr. Mohr am KIT in Karlsruhe. Insbesondere möchte ich an dieser Stelle Johannes Kenntner, Dr. Pascal Meyer und Dr. Martin Börner nennen. Vielen Dank, dass ich euch besuchen durfte und ihr mir einen Einblick in eure Arbeit ermöglicht habe, sowie für die Röntgenmasken, die ihr mir zur Verfügung gestellt habt. Vielen Dank darüberhinaus für die Infos zu eurer Wafer-Masken-Halterung, auf deren Basis ich eine Halterung für BL 1 bauen konnte und für das Programm DoseSim.

Ich möchte mich bei Frau Ahrens von der Firma micro resist technology GmbH für die Diskussionen über die Belichtungsergebnisse bedanken.

Ich danke Herrn Prof. Dr. Weis, dass er die Aufgabe des Zweitgutachters übernommen hat.

Ganz herzlich bedanken möchte ich mich bei meinen Kollegen Dr. Ulf Berges, Dr. Christian Sternemann, Dr. Michael Paulus sowie Thorsten Brenner für ihre Hilfe und Unterstützung beim Bau der Strahllinie, für das Korrekturlesen meiner Arbeit und dafür, dass sie für viel Freude bei der Arbeit an BL 1 gesorgt haben.

Zum Aufbau der Strallinie beigetragen haben ebenfalls Thorsten Witt, Georg Jülicher, die mechanische Werkstatt unter Leitung von Susanne Kralemann, die Elektro-Werkstatt sowie das Konstruktionsbüro von Herrn Rudloff. Ein großes Dankeschön daher an euch alle.

Den Mitarbeitern von DELTA danke ich für Ihre Hilfe und Ratschläge beim Beamline Aufbau und Jochem Friedl für seine Unterstützung in Sachen Strahlensicherheit an BL 1.

Meinem ehemaligen Kollegen Heiko Conrad möchte ich meinen Dank für seine Unterstützung bei der Erstellung der Konstruktionszeichnungen der BL 1 Komponenten aussprechen.

Danken möchte ich auch Frau Pike und Herrn Schemionek aus dem Präparationslabor, die mir bei der Herstellung der Waferproben geholfen haben.

Ein herzliches Dankeschön geht an Dr. Alex von Bohlen für seine Hilfe während der ersten Testmessungen an der ISASLine BL 2 bei DELTA und für seine Unterstützung bei der Untersuchung meiner Proben mit dem Rasterelektronenmikroskop.

Vielen Dank an Benedikt Sieben und Thorsten Upmeier vom ISF für ihre Hilfe bei der Rauheitsbestimmung meiner strukturierten Proben.

Uli Marggraf danke ich für seine Hilfe bei der Waferbelackung und die Möglichkeit den Gelbraum der AG MST der Fakultät ET&IT zu nutzen.

Dr. Julia Nase und Dr. Bridget Murphy danke ich für ihre Bereitschaft meine Arbeit Korrektur zu lesen.

Ganz herzlich danken möchte ich dem Lehrstuhl E1a. Die Arbeit mit euch in den letzten Jahren hat mir sehr viel Spaß gemacht. Herzlichen Dank auch an Saskia Schmacke für viele Jahre Freundschaft und das gemeinsame Studium.

Danke schön an meine Familie, meinen Freundeskreis und meine "Wikinger" für gelungene Abwechslungen vom Arbeitsalltag.

Meinem Freund Jörg Walbersloh danke ich ganz herzlich für seine Unterstützung und Hilfe während meiner Promotion. Danke, dass du immer für mich da bist.

Ganz herzlich danken möchte ich meinen Eltern Heike und Ulrich Lietz. Ihr habt mich mein Leben lang unterstützt und mir stets den Rücken gestärkt. Vielen Dank, dass ihr stets zu mir steht!